EVALUATION OF PROCESS-STRUCTURE-PROPERTY RELATIONSHIPS OF CARBON NANOTUBE FORESTS USING SIMULATION AND DEEP LEARNING

A Dissertation presented to

the Faculty of the Graduate School

at the University of Missouri

In Partial Fulfillment

of the Requirements for the Degree

Doctor of Philosophy

---

by

TAHER HAJILOUNEZHAD

Prof. Matthew R. Maschmann, Dissertation Supervisor

MAY 2020

The undersigned, appointed by the Dean of the Graduate School, have examined the dissertation entitled:

EVALUATION OF PROCESS-STRUCTURE-PROPERTY RELATIONSHIPS OF CARBON NANOTUBE FORESTS USING SIMULATION AND DEEP LEARNING

presented by Taher Hajilounezhad,

a candidate for the degree of Doctor of Philosophy and hereby certify that, in their opinion, it is worthy of acceptance.

Professor Matthew R. Maschmann

Professor Yangchuan Xing

Professor Robert A. Winholtz

Professor Jian Lin

Professor Zheng Yan

DEDICATION

To my wife, sons, and parents; you've given me pure love, encouragement, hope, and motivation. I would not be able to complete my PhD adventure without you. Specially, I always feel my father's inspiration to complete this journey.

ACKNOWLEDGMENTS

I express my genuine gratitude to my advisor, Prof. Matthew Maschmann, for his endless encouragement and support during my academic career. His guidance, positive attitude, encouragement, and confidence in me has helped me accomplish my academic life goals. My graduate research career has been smooth-sailing and free of the hardships typically associated with advisor-student relationships. He always supported me when I lost hope and steered me through this research and all aspects of graduate school. He is not only my adviser but also a great mentor and a marvelous person. I will never forget your smiles and "what do you think" statements. I am forever indebted. I also thank my thesis committee members, Professor Yangchuan Xing, Professor Robert A. Winholtz, Professor Jian Lin, and Professor Zheng Yan, for their provision and accommodation during the writing and editing process. You have shared many valuable insights during this time.

I thank my collaborators from MU Electrical Engineering and Computer Science (EECS) Department, Professor Palaniappan, Professor Calyam, Dr. Bunyak, Rina Bao and Zakariya Oraibi, MU Electron Microscopy Core Facility (specially David Stalla), and MIT Mechanosynthesis Group (Professor Hart), for productive collaboration and direction. My colleagues here at Mizzou have also been a guiding light for my research, career, and perspective; thank you Ryan Hines, Benjamin Davis, Josef Brown, Matthew Riehn, Andrew Countryman, Gordon Koerner, Ramakrishna Surya and Damola Ajiboye. I've learned much about science and the world from you. Moreover, I am extending my gratitude to Pourang Shamsi, whose positive attitude and sincere support always drove me through all this journey. Also, I would like to express my gratitude to Professor Calyam

for his friendly support, professional collaboration and providing me with a nice office to write my dissertation. Finally, I'd like to acknowledge and thank the National Science Foundation (NSF) for funding my projects under award CMMI 1651538 and MU EMC for funding my in-situ electron microscopy experimentation under EMC Excellence Award 2019. The computation for this work was performed on the high-performance computing infrastructure provided by Research Computing Support Services and in part by the National Science Foundation under grant number CNS-1429294 at the University of Missouri, Columbia MO.

TABLE OF CONTENTS

LIST OF FIGURES

Figure **Page**

LIST OF TABLES

ABSTRACT

This work is aimed to explore process-structure-property relationships of carbon nanotube (CNT) forests. CNTs have superior mechanical, electrical and thermal properties that make them suitable for many applications. Yet, due to lack of manufacturing control, there is a huge performance gap between promising properties of individual CNTs and CNT forest properties that hinders their adoption into potential industrial applications. In this research, computational modelling, in-situ electron microscopy for CNT synthesis, and data-driven and high-throughput deep convolutional neural networks are employed to not only accelerate implementing CNTs in various applications but also to establish a framework to make validated predictive models that can be easily extended to achieve application-tailored synthesis of any materials.

A time-resolved and physics-based finite-element simulation tool is modelled in MATLAB to investigate synthesis of CNT forests, specially to study the CNT-CNT interactions and generated mechanical forces and their role in ensemble structure and properties. A companion numerical model with similar construct is then employed to examine forest mechanical properties in compression. In addition, in-situ experiments are carried out inside Environmental Scanning Electron Microscope (ESEM) to nucleate and synthesize CNTs. Findings may primarily be used to expand the forest growth and self-assembly knowledge and to validate the assumptions of simulation package. Also, SEM images can be used as feed database to construct a deep learning model to grow CNTs by design.

The chemical vapor deposition parameter space of CNT synthesis is so vast that it is not possible to investigate all conceivable combinations in terms of time and costs. Hence, simulated CNT forest morphology images are used to train machine learning and learning algorithms that are able to predict CNT synthesis conditions based on desired properties. Exceptionally high prediction accuracies of $R^2 > 0.94$ is achieved for buckling load and stiffness, as well as accuracies of > 0.91 for the classification task. This high classification accuracy promotes discovering the CNT forest synthesis-structure relationships so that their promising performance can be adopted in real world applications. We foresee this work as a meaningful step towards creating an unsupervised simulation using machine learning techniques that can seek out the desired CNT forest synthesis parameters to achieve desired property sets for diverse applications.

CHAPTER 1

CARBON NANOTUBES, SYNTHESIS, PROPERTIES AND APPLICATIONS

1.1 Introduction

Carbon nanotubes (CNTs), seamless cylinders of graphene, have been widely studied since their discovery in 1991 by Iijima [1]. CNTs have superior mechanical, thermal, electrical and optical properties [2] that make them a great candidate for many applications. They are self-assembled hollow tubes featuring a nanometer scale diameter and lengths that vary from micrometers to millimeters, offering a high aspect ratio. For example, their Young's Modulus is on the order of 1 TPa [3] while it is sufficiently flexible to be tied into a knot [4, 5]. Also, they have outstandingly higher thermal conductivity compared to other conventional conductive engineering materials like copper, i.e. 10,000 W/m-K [6] for CNT (compared to nearly 400 W/m-K for copper). CNTs have comparable electrical conductivity to metals [7], while offering resistance to electromigration at high current [8].

Populations of CNTs that self-assemble into vertically oriented films during their synthesis, usually normal to the surface of a substrate, are called carbon nanotube (CNT) forests, CNT arrays or CNT turfs. However, the engineering properties of CNT forests are often significantly diminished relative to properties of isolated CNTs. An SEM image of internal morphology of CNT forests is shown in **Figure 1**. Although there is no comprehensive understanding governing the kinetics of growing and interacting CNTs, there are numerous studies and approaches that are conducted to achieve a manufacturing-level control over the synthesis, integration and assembly of CNT forests (discussed in more details in the proceeding chapters). Nevertheless, scientists believe that the major possible reason for property degradation of CNT forests is the structural disorder (as shown in **Figure 1a-b**) resulting from poor processing control which also leads to highly variable properties. **Figure 2** represents a typical comparison of individual CNT and CNT forest

modulus, stiffness and thermal conductivity with conventional engineering materials. Some orders of magnitude of property degradation is obvious by comparing for instance modulus of isolated CNTs with diamond, gold and rubber. It is shown that individual CNTs are approximately as stiff as diamond while CNT forests are as soft as rubber, a 4-5 orders of magnitude degradation.

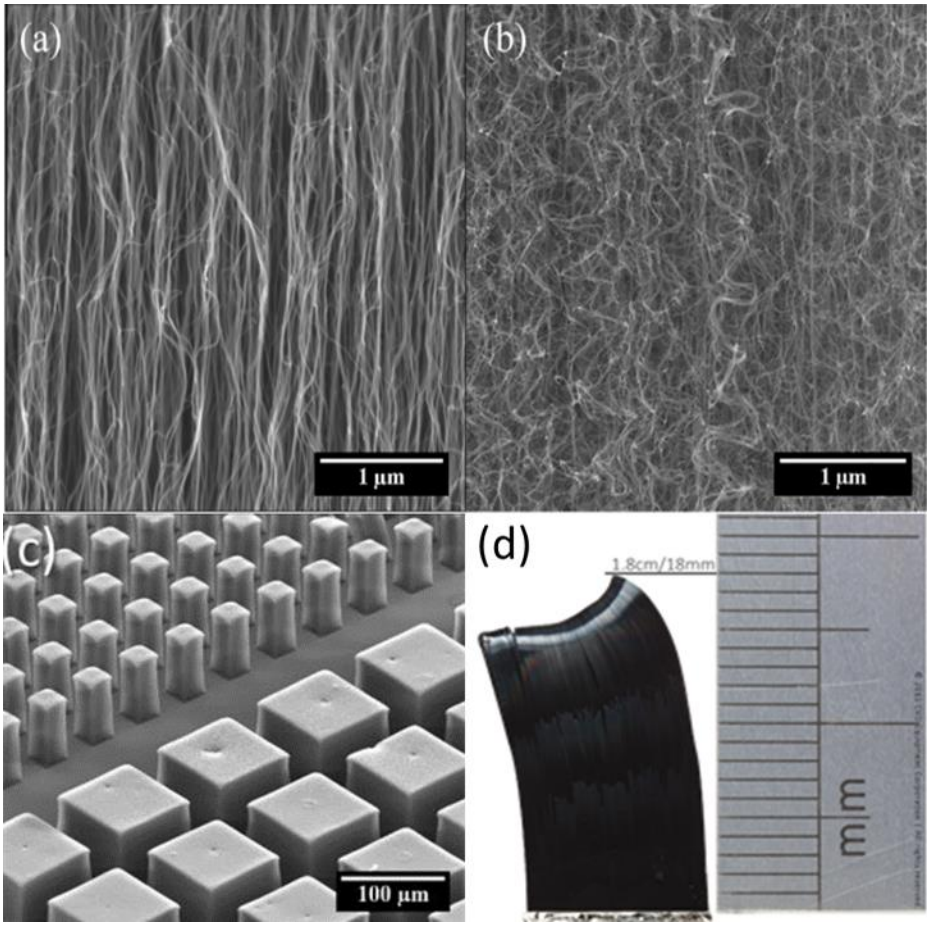

Figure 1. SEM image of internal morphology of (a) a relatively straight CNT forest (b) a tortuous and wavy CNT forest (c) microscale MEMS architectures consisting of patterned CNT forests [9] (d) a centimeter-scale super tall CNT forest [10].

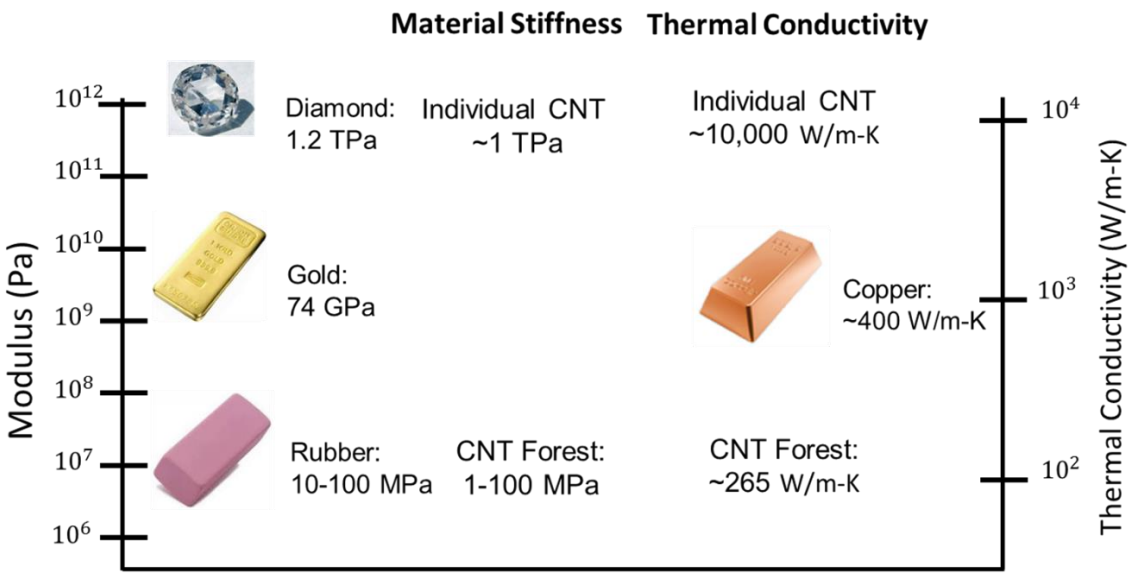

Figure 2. A comparison of individual CNT and CNT forest modulus, stiffness and thermal conductivity with conventional engineering materials.

1.2 Properties of Carbon Nanotubes

1.2.1 Mechanical Properties

In general, CNTs can sustain large elastic strain [11], high fracture strength [12], and high elastic modulus [13], high bending stiffness [14], among others. Iijima et al. [15] showed the excellent flexible properties of carbon nanotubes and remarkable resistance to large strains. Chirality (crystal structure) has little influence on tensile modulus of SWNT's [16]. The axis of the nanotube can form along many different directions [i.e., chiral vectors (n, m)] in the carbon layer, yielding CNTs with different chirality and diameters. Under large deformation CNTs change to different morphological patterns where each shape signifies an instantaneous release of energy in the stress/strain curve. The maximum moment that the tube can withhold, or the critical kinking moment is calculated by [17, 18]:

$$M_{kink} = 0.4683 \frac{EDt^2}{\sqrt{1-\nu^2}} \tag{1}$$

where t is the thickness of the tube and ν is the Poisson ratio of the tubes's material ($\nu = 0.17$ for graphite [19]). Further, the yield strength of carbon nanotubes depends on its symmetry [20].

CNTs are among the strongest and stiffest materials yet discovered. Their tensile strength is up to 100 GPa and elastic modulus is over 1 TPa, for ideal defect-free SWCNTs. Although their radial elasticity is relatively low, they are extremely flexible because of their ability to flatten and form a non-circular cross-sectional shape. Under some conditions (see Eq. (1)), CNTs will spontaneously collapse to a flattened structure, for energy minimization, a balance between attractive van der Waals potential and high-curvature strain energy. They tend to buckle when placed under compressive, torsional, or bending stress, because of their hollow structure and high aspect ratio [21].

1.2.2 Electrical, Thermal and Optical Properties

CNTs offer outstanding electrical conductivity which depends on how the hexagons are oriented along the axis of the tube (chirality). For instance, adding only a little amount of CNTs (~2 wt%) into polymers, turn them into conductive composites [22]. Depending on their chirality (see **Figure 3**), CNTs can be either metallic or semiconducting along the axis; armchair (n,n) nanotubes are always metallic, while zigzag (n,0) and other (n,m) chiralities are semiconducting [23]. In theory, metallic nanotubes can carry an electric current density of 4×10^9 A/cm^2 (3 orders of magnitude more than copper) [24]. Electrons propagate only along the CNT axis, so they are commonly called one-dimensional conductors.

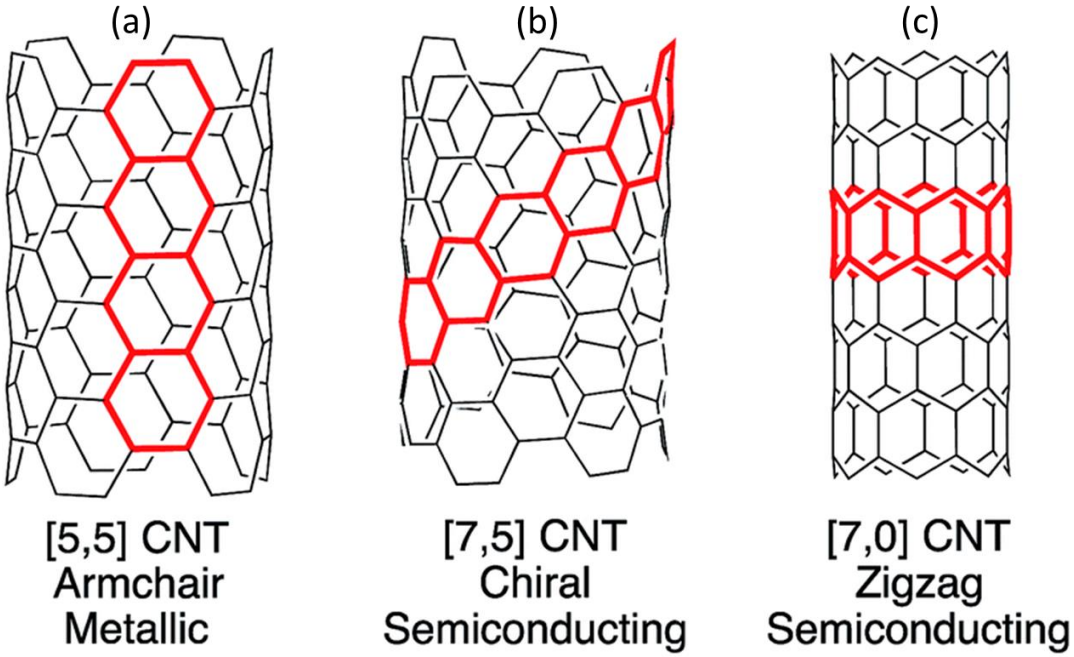

Figure 3. Representation of CNT chirality and of carbon nanotubes (a) arm-chair (b) chiral (c) zig-zag [25].

Furthermore, carbon nanotubes offer interesting optical properties like absorption, photoluminescence. Spectroscopic methods offer quick and non-destructive characterization; a quantifiable way of assessing CNT quality, assigning chirality and measuring defect density.

CNTs have excellent thermal transport properties that arises from strong carbon-carbon chemical bonding [26]. Transport of thermal energy through a CNT is dominated by the phonon conduction mechanism (principally based on collective vibration of carbon atoms) [6]. High expectations for the thermal conductivity of CNTs were originally based on the high in-plane thermal conductivity of graphite and the high thermal conductivity of bulk and thin film diamond [27]. The long range crystallinity, long phonon mean free path and larger speed of sound of the CNTs lead to the large thermal conductivity [23]. In principle, with temperatures increasing from relatively low to around room temperature, phonon conduction varies correspondingly from ballistic/ quasiballistic to diffusive behavior.

1.3 CNT Forest Applications

As discussed earlier in the previous section, CNTs have numerous beneficial mechanical, thermal and electronic properties that make them desirable robust physical sensors [28-32], thermal interfaces [33-35], lithium ion batteries [36-39], electrochemical energy storage [40], space composite structures [41-44], high performance composites [45-49], and electrical interfaces and Vertical Interconnect Access (VIAS) [50-52]. In addition, CNTs are widely employed in novel applications such as advanced sensors for defect monitoring in fiber-reinforced polymer composites [53-56], electrochemical capacitors [57, 58], photodetectors [59], thin-film flexible electronics [60-62], transparent conductive membranes [63], bioelectronics [64] and dry adhesives [65-68]. In addition, CNTs are employed to reinforce composites [69-73]

Rao et. al. [74] presented the recent advances in CNT application as shown in **Figure 4a** with a focus on single-walled CNTs integrated in fibers, membranes, electronics, thermal interfaces and energy storage applications. In **Figure 4b**, the horizontal axis shows the organization of the SWCNTs from a random network to highly aligned architectures (vertically aligned, fibers, etc.), while the vertical axis shows the degree of diameter/helicity control from mixed to single helicity. Existing and emerging SWCNT applications are shown in the square and oval boxes, respectively.

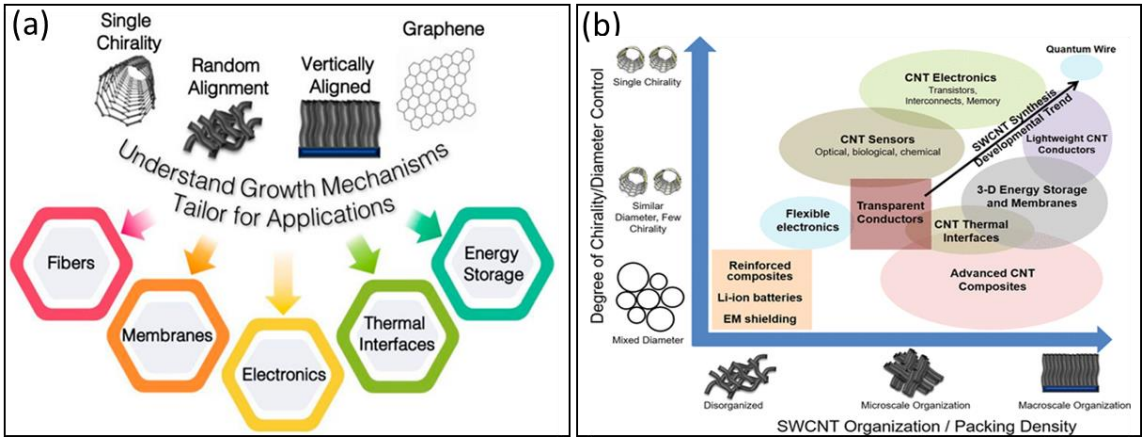

Figure 4. (a) Different application of CNTs (b) Structure–property relationship diagram showing the application space of SWCNTs with respect to tube diameter/helicity and architecture [74].

1.4 CNT Forest Synthesis

In order to achieve high-performance and application-specific CNT materials, various synthesis techniques should be applied to control geometrical structure, chirality, orientation, alignment, density, and morphology of CNTs. However, there are three common CNT growth methods including arc-discharge, laser ablation, and thermal chemical vapor deposition (CVD).

1.4.1 Arc-discharge

Arc-discharge consists of an apparatus with two graphitic rods under vacuum. First, an ambient gas (usually methane that is more effective than inert gases like helium and argon) is introduced to the system followed by applying an arc voltage between each graphite rod [75]. When the evaporated anode is absorbed onto the cathode, high quality multi-walled CNT (MWCNT) are generated. In order to synthesize single-walled CNT (SWCNT), graphitic rods that contain metal catalysts such as iron and cobalt can be employed as the anode with a graphite cathode. A schematic of arc-discharge method for CNT growth is shown in **Figure 5a.**

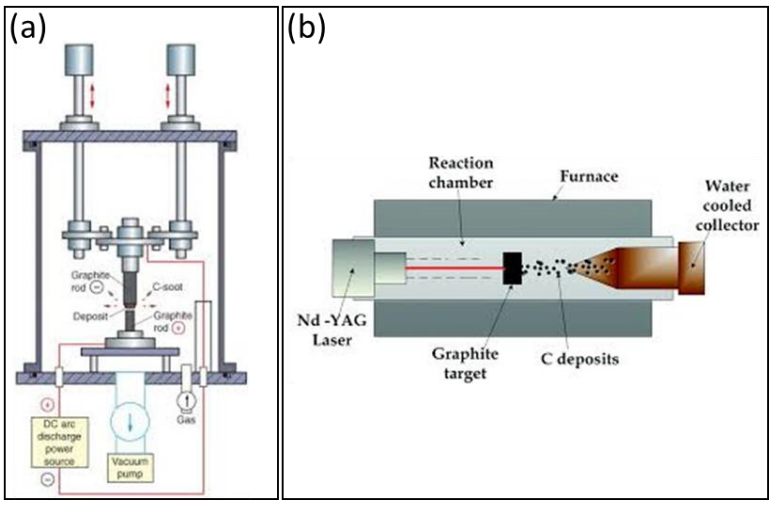

Figure 5. Schematic of (a) arc-discharge [75] (b) laser-furnace apparatus for CNT growth [76].

1.4.2 Laser Ablation

Laser-furnace vaporization provides a suitable method for CNT synthesis and other fullerenes where a laser outside of the furnace, typically introduced from a yttrium aluminum garnet (YAG) crystal, focuses onto a target through a window into a quartz tube and onto a target in the center of the furnace. The target consisting of a carbon composite doped with catalyst metals is vaporized under argon gas flow forming SWCNT [75]. There are numerous advantages of this method like the production of high quality SWCNT and CNT diameter control through tuning the catalyst materials, flow rate, and furnace temperature. The laser-furnace method is not only important for CNT production but the advancement for other nanomaterials. A schematic of laser-furnace apparatus for CNT growth is shown in **Figure 5b.**

1.4.3 Chemical Vapor Deposition (CVD)

CNT forests are typically synthesized using chemical vapor deposition (CVD) in which transition metal catalyst nanoparticles (mainly Fe or Ni) facilitate the catalytic conversion of gas-phase hydrocarbon species (such as acetylene or ethylene) into solid CNTs on a metal catalyst that is either already fixed on a substrate or simultaneously flowing into the system with the carbon feedstock. The catalyst particle may reside on the growth substrate during CNT growth (base growth) [77], or it may reside at the tip of a growing CNT (tip growth) [78]. Using conventional CVD processes, CNT forest synthesis is generally observed to follow a base-growth mechanism, placing significance on catalyst-substrate interactions throughout the duration of

CNT synthesis. Catalyst is usually deposited as a thin film that is later transformed to catalyst nanoparticles by an annealing step at high temperatures (600 °C- 950 °C) [79, 80].

CVD provides a better control over various synthesis parameters including hydrocarbon precursor type and flow rates, catalyst type and required thicknesses, substrate type, temperature, and pressure. In addition, there is a good flexibility choosing the carbon precursor and the catalyst source which can be either solid, liquid, or gas, providing versatility in the CNT synthesis. Other underlayers such as alumina or other oxide layers are used for thermal CVD to make use of their strong metal-support interaction that allows a high density of active catalyst sites and discourages sub-surface catalyst diffusion [81]. Larger clusters of catalyst would result in an undesirable graphitic carbon. A schematic of catalyst thin film layer conversion to nanoparticles by an annealing step followed by CNT nucleation is shown in **Figure 6a.** Catalyst thin film deposition is performed by various methods but an Ion Beam Sputtering (IBS) method with a South Bay Technology, Inc. system is used in our experimental works as shown in **Figure 6b.** Also, a CVD furnace facilitating fixed- and floating-catalyst CVD growth is displayed in **Figure 6c.**

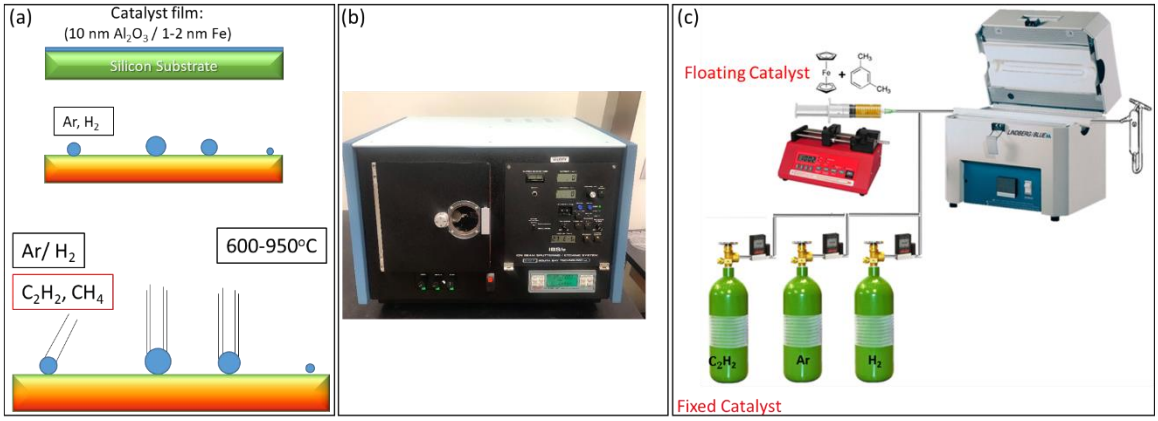

Figure 6. Chemical Vapor Deposition (CVD) method to grow CNTs (a) how a thin film of catalyst converted to nanoparticles by an annealing step followed by CNT nucleation (b) Ion Beam Sputtering (IBS) performed with a South Bay Technology, Inc. (b) a CVD furnace facilitating fixed- and floating-catalyst CVD growth.

1.5 CNT Forest Mechanics

The most common CNT synthesis method is chemical vapor deposition (CVD) where a thin film of catalyst (for the film-catalyst growth) is converted to nanoparticles through an annealing step. Then, the catalyst nanoparticles enable CNTs precipitation from the gas phase precursors. CVD method is already discussed in

the previous section. CNT populations grow concurrently from these catalyst nanoparticles at different rates angles of orientations and growth rates. Their interaction caused by van der Waals forces drives the vertical growth and self-assembly. The inhomogeneous and anisotropic structural morphology of CNT forests is shown in **Figure 1b**. Although several studies investigated the mechanics of CNT synthesis and self-assembly along with examining the resulting properties, the origin of the structural disorder is not fully discovered [82, 83]. However, most researchers rely on post-synthesis characterization or focused on growth rate measurements. So, it is essential to conduct emerging and advanced experiments to observe CNT-CNT interactions to observe structural morphology evolution in real time and high resolution. Understanding CNT forest collective growth mechanism enables adoption of CNTs into their various real-life applications.

Accordingly, some researchers carried out in-situ experiments to explore actively growing CNTs and forests using different approaches. Bedewy and Hart performed in-situ small angle x-ray scattering (SAXS) [83, 84] characterization of the spatially and temporally-varying internal morphology of CNT forests to explain the evolution and termination of CNT forests by a collective mechanism. They concluded that forest growth consists of four stages: (I) self-organization; (II) steady growth with a constant CNT number density; (III) decay with a decreasing number density; and (IV) abrupt self-termination, which is coincident with a loss of alignment at the base of the forest. This means that the forest density and growth rates are time-dependent and changing during the course of growth. They found out that the abrupt termination happens due to the loss of self-supporting structure (individual CNTs stop growing due to catalyst deactivation). In-situ SAXS measurements provided real-time height kinetics, alignment, diameter and density of CNT population as a function of time. The mass-based kinetics of a CNT population suggests that growth can be defined by the S-shaped Gompertz model, while the forest height and CNT length kinetics are essentially linear. Most importantly [82], they point out that the density and alignment of self-organized CNT growth is limited by mechanical coupling among CNTs in contact, in combination with their diameter-dependent growth rates. This reveals that the mismatch between concurrently growing CNTs,proportional to the diameter of individual CNTs (a quadratic function of CNT outer diameter), is the main reason behind generated mechanical forces that are exerted on the catalyst nanoparticles. These forces are also time-dependent (proportional to growth rate mismatch) and not also contribute to self-organization of CNT forests but also cause the tortuous and entangled forest morphology. It is proposed that these forces are also diameter

dependent. Furthermore, [85, 86] found that structural disorder is a distinct chemical and/or mechanical signature of self-terminated CNT forest growth.

Findings from discussed studies motivate the attempts to model CNT forest growth based on finite-element analysis. The experimental observations of CNT forest mechanics during synthesis are implemented into a time-resolved and physics-based simulation tool (discussed thoroughly in the proceeding chapter) that represents behavior of any individual CNT and resulting CNT-CNT interactions. The main outputs of the simulation are the structural morphology image (can be stored at all steps of growth from nucleation to termination) and diameter-dependent mechanical forces generated by the interaction of concurrently growing CNTs that are imparted to the substrate base. The computational model takes advantage of experimental discoveries and is also validated by a commercial finite-element analysis software (COMSOL). The same concepts are used to model CNT forest post-synthesis experiments like nanoindentation to obtain ensemble properties.

Other advanced experimental tools are applied to examine forest kinetics during growth like in-situ optical reflectance [86-89] and absorption [90] experiments. However, such experiments can only measure the ensemble CNT forest growth rate, while fail to investigate CNT-CNT interactions within growing forests due to insufficient resolution. In addition, since CNT measurements are performed by a 10 μm diameter x-ray beam for SAXS experiments, only collective average measurements (consisting of thousands of CNTs) are feasible. Also, it is unable to capture early stages of growth like nanoparticle formation, CNT nucleation and early CNT interactions. Moreover, in-situ Transmission Electron Microscopy (TEM) synthesis is conducted to provide real-time imagining of the nucleation and growth of individual CNTs [91-97]. Most recently, CNT populations are also observed at up to atomic-level resolution [98, 99]. They provide interesting results that determines limited CNT interactions (like 2 CNTs mechanical coupling) which is also used in our simulation package. While TEM is a powerful analytical and visual technique, previous in-situ TEM studies have emphasized CNT catalyst kinetics, with little or no emphasis on CNT interactions within a growing forest. So, cutting-edge in-situ SEM experiments are conducted to observe collective growth mechanics of concurrently growing CNTs to yield a broader understand of CNT-CNT interactions.

1.6 Data- & Artificial Intelligence-Driven Material Research

Advanced materials are essential to economic security and human well-being, with applications in many industries, yet it can take 20 or more years to move a material after initial discovery to the market. Accelerating the pace of discovery and deployment of advanced material systems will therefore be crucial to achieving global competitiveness in the 21st century. Rapid advances in computational modeling and data exchange and more advanced algorithms for modeling materials behavior facilitates combing innovative synthetic, experimental, and computational tools with digital data in an iterative fashion leading to validated predicative models that can reliably design next generation of new materials aimed to a wide market adoption and use. Data — whether derived from computation or experiment — are the basis of the information that drives the materials development continuum. Data inform and verify the computational models that will streamline the development process. machine learning is any approach that achieves artificial intelligence through systems that can learn from experience to find patterns in a set of data. In other words, ML involves the computer learning to recognize patterns (by supervised or unsupervised methods), rather than programming the computer with specific rules. In materials research, the goal is to have the computer help the researcher work usefully with data, and to do so either more quickly or more effectively, complementing more traditional approaches.

Machine learning methods, especially using deep learning architectures, require large amount of labeled training data. Unfortunately, the amount of available experimental data of emerging materials' growth is not sufficient to be used as labeled data for training the machine learning model due to the vast range of synthesis conditions, growth recipes and resultant morphologies reported in literature. Experimental results are usually noisy, expensive and time consuming, while the advanced material attributes are poorly characterized and time variant. Also, it is difficult and expensive to acquire enough data through the physical in-situ approaches. Therefore, the physics-based simulation of advanced materials (CNT forests in our research) may present a reliable and powerful tool for training ML models in the absence of suitable experimental data.

Hence in the current work, we propose using finite element simulation data for the initial boot strapping of the deep architecture weights along with generative adversarial networks. Traditional machine learning and advanced deep neural networks are employed to develop a model that contained physics-based

parameters, with which we are able to predict CNT forests mechanical, thermal and electrical properties with a remarkable precisions and accuracies. Predicting the combination of processing parameters required to grow application-tailored CNT forests would represent a significant advance that could enable new CNT forest-based applications that fully exploit the beneficial properties of individual CNTs.

This model is intended to become part of an active learning, closed-loop system that employs multiple sources of information including SEM CNT imagery, finite element simulation predictions, physical measurements and a knowledgebase of previous experimental results or mined from the literature. Such a system will broaden our theoretical understanding of CNT materials and provide a robust, deterministic methodology for discover materials with prescribed property sets for specific engineering applications. This work represents a substantial step towards fabricating materials by design.

CHAPTER 2

PHYSICS BASED AND TIME-RESOLVED SIMULATION OF CARBON NANOTUBE FORESTS: SYNTHESIS AND CHARACTERIZATION

2.1 Introduction

While the mechanical, thermal, and electrical properties of CNT forests may exceed traditional engineering materials, their properties are significantly degraded based on a volumetric scaling of individual CNT properties [9, 29, 33, 100-104]. The attributes of individual CNTs within a forest, such as diameter, growth rate, stiffness, and areal density, are distributed, and functional relationships between these attributes and CNT forest morphology are not fully understood. The distributed nature of these attributes creates strong heterogeneity within the forest, the physical effects of which remain poorly understood. Nevertheless, it is generally accepted that the wavy structural morphology of CNTs within forests formed during the self-assembly process [84] have deleterious effects on ensemble properties [82-86, 104], and efforts to understand and control forest morphology could lead to increased forest performance relative to mechanical, thermal, and electrical properties. The chemical vapor deposition (CVD) synthesis of CNT forests typically proceeds from the base-growth mechanism in which catalyst nanoparticles support CNT formation while residing on a rigid substrate throughout the duration of growth. As a result, the forces generated by CNT forest self-assembly are transmitted directly to the catalyst particles. The magnitude of these forces as a function of CNT population attributes and their impact to the self-assembly process has yet to be thoroughly examined.

Mechanical interactions between growing CNTs in contact lead to crowding and a general vertical orientation of CNTs, normal to the growth substrate. When in close proximity, neighboring CNTs are attracted to each other and are held in contact by short-range van der Waals forces. The contacts provide mechanical resistance to free motion of CNTs. Because CNTs in contact may be growing at drastically different rates and may provide different effective stiffness in response to deformation, force is generated

between contacting CNT pairs. The forces are transmitted through the CNT and are of sufficient magnitude to deform CNTs, leading to the typical tortuous CNT morphological appearance observed in experiments. The tortuous CNTs are intermixed with vertically oriented CNTs, suggesting mechanical competition during the growth process. Differences in interaction during growth can lead to drastically different CNT alignment and tortuosity, even within the height of a single CNT forest. An example of relatively straight CNT morphology is compared to a more tortuous morphology in **Figure 7**.

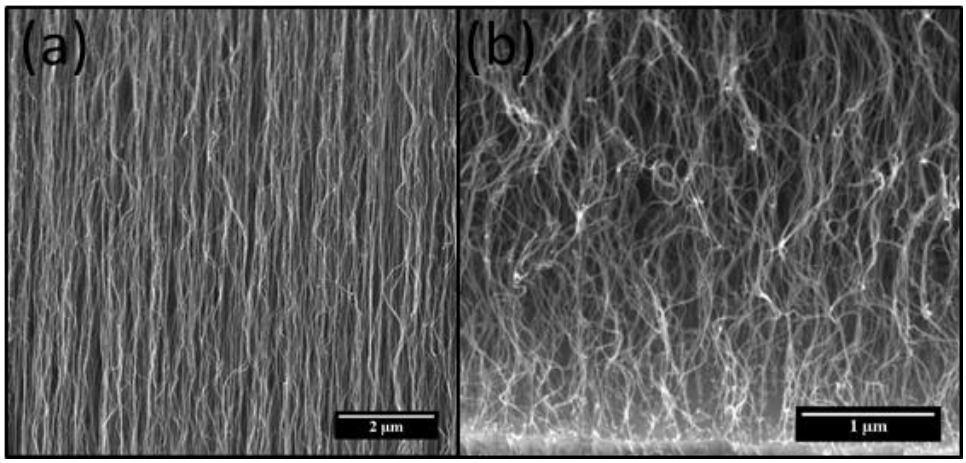

Figure 7. SEM micrographs of two different CNT forests that feature (a) a morphology that is well aligned and (b) a morphology that is highly tortuous and wavy in nature [105].

A lack of a detailed understanding governing the kinetics of growing and interacting CNTs hinders the ability of researchers to control the ensemble properties of CNT forests. The mechanical coupling among CNTs during forest growth undoubtedly plays an important role on CNT forest collective growth and self-assembly [82]. The complexity of the coupling is made more difficult by the distributed nature of CNT physical attributes. Fundamental kinetics studies using small angle x-ray scattering (SAXS) have revealed that the areal density, alignment, and diameter distribution of CNT forests evolve with time and that CNT forest growth termination is often abrupt [84-86, 106]. Recently, an external compressive force applied to the top surface of CNT forests was shown to decrease the ensemble forest growth rate, indicating that CNT growth kinetics are directly influenced by even relatively small external forces [107]. The forces generated by forest self-assembly and transmitted to CNT catalyst particles are expected to exceed those applied in the experiment while also manifesting as both tensile and compressive orientations. By extension, it may be assumed that the mechanical forces generated during self-assembly similarly modulate the growth rate of

individual CNTs during their growth and may contribute to the abrupt growth termination of CNT forests [82, 83, 85, 107]. Measuring the evolution of forces within a forest at the level of individual CNTs is currently inaccessible by experimental techniques and requires a simulation capable of modeling both the self-assembly process of interacting CNTs and the mechanical response resulting from these interactions. According to Puretzky et al. [88], CNT growth rates are non-linearly correlated to CNT diameter due the catalyst kinetics. Bedewy and Hart [82] utilized a two-CNT micro-mechanical unit cell to show that mechanical coupling among CNTs growing in contact may also present a significant limitation to the density and quality of CNTs in a forest. As numerous CNTs grow to form an increasingly more complicated and interactive network, the mechanical interactions within CNT forests become significantly more complex, and more resolved simulation techniques are required.

The mechanical modeling of CNT forests is challenging because of the complex structural morphology and the interconnectivity of CNTs within a forest. Previous studies investigating the mechanics of CNT forests have employed simplified forest geometries such as an isotropic continuum [108], array of interacting beam segments [82], distinct unit cells of oriented beams [100, 109], perfectly vertical and non-contacting beams [101, 110], or energy relaxation-based methods that populate CNTs in a volume and allow them to interact freely via van der Waals forces [111]. These modeling approaches are sufficient for approximating the mechanical response of CNT forests. However, they cannot capture the complex mechanics of forest self-assembly or the resultant forces transmitted to catalyst nanoparticles. A typical 2D and 3D simulated CNT forest morphology is shown in **Figure 8**.

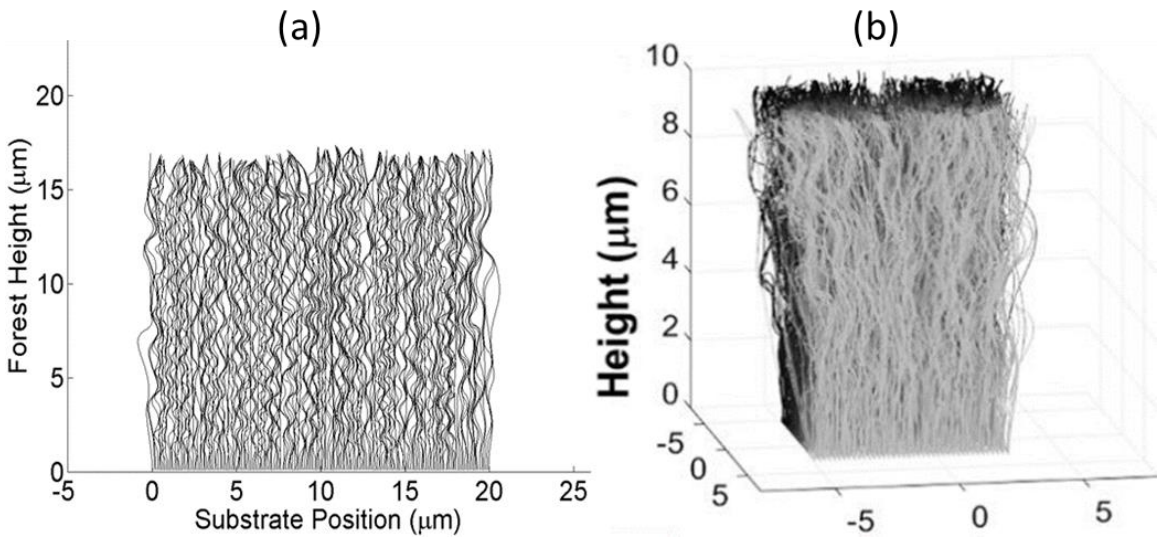

Figure 8. A typical simulated morphology of CNT forest obtained from the finite element simulation in (a) 2D (b) 3D

Here, we report a time-resolved mechanical finite element simulation of growing and interacting CNTs that readily facilitates the computation of distributed CNT forces as a function of CNT attributes [10]. The length of individual CNTs is sub-divided into discrete and interconnected "frame" elements, with nodes positioned on the end points of the element. Each nodal point supports bending, axial load, and transverse load (3 mechanical degrees of freedom per node). CNT-CNT van der Waals interactions are simulated as truss elements that resist relative motion between CNTs in contact. The growth of CNTs is accomplished by adding new elements to the base of each CNT at discrete time steps, approximating the base-growth mechanism that is frequently observed for CNT forests. First, the simulation construct is described for the growth and synthesis of CNT forests, followed by post-synthesis simulation models, namely compression and tension that resembles mechanical material characterization methods like nanoindentation [10, 112, 113]. Such simulations can yield mechanical, electrical and thermal properties of CNT forests.

Achieving a desired property set from CNT forests is currently an unfulfilled challenge. Most CNT synthesis recipes rely on previously successful results rather than a fundamental understanding of CNT forest kinetics and the assembly process. The CNT forest processing parameter space includes numerous variables. An experimental exploration of the full synthesis parameter space is both cost and time prohibitive. Numerical simulation of CNT forests synthesis and self-assembly is an alternative approach that may increase the speed and diversity of synthesis parameters examined. Such simulations can predict both the CNT forest

structural morphology and the resulting CNT forest properties. By systematically varying CNT synthesis parameters, one may arrive at a set of conditions that product the desired CNT forest performance metrics such as mechanical stiffness and thermal conductivity. These desired performance metrics are intricately related to the structural morphology of the CNT forest itself, although the functional relationships between CNT forest structural morphology and CNT forest properties are currently not well understood.

In the results section, after validating the simulation with two-CNT mechanics, a series of CNT forest growth simulations were examined using increasingly complex kinetics and parametric assumptions, with emphasis placed on the force and stress transmitted to the base of each CNT, corresponding to the location of active catalyst nanoparticles [105, 114]. CNT forests with homogeneous diameters were simulated to determine the scaling relationship between transmitted forces and CNT diameter. Next, forests with heterogeneous CNT diameters were examined using diameter-independent growth rates compared to a diameter-dependent growth rate [88]. Mechanical strain imparted to the CNT catalysts was allowed to alter the growth rate of CNTs using an Arrhenius-type relationship in which compressive forces decrease CNT growth rate and tensile forces increase CNT growth rates. The observed scaling laws and mechanochemical coupling observations may be used to understand and control CNT morphology for improved CNT forest properties. Also, the mechanical behavior of single and multiple-generation CNT forests as well as the delamination mechanics of carbon nanotube micropillars is investigated using the compression and tension simulation package.

2.2 Simulation Modeling Procedure

2.2.1 Growth

The simulation considers the concurrent growth and self-assembly of CNT populations by evaluated mechanical equilibrium of finite frame elements at discrete time increments [10]. Each simulated CNT, comprised of numerous elements connected end-to-end, underwent base growth at discrete time increments. Interactions and bonding between neighboring CNTs were approximated by a linearized van der Waals potential. Each element node supported three mechanical degrees of freedom representing axial, transverse, and angular deformation. The CNT attributes of inner and outer diameter, modulus, orientation angle, and

initial growth rate were assigned to each CNT stochastically at the beginning of the simulation based on user-defined distributions. The simulation does not consider structural imperfections of CNT walls or transient catalyst mass loss via Ostwald ripening or subsurface diffusion during growth [81, 115].

The CNT population growth sequence began with the nucleation of CNTs on a planar substrate. The global stiffness matrix of the CNT population, relating CNT deformation to nodal forces, was determined by assembling and rotating the local stiffness matrix of each constituent element into a global coordinate system. A representative stiffness matrix of a typical plane frame element is shown in **Figure 9**. Each CNT within a growing CNT forest was modeled as a finite frame element. Because each node contributed three mechanical degrees of freedom, each element represented a 6×6 matrix, k, within the global stiffness matrix.

$$k = \begin{bmatrix} \frac{EA}{L} & 0 & 0 & \frac{-EA}{L} & 0 & 0 \\ 0 & \frac{12EI}{L^3} & \frac{6EI}{L^2} & 0 & \frac{-12EI}{L^3} & \frac{6EI}{L^2} \\ 0 & \frac{6EI}{L^2} & \frac{4EI}{L} & 0 & \frac{-6EI}{L^2} & \frac{2EI}{L} \\ \frac{-EA}{L} & 0 & 0 & \frac{EA}{L} & 0 & 0 \\ 0 & \frac{-12EI}{L^3} & \frac{-6EI}{L^2} & 0 & \frac{12EI}{L^3} & \frac{-6EI}{L^2} \\ 0 & \frac{6EI}{L^2} & \frac{2EI}{L} & 0 & \frac{-6EI}{L^2} & \frac{4EI}{L} \end{bmatrix}$$

Figure 9. Stiffness matrix of a plane frame element [105].

where, E is the elastic modulus of the element, A is the cross-sectional area of the element, L is the length of the element, and I is the second moment of inertial of the element. The stiffness matrix of each element is rotated to a global coordinate system and compiled into a global stiffness matrix that represents each element of the CNT forest. Additional details may be found in [10].

A schematic of a typical frame element assembly used to model CNT forest growth over different growth time steps is shown in **Figure 10**, showing the base growth mechanism. The growth of each CNT is achieved at the beginning of each discrete time step, as depicted in **Figure 10**. Mechanical equilibrium is computed at each node for each time step, based upon interactions of adjacent CNTs and the global stiffness matrix of the system. As CNTs lengthen with time, they encounter neighboring CNTs and form van der Waals bonds, represented as linear spring elements. The van der Waals bonds persist, causing contacting CNTs to deform in response to disparate CNT growth rates.

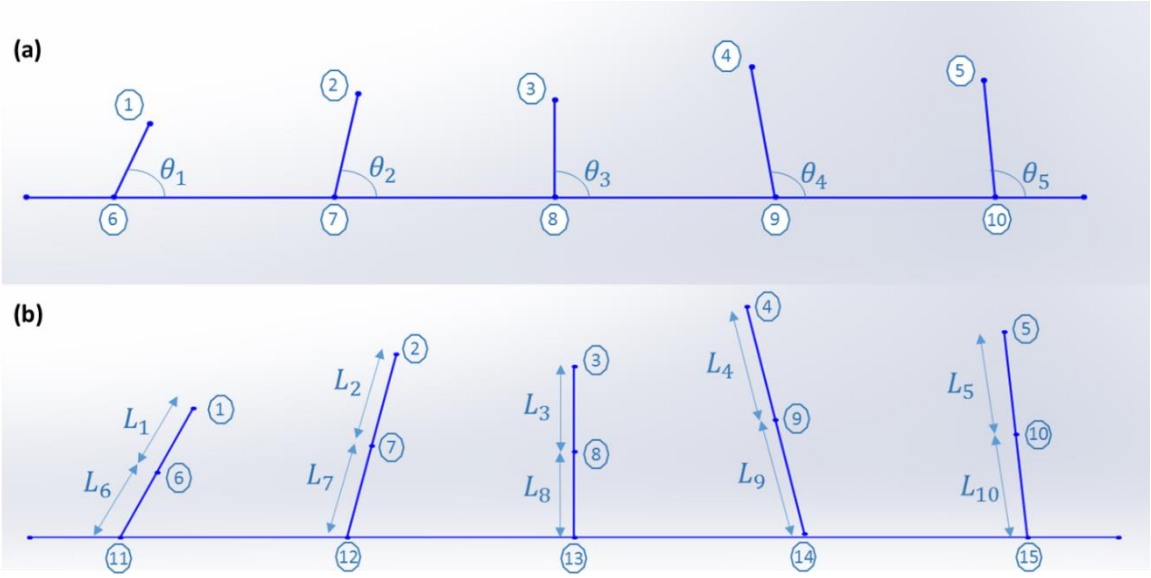

Figure 10. The schematic of a typical frame element employed to model carbon nanotube forest growth. (a) The nucleation of CNT forest with five nanotubes where each nanotube is assigned user-defined growth rates, angle of orientation, inner and outer diameter, etc. (b) The lengthening of bottom most elements representing a bottom growth mechanism. Each nanotube is stretched twice the length of bottom-most element along the same angle of orientation [105].

Van der Waals interactions between adjacent nodes were found by evaluating the relative pair-wise distance between all nodes in the system. Nodes within a predefined gap of 50 nm or less (measured between the central axis of two CNTs), were assumed to experience a van der Waals attraction. To model van der Waals potential, a linear-elastic bar element was introduced between the nodes in contact. The van der Waals stiffness elements between contacting nodes were then added to the global stiffness matrix.

To facilitate the growth of each CNT in the population, the bottom-most node of each CNT was displaced by a magnitude representing the growth rate and orientation angle of the CNT. The displacements of all other nodes in the system due to the stretching of the bottom-most elements was computed using the updated Lagrangian modeling approach whereby

$$\{R\}_t - \{F\}_{t-1} = [K]_t\{U\}_t \tag{2}$$

where F is a vector of internal forces, R is a vector of external forces, K is the global stiffness matrix, U is the nodal displacement matrix, and the subscript t represents the current time step. After determining nodal displacements for a given time step, the nodal positions were then updated by adding the computed displacements to the previous position of each node. A new time step began by updating the global stiffness

matrix based on the updated nodal positions and CNT-CNT contacts, and the process repeated for a user-defined number of time steps.

Because contacting CNTs were growing at mismatched rates and angles, reaction forces were generated by CNTs in contact. The forces were presumed to be insufficient for CNT contacts to slide or break [9, 82]. The reaction forces may be evaluated for each node in the simulated CNT forest by multiplying the local stiffness matrix and the appropriate nodal deformation, given by:

$$\{F\} = [k][r]\{U\} \tag{3}$$

where F denotes a force vector, k is the local stiffness matrix of the element, r is a rotation matrix to transform global coordinates into local coordinates, and U is the displacement vector expressed in global coordinates. If desired, the local forces may also be translated into the global coordinate system using the appropriate rotation matrix.

2.2.2 Compression

CNT forests are compressed using another simulation model to obtain the force necessary to buckle CNT forests. Compression of forests was simulated by a vertically translating and rigid platen that contacts the top surface of the forests. After the compressive load was applied to the top surface of forest, similar finite-element analysis concepts are used to solve for displacement and forces. The compression is applied by a constant platen translation per compression step and normal to the forest while the substrate is conceived as a rigid body. The reaction forces are calculated at each node in contact with the moving platen and summed up to obtain the compression force. The force applied to the top surface was identical to the force transmitted to the growth surface. The compression simulation is discussed in detail in [10]. The compression simulation resembles a nanoindentation experimentation where the compressive behavior of the CNT forests was examined using an Agilent G200 nanoindenter. The indentation technique employed multiple loading and unloading cycles, each at progressively increasing loads. A maximum load is selected to ensure that compression of the forests exceeded the linear elastic and plateau regions of the force-displacement response. The compression simulation may be employed to obtain CNT forest mechanical properties like stiffness and buckling load, thermal and electrical conductivity (electrical resistance).

2.2.3 Tension

To better understand how the non-uniform load sharing and complex CNT forest morphology influence the experimentally measured delamination force of a CNT forest pillar, a similar construct to growth and compression finite element simulation is used representing a tension experiment. Here, CNT forest delamination stress is defined as the force required to remove a monolithic forest structure from the growth substrate divided by its apparent cross-sectional area, while CNT adhesion strength is defined as the stress required to remove a single CNT from the growth substrate. Uniaxial tension tests were conducted by attaching a micro-scale probe to CNT forest micropillars using an epoxy interface as discussed in details in [112]. Briefly, uniaxial tensile displacement was applied to the top surface of CNT forests pillars by moving the sample stage away from the sapphire tip using the piezoelectric stage motor (see **Figure 27**).

2.3 Results and discussions

The time-resolved simulation enables the evaluation of a wide range of CNT attributes and their influence on the forces exerted during forest assembly. The development of the model framework has been reported elsewhere [10, 105, 112, 114]. Prior to using the simulation to model large CNT populations, the forces generated by the finite element model were investigated using a simplified system comprised of two CNTs. Two continuously growing and interacting CNTs were next simulated to investigate the behavior and magnitude of forces transmitted to the base of the CNT, where the catalyst particle is assumed to reside.

2.3.1 Model validation for a two-CNT growth

Model validation utilized a cantilever beam subjected to prescribed loads such that all degrees of freedom were interrogated. In all cases, a 1 μm long cylindrical beam with a Young's Modulus of 1 TPa, outer diameter of 20 nm, and inner diameter of 14 nm served as the physical CNT parameters. The simulated loads and deflections agreed with analytical results, suggesting that the foundational stiffness matrix and solver of the CNT forest simulation is valid.

The time-resolved interactions between two concurrently growing CNTs (20 nm O.D. and 14 nm I.D.) were then simulated to establish baseline reaction forces generated by isolated two-CNT interactions. A

vertically oriented CNT grew at a rate of 50 nm per time step while an angled CNT originating 100 nm away from the vertical CNT grew at 60 nm per time step, resulting in a growth rate mismatch of 10 nm per time step between the pair. The angled CNT was oriented such that CNT-CNT contact occurred at a height of 1.25 μm from the growth substrate. Emphasis was placed on evaluating the axial force transmitted to the base of each CNT, as this force represented the mechanical load transmitted to catalyst particles, as examined in greater detail later. Each CNT initially grew unconstrained in a straight line at a prescribed angle and rate. Upon contact with a neighboring CNT, the CNTs were locally bonded by van der Waals interactions. The CNT pair then bent away from the faster growing CNT with increased interaction time. The axial force imparted to the base of each CNT spiked upon the establishment of the CNT-CNT contact. The time-resolved CNT morphology and axial force measured at the base of each CNT are shown in **Figure 11**.

This simulation setup is similar to experimental findings from recent E-TEM results [116] in which mechanically coupling between CNTs growing at different rates is observed. The magnitude of the axial force generally diminished as the CNTs lengthened with time. For the simulated conditions, the maximum magnitude of force was approximately 3-4 nN, corresponding to an axial stress of 19-25 MPa. The slower-growing CNT was pulled upward by the faster growing CNT, imparting tensile loading, denoted by a positive force magnitude. Conversely, the faster growing CNT was impeded by the slower growing CNT, imparting compressive (negative magnitude) loading at its base. The magnitude of axial force reduced as the CNTs continued to lengthen. Such behavior is analogous to the force required to deflect a lengthening cantilever beam, whereby force is inversely proportional to the third power of beam length. Note that the magnitude of axial force expressed in **Figure 11** are not equal in magnitude and opposite in sign because the force vectors are aligned with the local growth axis of each individual CNT. In global coordinates, the forces are balanced at all times.

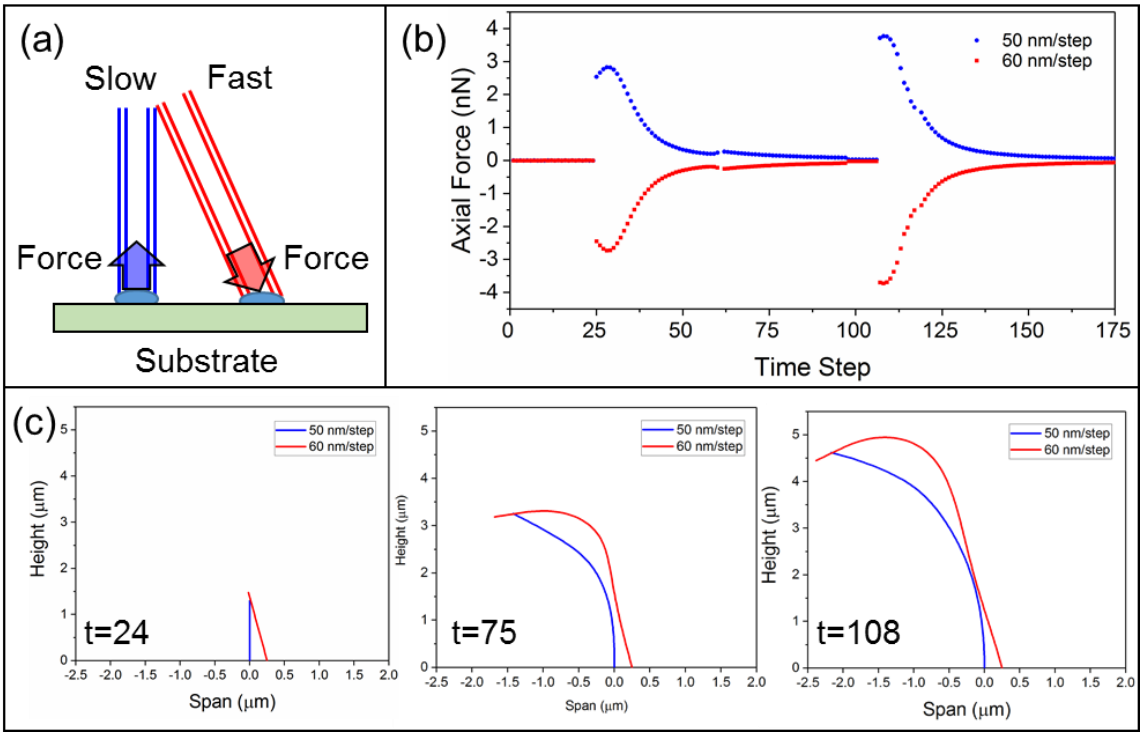

Figure 11. Time-resolved axial forces transmitted to the base of CNTs. (a) A schematic depicting the direction of forces transmitted to the catalyst particle residing on a rigid substrate. (b) Time-resolved force evolution for two CNTs growing at 50 and 60 nm/step. (c)The morphology of 2 interacting CNTs shown at 24 (first contact), 75 and 108 time steps [114].

Note that the forces observed between the 2-CNT interactions are validated using a static simulation with both COMSOL Multiphysics finite element software and the current CNT simulation solver, as shown in **Figure 12** and **Table 1** [114, 117]. The validation consisted of two simulated CNTs in contact. The two CNTs include the segment consisting of nodes 1 and 2 and the segment formed by nodes 2 and 3 shown in Fig. S3. The two CNTs were connected at node 2. Node 3 was displaced 10 nm upward, in the direction of node 2. Each element has an O.D. of the element of 20 nm, with an I.D. of 14 nm. The COMSOL simulations results were then compared to those produced from a similar simulation run using the CNT finite element code used to investigate the time-resolved CNT forest forces. The COMSOL simulation setup and results may be seen in **Figure 12**. The resulting reaction forces at node 1 and 3 may be found in **Table 1**. All forces at node 2 were zero. Note that the COMSOL simulation agrees with the CNT finite element simulation with significantly less than 1% error.

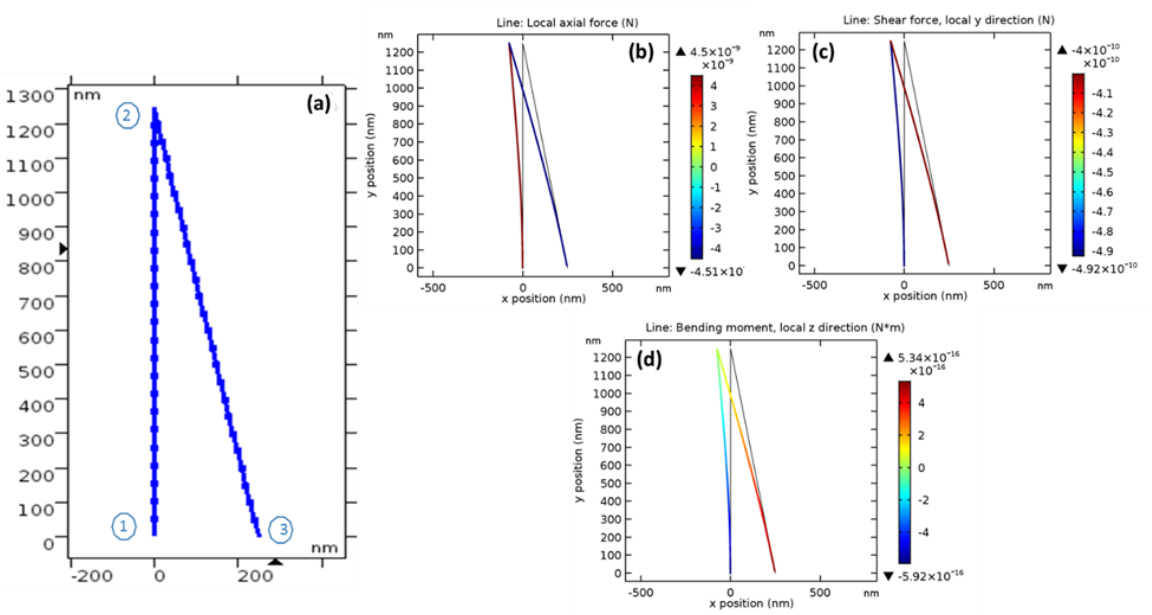

Figure 12. The 2-CNT simulation model in COMSOL. (a) Element nodes, including nodes of interest: 1, 2, and 3. (b) The axial force, F_y, (c) shear force, F_x, and (d) moment, M resulting from 10 nm displacement applied at node 3 [114].

Table 1. Results of Model Validation with COMSOL [114].

	COMSOL	CNT Model	Difference (%)
Point 1: F_x (nN)	0.492	0.491	-0.3356
Point 3: F_x (nN)	-0.49	-0.491	-0.3356
Point 1: F_y (nN)	-4.509	-4.509	0.0000
Point 3: F_y (nN)	4.503	4.509	0.1300
Point 1: Moment (nN-µm)	-0.592	-0.591	-0.1118
Point 3: Moment (nN-µm)	-0.534	-0.536	0.3979

2.3.2 Time-resolved forces within a growing CNT forest

Larger CNT populations were next examined, with emphasis again placed on axial forces transmitted to the catalyst particles. Populations of 100 CNTs were grown on a 10 µm simulation domain (10 CNT/µm) for a duration of 200 time steps. CNT growth rates were assigned stochastically based on a Gaussian probability density function. The average CNT growth rate was 50 nm/step with a standard deviation of 5 nm/step. For initial simulations, CNT populations were assigned a uniform outer diameter, with inner diameters equal to 70% of the outer diameters. The growth angles of the CNTs were distributed with a 5° standard deviation

from the substrate normal. The mechanical force transmitted to the base of each CNT was recorded at each time step.

Figure 13 displays the final morphology and the time-resolved axial forces transmitted to the substrate by the slowest and fastest-growing CNT within a forest consisting of 10 nm outer diameter CNTs. Note that the blue CNT in **Figure 13a** represents the slowest growing CNT in the forest, while the red CNT represents the fastest growing CNT. As anticipated, the slowest-growing CNT in the forest is oriented vertically in tension, while the fastest-growing CNT demonstrates significant waviness and is bound between its two neighboring CNTs. The slowest-growing CNT does not have the back-and-forth waviness of the fastest growing CNT, but it is laterally deflected by contact with neighboring CNTs. The forces transmitted to the base of the slowest and fastest CNT within a growing population are displayed in **Figure 13b**. Note that the force magnitude range experienced by the two CNTs is similar, though each have an opposite sign convention. The slowest-growing CNT is in tension at its base, while the fastest growing CNT transmits a force in compression. Each spike in force represents establishment of a new CNT-CNT connection. Note that the fastest-growing CNT experienced a greater quantity of force spikes than the slowest-growing CNT, as it more frequently contacts its neighboring CNTs. Furthermore, the slowest-growing CNT was in a constant state of non-zero tension after the initiation of contact while the fastest-growing CNT relaxes to a nearly neutral axial force between establishment of new contacts.

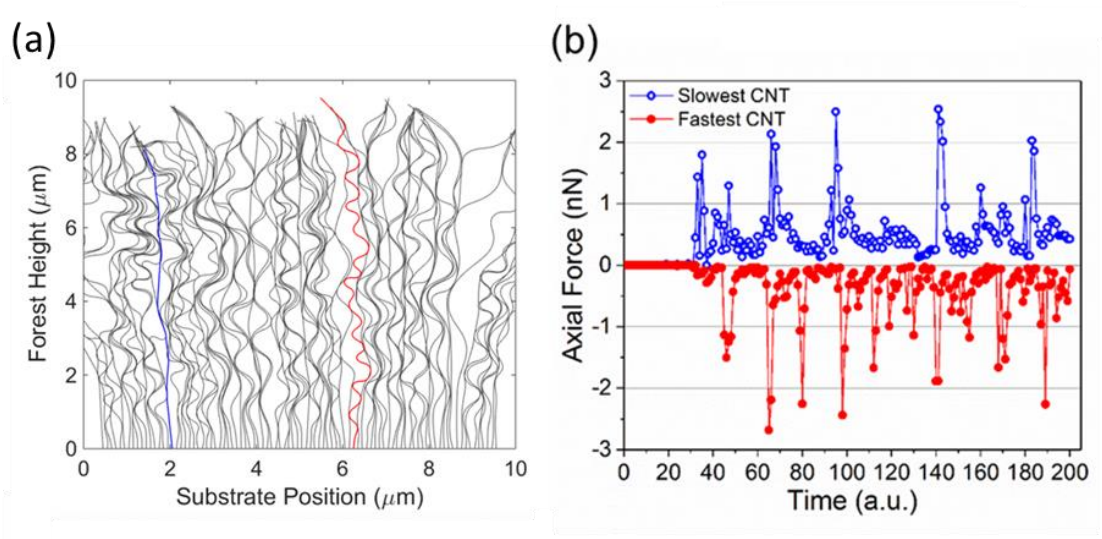

Figure 13. (a) The final CNT morphology and (b) time-resolved axial force of the fastest- and slowest-growing CNTs exerted to the substrate in a 100 CNT forest. The morphology of fastest-growing (red) CNT in the forest undergoes a highly tortuous path, while the slowest-growing (blue) CNT is pulled in tension. All CNTs in the forest were assigned 10 nm outer diameter. The standard deviation of population growth rate was 5 nm per time step with a mean growth rate of 50 nm per time step [114].

2.3.3 The effect of CNT diameter

The force transmitted to the substrate was recorded for all CNTs within the population for all time steps, facilitating an evaluation of axial force as a function of each individual CNT's growth rate. A total of 10 distinct CNT forests were simulated using the same probability distribution functions for growth rate and orientation angle, and the same physical CNT parameters. CNT forests consisting of uniform CNT outer diameters of 5, 10, 20 and 40 nm were simulated for direct comparison of axial forces as a function of CNT diameter. The inner diameters were 70% of the outer diameter for all cases. Note that the 10 simulations performed for 5, 10, 20, and 40 nm diameter CNTs shared otherwise identical parameters, including growth rate and orientation assignments.

As observed in **Figure 13**, the force transmitted to the base of each CNT varied greatly with time as the self-assembly of CNT forests proceeded and new CNT-CNT contacts were established. To examine the effect of diameter to the magnitude of forces transmitted to the catalyst particles, the time-averaged axial force for each CNT was computed after the first 50 simulation time steps. Within this sampling period, all CNTs have established contact with neighboring CNTs, ensuring that zero-force entries prior to CNT-CNT contact were not considered within the force average. The time-averaged axial force for each CNT and for all 10 simulations was plotted as a function of CNT growth rate in **Figure 14a-d**. The minimum and maximum

growth rate ranged from 23 to 79 nm/step. A strong negative correlation between CNT growth rate and time-averaged axial force was observed, with approximately zero average load observed at the population average growth rate of 50 nm per time step. Note that the time-averaged forces were examined for simulation durations of up to 500 steps (see **Figure 16**), with little change in the average force values; therefore, the results presented in **Figure 14** are independent of the time window over which the forces were averaged. This is discussed in more detail in the next section.

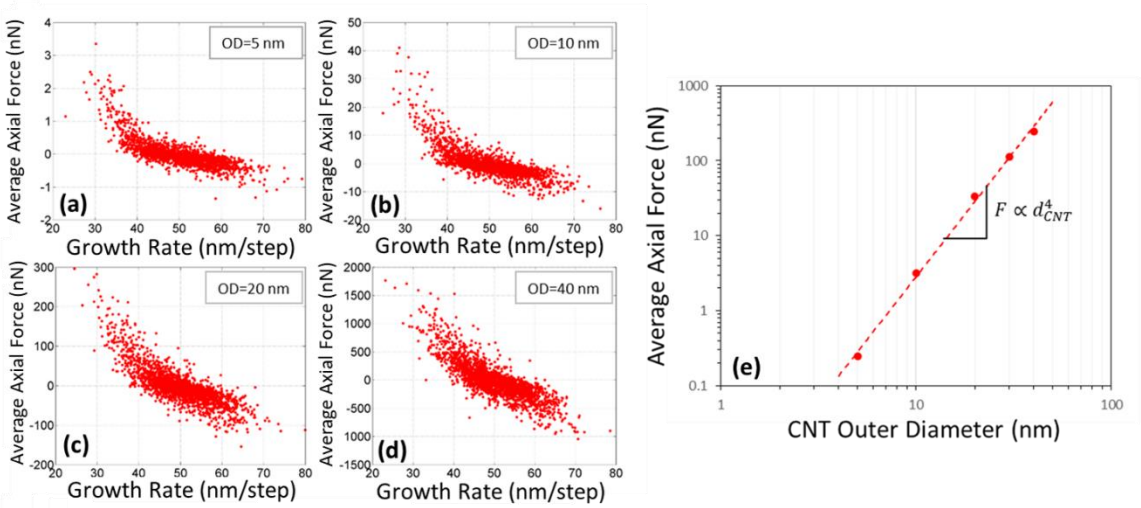

Figure 14. The time-averaged axial force transmitted to the base of growing CNTs as a function of the CNT growth rate and diameter. The average axial force transmitted to the CNT base as a function of CNT growth rate for populations with a homogeneous outer diameter of (a) 5 nm, (b) 10 nm, (c) 20 nm, and (d) 40 nm. (e) The average axial force magnitude scales approximately as CNT outer diameter to the forth power [114].

The magnitude of force generated within the CNT forests varied strongly with CNT diameter. The time-averaged force magnitude of data plotted in **Figure 14a-d** was obtained for all forests of uniform diameter ranging from 5 – 40 nm. The resulting time-averaged force magnitude (absolute value) resulting from all simulations of like diameter is shown in **Figure 14e**. CNT forests consisting of 5 nm OD CNTs produced an average force magnitude of approximately 0.25 nN, while 40 nm OD CNT forests generated average force magnitude of approximately 245 nN. The average force magnitude scales approximately as the CNT forth power of diameter, as shown by the log-plot in **Figure 14e**. This scaling trend suggests that the tensile force experienced by slower-growing CNTs is generated by the bending stiffness of the faster-growing CNT population. In particular, the bending stiffness may be represented as:

$$EI = \frac{\pi E}{64}(d_o^4 - d_i^4) \tag{4}$$

where E is the Young's modulus, I is the second area moment of inertia, and d_o and d_i represent the outer and inner CNT diameter, respectively.

2.3.4 Grid Independence

The grid size of the simulation, represented as growth rate in the current model, was varied from a population average of 30 nm/step to 80 nm/step to test for independence of results. The growth rate standard deviation is scaled relative to the population average growth rate, and is equal to 5% of the average growth rate for all simulations. Results shown in **Error! Reference source not found.** demonstrate that the magnitude of forces and the relationship between growth rate and average force are retained for all tested values of average growth rate. A value of 50 nm/step was selected as a default value for simulations, as it is slightly larger than the nodal distance at which van der Waals forces are active.

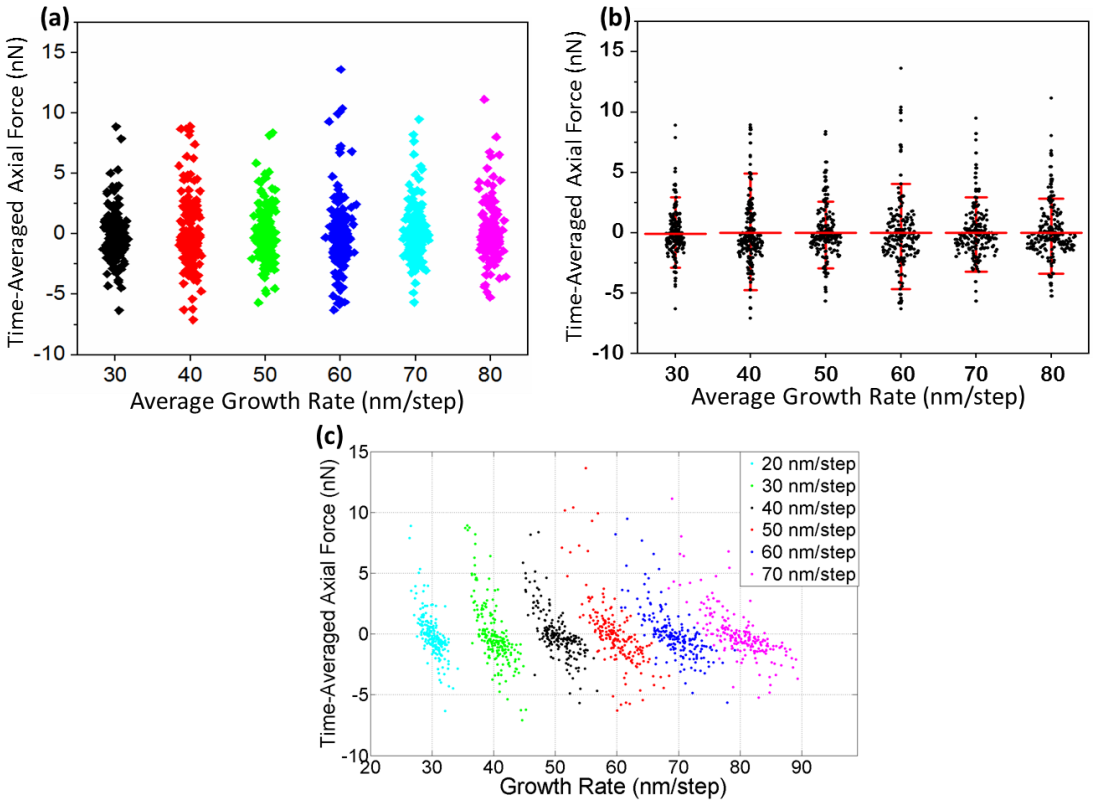

Figure 15. The mesh-size independence tests of time-averaged axial force transmitted to catalyst particles versus average growth rates of 30-80 nm/step shown as (a) jitter plot (b) box plot (c) versus growth rates [114].

2.3.5 Time Independence of Average Axial Force

The reaction forces generated within a growing CNT forest are transient in response to the formation and evolution of CNT-CNT van der Waals bonds. The time-averaged forces were examined at 200, 300, 400, and 500 time steps for a given forest to examine the magnitude of variability with time. The average axial force vs. growth rate is shown in **Figure 16a** and shows that minimal variation exists within these sampling intervals. As further evidence, the cumulative probability for these same sampling intervals is shown in **Figure 16b**. Again, negligible variation between the sampling intervals is observed.

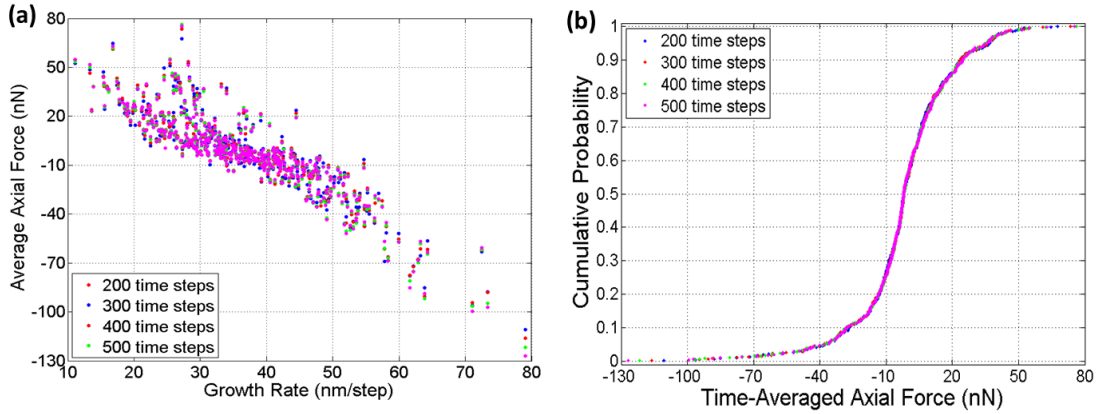

Figure 16. The time-averaged axial force transmitted to catalyst particles as a function of CNT outer diameter versus (a) growth rate (b) cumulative probability, at time steps 200, 300, 400 and 500 [114].

2.3.6 Heterogeneous CNT diameter

While CNT diameter greatly influences the magnitude of forces generated in CNT forests comprised of uniform diameter CNTs, the CNT diameters in actual CNT forests are heterogeneous rather than single-valued [83, 84]. To incorporate this natural diameter variation, a Gaussian distribution of CNT outer diameters in the range of 4-16 nm [84] were introduced into simulations, with a mean value of 10 nm. The relationship between CNT diameter and CNT growth rate is uncertain for CNT forests. Puretzky et al. [88] suggested that the reaction kinetics of CNT catalyst particles is diameter dependent, whereby larger-diameter CNTs grow more quickly than smaller-diameter CNTs. This kinetic model is incorporated into the current simulations using a quadratic function, similar to recent work [82]

$$\text{Growth Rate} = f(0.11d^2 - 0.02d + 0.36) \quad (5)$$

where d is outer diameter of each CNT and f is a scaling function. Note that the growth rate increases nonlinearly with diameter in this model. On the other hand, in-situ CNT synthesis observations of Yoshida

et al. [92] indicate that growth rate is diameter-independent. Because of the uncertainty between CNT diameter and growth rate, two distinct CNT forests were simulated with exactly same inputs except for the relationship between CNT outer diameter and growth rate, i.e. diameter-dependent and diameter-independent growth rates.

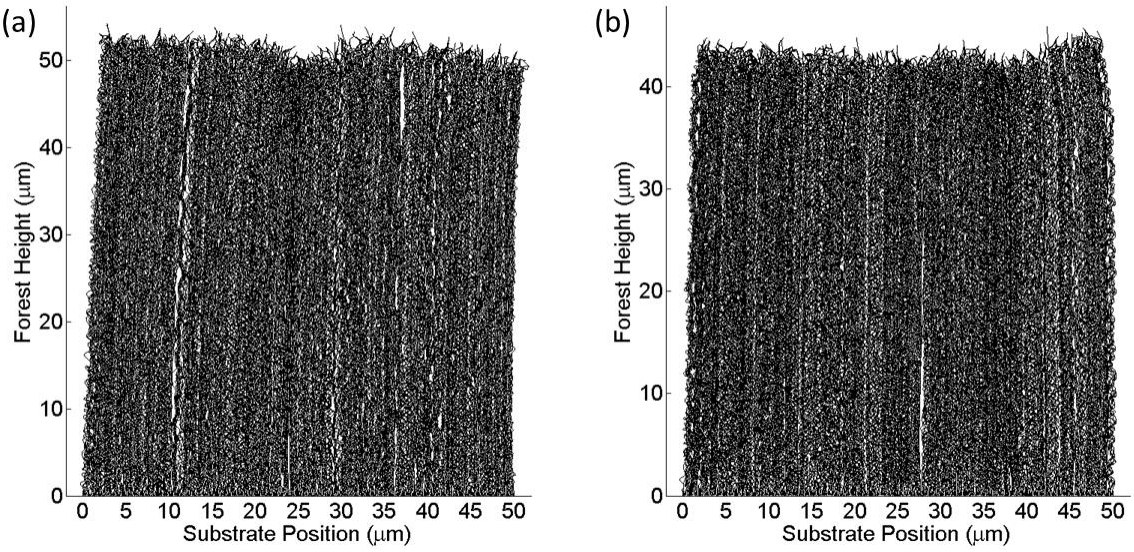

Figure 17. Final CNT morphology of a typical 500-CNT forest featuring (a) diameter-dependent growth rates, and (b) randomly distributed, diameter-independent, growth rates after 2,000 time steps [114].

Introducing heterogeneous CNT diameters into a simulation is expected to alter the magnitude and distribution of forces transmitted to the base of the CNTs. Two sets of simulations were executed using two different assumptions about how CNT growth rate was influenced by CNT diameter. Diameter-dependent growth rates were directly calculated using Eq. (5). Diameter-independent growth rates used the same set of growth rates as the diameter-dependent growth; however, the diameters and growth rates were randomly paired with no correlation. The typical growth rates for CNT outer diameters between 4-16 ranged from approximately 10-90 nm/step, with an average growth rate of approximately 37 nm/step. The resulting CNT morphologies were similar after 2,000 growth steps, as shown in **Figure 17**. Histograms of the diameter distribution and growth rate and a plot showing the growth rate as a function of CNT outer diameter may be found in **Figure 18**. Similar simulations were then executed in which all parameters were identical except for the assignment of growth rate. In these diameter-independent growth rate simulations, the same growth rates used in the diameter-dependent growth rates were then randomly assigned to the CNTs in the forest,

regardless of their diameter. In this way the simulations were identical in all ways except for the relationship in which growth rates were assigned to CNT diameters. The simulations were run for 250 time steps on a 50 μm wide domain using 500 CNTs. 100 simulation of each type were performed, with the axial forces transmitted to the catalyst particles recorded and averages from time steps 50-250. The axial forces were also converted to stress to more readily account for the variations in diameter.

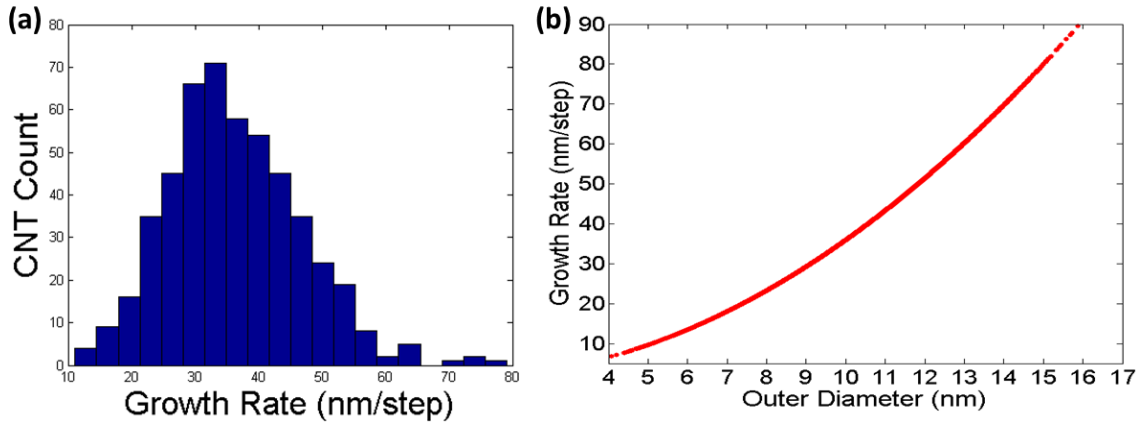

Figure 18. (a) Histogram of the diameter distribution and (b) growth rate as a function of CNT outer diameter corresponding to Eq. (5) [114].

Figure 19 displays the average axial force and axial stress as a function of both outer diameter and growth rate. **Figure 19a** shows that the average forces ranged from almost 120 nN to -235 nN for the diameter-dependent growth rate and from approximately 320 nN to -160 nN for diameter-independent growth rate forest. Forces as a function of diameter followed a nonlinear trend for the diameter-dependent rates with a sign change from positive (tensile) to negative (compressive) forces near the average diameter of 10 nm. CNTs with diameters smaller than ensemble average diameter represent CNTs growing at a rate less than the average growth rate. These small-diameter CNTs experienced tensile forces generated by interactions with faster-growing and larger-diameter CNTs. The larger-diameter (faster-growing) CNTs experienced compressive forces at their base for the same reason. Conversely, in simulations where CNT growth rate and diameter were uncoupled, seemingly no correlation between diameter and the directionality of force was

exhibited. Rather, the envelope representing the time-averaged force magnitude increased, both in compression and tension, as a function of increasing diameter.

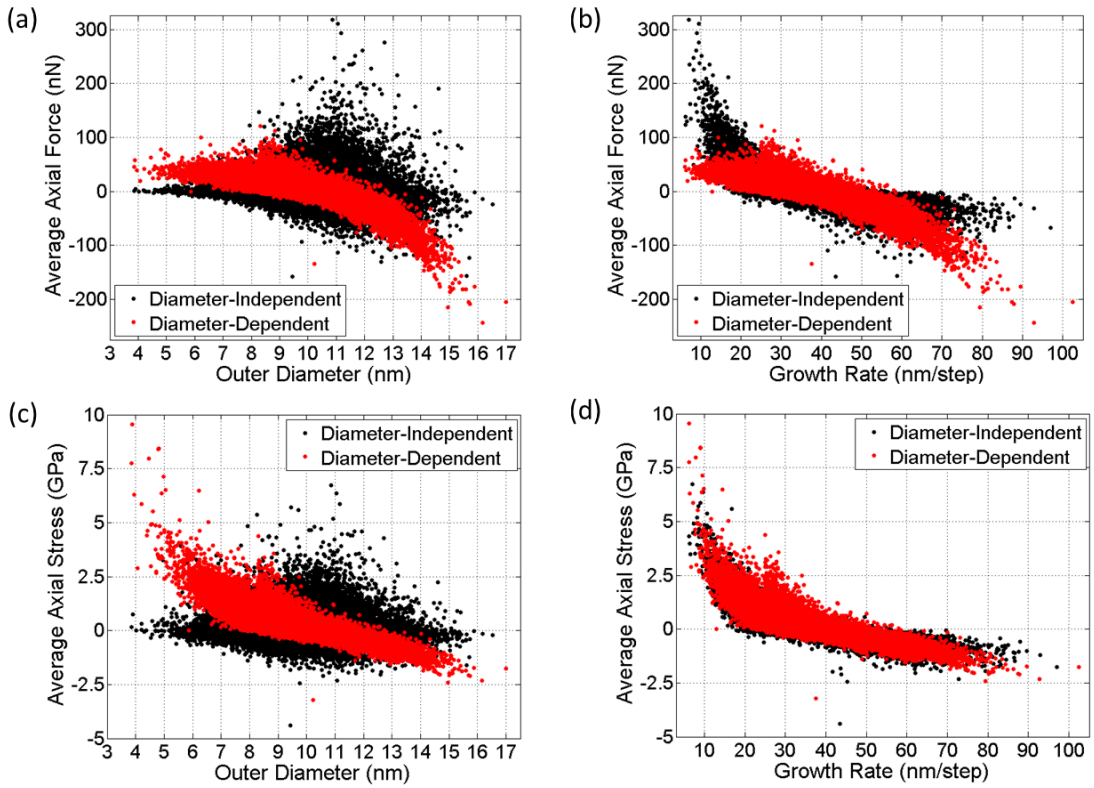

Figure 19. The time-averaged axial forces transmitted to the base of CNTs for CNT forests grown using diameter-dependent and diameter-independent growth rates as a function of (a) CNT outer diameter (b) CNT growth rates. The time-averaged axial stress transmitted to the base of CNT forest for diameter-dependent and diameter-independent growth rates plotted as a function of (c) CNT outer diameter and (d) CNT growth rates. The data was obtained from 100 distinct simulations of each type [114].

When these same average forces were examined versus CNT growth rate, as displayed in **Figure 19b**, a negative correlation between force and growth rate was observed for both sets of data. Neutral loading was observed for both sets of data near the population averaged growth rate of 37 nm/step. Recall that the diameter-dependent model correlates a high growth rate with large-diameter CNTs. As a result, the fastest-growing CNTs also exhibit the greatest bending stiffness (Eq. (4)) and generate the largest (compressive) loads in the diameter-dependent growth rate model. This trend is collaborated in both **Figure 19a** and **Figure 19b**. With a diameter-independent growth rate, small-diameter CNTs may grow rapidly, generating smaller compressive loads because of a much-decreased bending stiffness. In addition, the diameter-dependent growth rate model dictates that the slowest-growing CNTs in a population have the smallest

diameter. The diameter-independent growth rate permits large-diameter CNTs to grow slowly. The increased tensile stiffness offered by an increased cross-sectional area decreases the tensile deformation of slow-growing CNTs while simultaneously increasing the bending deformation of contacting CNTs. The net result of such an interaction is an increased tensile loading of slow-growing CNTs for the diameter-independent growth rate when compared to the diameter-dependent growth rate. This trend is confirmed in **Figure 19b**, where the slowest-growing CNTs exhibit a load of up to 300 nN in tension.

Normalizing the axial load by the cross-sectional area of the CNT converts force to axial stress, which is a more direct representation of energy density transmitted to a catalyst particle. The time-averaged axial stress for the diameter-intendent and diameter-dependent growth rate distributions as a function of CNT outer diameter is shown in **Figure 19c**. For the parameters used in these simulations, the time-averaged stress transmitted to the catalysts ranged from -3.2 GPa to 9.5 GPa, with a majority of data residing closer to neutral stress. Interestingly, these stress values are greater than the yield strength for iron and high-strength steels, indicating that the observed stress may be sufficient to plastically deform a catalyst particle and modulate the catalytic activity. The highest tensile stress was generated in the smallest-diameter CNTs in the diameter-dependent growth rate model, as these CNTs represent the slowest-growing CNTs in the population. Interestingly, the largest magnitude of tensile and compressive stress in the diameter-independent growth rate model was near the mean diameter of 10 nm. We believe that this trend arises because of the Gaussian distribution of CNT diameters in which a large fraction of CNTs in the population resided near the average diameter. This trend was confirmed when the average stress is plotted as a function of CNT growth rate, as shown in **Figure 19d**. Remarkably, the average axial stress as a function of CNT growth rate overlap for the diameter-dependent and independent growths. The overlap in results indicates that the mechanical stress transmitted from the assembling CNT forest to the catalyst particles is most strongly related to the growth rate of the individual CNT and is insensitive to the relationship between CNT diameter and growth rate. This overlap may be an artifact resulting from the quadratic nature of the diameter-dependent growth rates shown by Eq. (5). The time-averaged axial forces are divided by cross-sectional area to obtain time-averaged axial stresses. Division by the area, which also scales with the second power of diameter, may be responsible for the overlap in data. Recall that the same CNT diameters and growth rates were used for each simulation type - only the method of assigning growth rates to CNTs of different diameters differed. After many stochastic

growth runs, the mechanical strain energy produced by the two growth rate models generated, on average, similar values. The results in **Figure 19d** indicate that CNT growth rate is on average the dominant predictor of force transmitted to the catalyst particle, regardless of which growth rate model is used.

2.3.7 The Effect of van der Waals Bonds

As discussed earlier, when CNTs establish contact with neighbors, van der Waals forces act to hold contacting CNTs together. Collectively growing CNT pairs are subject to deformation and mechanical loading. Although the van der Waals bonds have been observed to persist in compressed CNT forests [106], they are not permanent and may break if tensile forces exceed a maximum value. If two CNTs in contact may be treated as parallel hollow cylinders, the force per unit length of contact is calculated as [84]:

$$\frac{-A}{8\sqrt{2}D^{\frac{5}{2}}}\left(\frac{R_1R_2}{R_1+R_2}\right)^{1/2} \tag{6}$$

where A is Hamaker constant, D is distance between outer diameters of two adjacent CNTs, and R_1 and R_2 are outer radii of neighboring nanotubes. To obtain an order of magnitude for this value, average values of CNT radius and length were analyzed, and the separation distance between contacting CNTs was assumed to be the interatomic layer spacing of graphite sheets, 0.34 nm. Also note that the value of the Hamaker constant was assumed to be 5×10^{-20}J [84]. For such a scenario, the average force required to break the van der Waals bond is 5 nN. Based on this representative value, van der Waals bonds experiencing a tensile force that exceeded this value were removed from the simulation, and liberated nodes were free to interact in the absence of the bond.

Introducing this condition to van der Waals contacts had minimal influence on the CNT morphology, as shown in **Figure 20a**. The CNT forest displayed represents the identical simulation conditions used to generate the CNT forest shown in **Figure 20b** with the addition of the conditional van der Waals bond. Only subtle differences between the two CNT morphologies may be observed. Obviously, the morphology dissimilarity and achieved heights would be more diverse if the simulation had been run for more time steps.

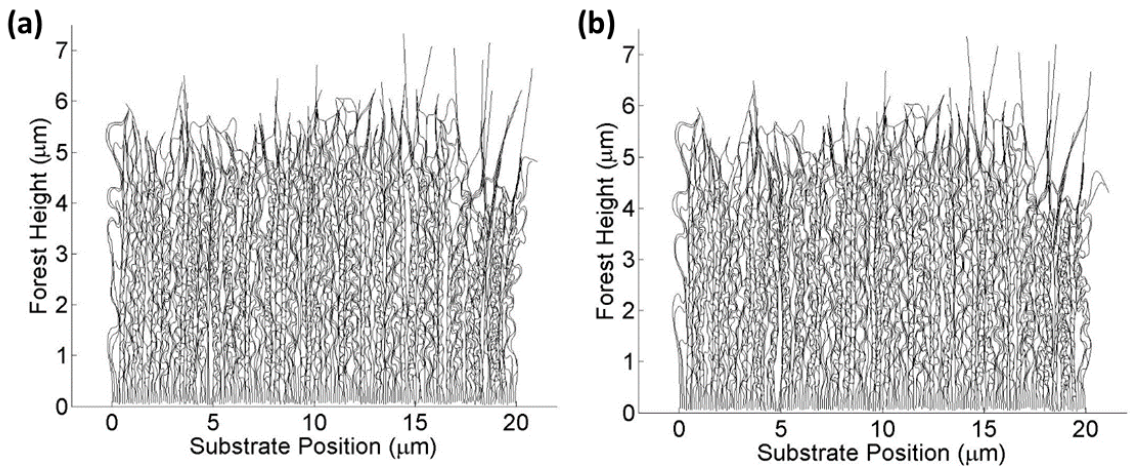

Figure 20. CNT morphology of a 200 CNT forest allowing vdW bond breakage [105].

To better understand the subtle changes of the CNT morphology, the quantity of broken van der Waals contacts was evaluated at the end of each time step. Note that the number of nodes introduced during each time step is 200 corresponding to one additional node per CNT. One would also anticipate that the number of CNT-CNT bonds would also increase as a function of time as new nodes are introduced the system and deformation within the forest increases. As shown in **Figure 21**, no bonds were broken during the first 20 time steps. During this time the CNTs had not yet established neighboring contacts. As the length of CNTs and the number of CNT-CNT contacts increases. The number of broken CNT-CNT bonds also increases. In fact, the number of broken bonds increases nearly linearly until approximately 80 time steps, when the number of broken CNT-CNT bonds plateaus at about 2,000 time steps. The nature of this trend is under investigation; however, we believe that the distribution of CNT-CNT forces is greatest near the substrate. It is here that CNTs exhibit the greatest force to resist bending (proportional to $1/L^3$). These forces relax as CNTs grow longer, such that CNT-CNT bonds located sufficiently far from the growth substrate have less force acting on them and a lower probability of breaking.

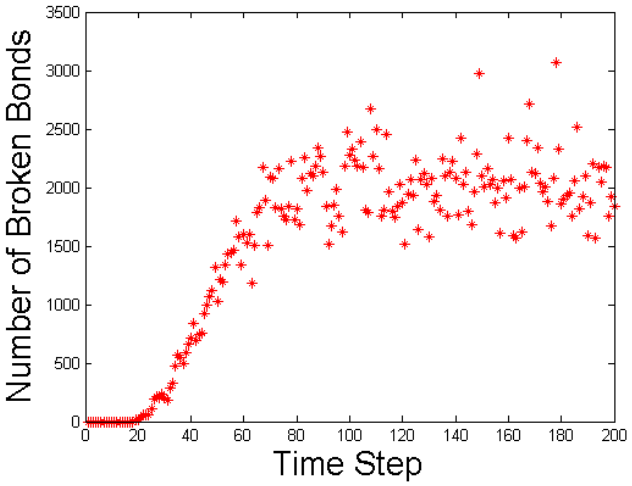

Figure 21. The number of broken bonds per time step due to excessive tensile forces [105].

2.3.8 The effect of CNT forest areal density

The areal density of CNTs is also expected to influence the magnitude of forces generated in assembling CNT forests, as the areal density will impact the frequency of CNT-CNT contacts. A set of 100 simulations each was examined in which the diameter-dependent growth rate model was implemented for cases of 250, 500 and 750 CNTs within a 50 μm simulation domain. A similar inter-CNT spacing in a 3D CNT forest would correspond to 2.5×10^{9}, 10^{10}, and 2.25×10^{10} CNTs/cm^2, respectively. By comparison, the density of a typical CNT forest is 10^{9}–10^{10} CNTs per square centimeter [82-84]. The time-averaged forces transmitted to the catalyst particles were computed and displayed as cumulative probability density in **Figure 22**. The total simulation time was 250 time steps for each simulation, and forces were averaged between time steps 50-250.

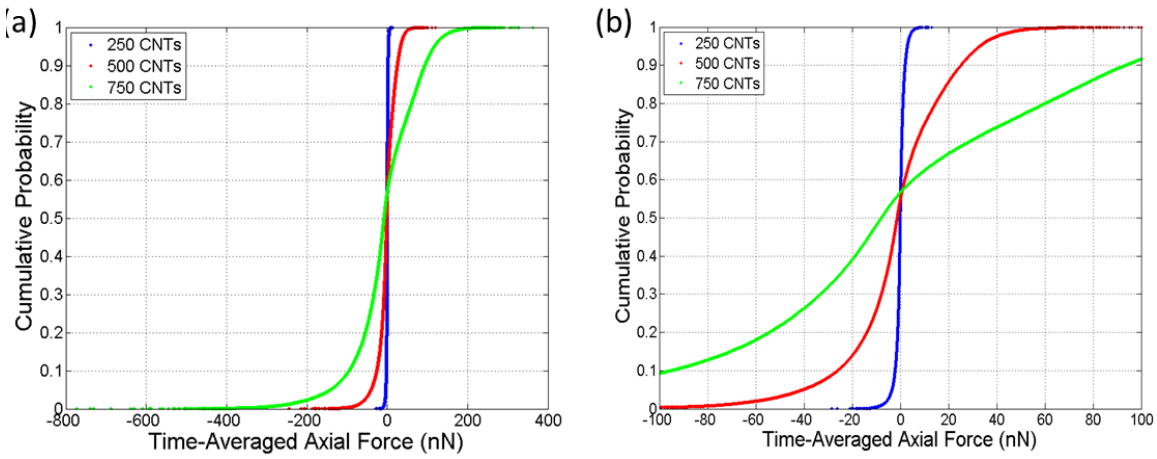

Figure 22. The cumulative probability of axial forces generated for forests consisting of 250, 500 and 750 CNTs forests residing on a 50 μm substrate shown for (a) the entire distribution, and (b) between -100 nN to 100 nN [105].

The magnitude of force increased significantly with increased CNT density. The increase is related to an increased frequency of CNT-CNT interactions. Because the force generated by CNT-CNT interactions decays with time after the establishment of new CNT-CNT contact (see **Figure 13**), an increased frequency of CNT interaction leads to increased average force. We found that the average force scaled approximately with the third power of number density. A reduced-area plot of **Figure 22a** is shown in **Figure 22b**. This plot demonstrates that the time averaged force axial force distribution is not symmetric, and that approximately 55-57% of CNTs are in compression, while the remainder are in tension.

2.3.9 CNT forest edge effect

Whereas CNTs in the interior of a forest incur CNT-CNT interactions from all directions, CNTs at the edges of the simulation domain may only interact with CNTs from within the interior of the forest. To investigate how this edge effect relates to the magnitude of forces transmitted to the catalyst particles, CNT densities of 250, 500, 750 CNTs over a 50 μm substrate were simulated. Time-averaged force magnitudes were recorded over 100 simulations for each configuration and were normalized based on the maximum load magnitude for each configuration. As seen in **Figure 23**, the magnitude of force at the edges of the simulation are significantly less than those experienced within the interior. The transition between the edge and interior occurs over a span of 1-2 μm, indicating that a limited "skin-effect" is present in which exterior CNTs experience reduced loading.

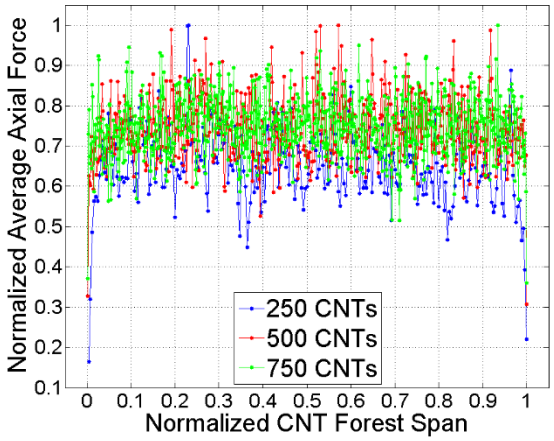

Figure 23. Normalized magnitude of time-averaged axial force vs. normalized span for CNT forests consisting of 250, 500, and 750 CNTs within a 50 μm simulation domain. The results are based on 100 simulations for each CNT density [105].

2.3.10 Force-modulated growth rates

The time-varying forces transmitted to CNT catalyst nanoparticles is expected to modulate the growth rate, and perhaps quality, of CNTs within a growing forest. The role of a catalyst particle is to selectively facilitate a specific reaction pathway. Often chemical reactants are adsorbed to the surface of the catalyst particle, during which time chemical interactions between reactants and the catalyst particle act to alter the energy level of adsorbed species [118-121]. Mechanical strain modulates the interatomic displacement in a catalyst particle, thereby altering the chemical pathway of the catalytic interactions in a process known as mechanochemistry. Kinetically, mechanical strain manifests as a modification to the activation energy of a given process. Han *et. al*. pointed out that a mechanical coupling between growing CNTs transmits forces that can create an energy barrier that ultimately exceeds energy available from chemical reaction at underlying catalyst particles [122], stunting CNT growth. Another recent report showed that CNT forests growing under a compressive mechanical decreased the observed CNT population growth rate [107]. These studies suggest that mechanical stress acting on catalyst nanoparticles alter the activation energy of CNT growth. In these studies, the collective CNT forest grew at a decreased rate with Arrhenius-like dependence [107]:

$$\text{Growth Rate} = Ae^{-(E_a-\Delta E_a)/kT} \quad (7)$$

where A is a constant derived when no force is applied to the substrate, E_a is the effective activation energy of CNT growth under no mechanical load which is assumed to be constant for our simulations, k is the

Boltzmann constant, and T is temperature. The ΔE_a represents a change in the activation energy resulting from mechanical energy acting on the catalyst in which tensile force is positive in sign, and compressive force is negative. The change in activation energy is linearly related to real-time applied force per CNT by a constant, α.

$$\Delta E_a = \alpha F \tag{8}$$

A constant value of α = 0.15 nm was found to match population-based data. Note that Eq. (8) does not account for variable CNT diameter, although the change in activation energy would likely vary as a function of strain energy, which is area-dependent. The effective activation energy for CNT growth in thermal CVD processes is in the range of 1.02−2.0 eV [84, 123-125]. ΔEa was calculated for each CNT in every time step to account for real-time forces exerted on catalyst particles. A stress-induced energy change of 0.02−0.16 eV was measured based on a compressive force application ranging from 10 pN to 1nN per CNT [107]. The study was conducted on CNT forests having diameters ranging from 6-10 nm and an areal density range of 7×10^8 to 2×10^{10} CNTs/cm^2. Because the external load was applied to the entire CNT forest population, it is unclear how the loading condition of individual CNTs within the forest were affected.

This mechanochemical coupling was incorporated into the finite element model based on these experimental findings. An activation energy of 1.5 eV was selected for all simulations. If the relationship provided by Eq. (8) is to be enforced with a value of α = 0.15 nm, then the stability of the simulation can only be ensured by real-time CNT forces on the order of 1 nN or less. To accommodate this limited force range, CNT forests having a homogenous outer diameter of 1 nm were selected for simulation. Furthermore, Eq. (7) was strictly enforced with both compressive and tensile forces. As a result, compressive forces decreased the growth rate of CNTs, while tensile forces increased the growth rate of CNTs. Two CNT forests were simulated up to 250 time steps employing a constant outer diameter of 1 nm to explore the effect of force-modulated growth rates during active growth. One simulation utilized force-independent CNT growth rates, while the other simulation used force-modulated growth rates based on Eq. (7-8). The simulations were otherwise identical.

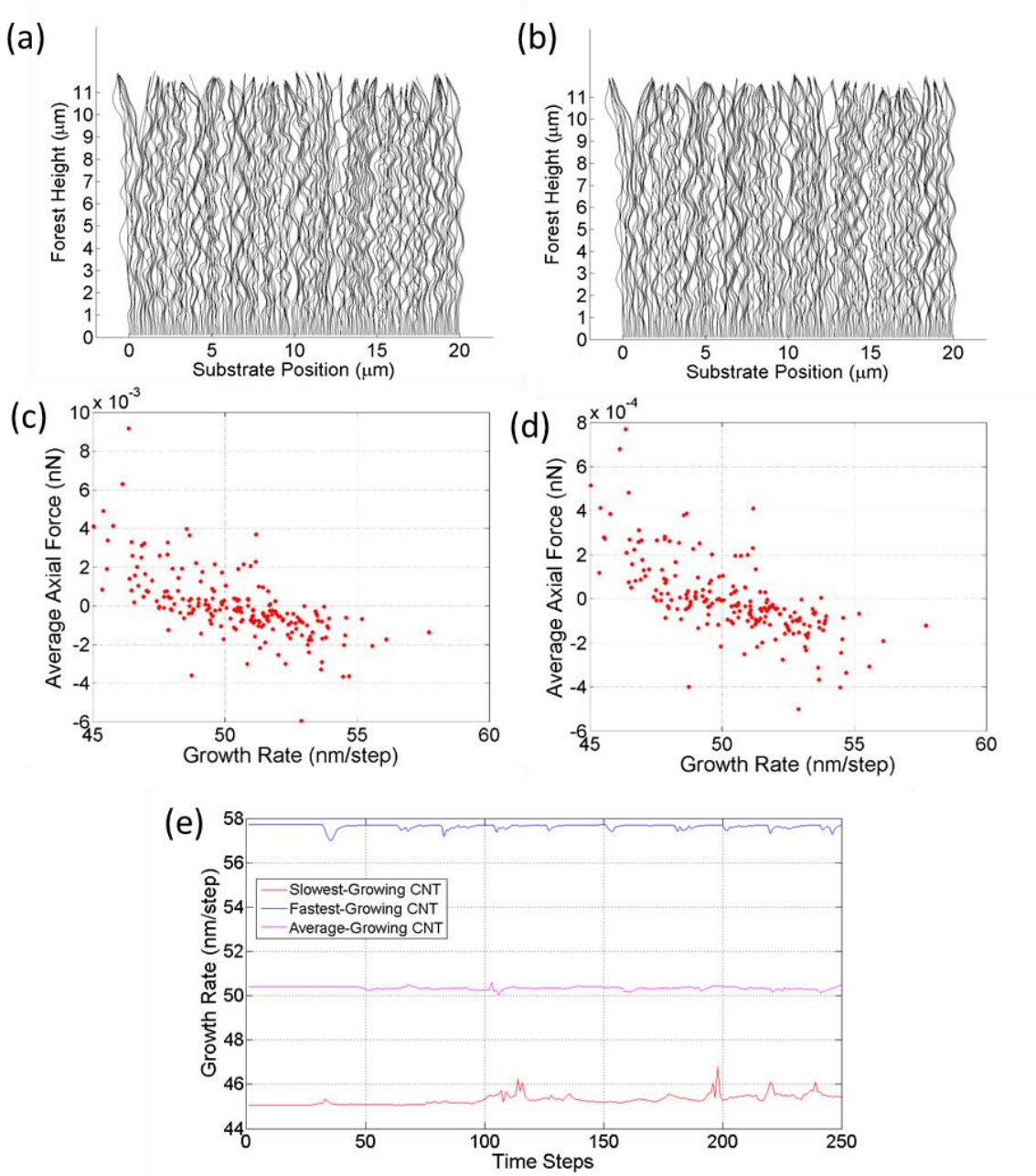

Figure 24. A comparison of CNT forest morphology grown using (a) constant and (b) force-modulated growth rates. The time-averaged axial forces transmitted to the base of CNT forests for (c) force-independent growth rates and (d) force-modulated growth rates indicate that a force-modulated kinetic model drastically decrease the magnitude of reaction forces generated within a growing CNT forest. (e) The time-resolved CNT growth rate based on force-modulated growth rates for the slowest-growing, fastest-growing, and population average CNTs indicate that the slow-growing CNT growth rate increased with tensile forces, while fast-growing CNT growth rate decreased with compressive forces. The simulations considered a CNT forest comprised of 1 nm outer diameter CNTs simulated for 250 time steps [105].

Figure 24 shows the CNT forest morphology and time-averaged axial force behavior using both force-independent and force-modulated growth rates. As displayed in **Figure 24a-b**, the CNT forests grown with and without force-modulated growth rates have a similar morphology. Because the change in activation

energy tends to decrease the growth rate of faster-growing CNTs (those in compression) and increase the growth rate of slower-growing CNTs (those in tension), the force modulation model tends to alter growth rates towards a population average growth rate and reduce the magnitude of forces generated within the forest. In fact, the time-averaged force transmitted to catalyst particles decreased by approximately one order of magnitude when force-modulated growth rates are considered, as shown in **Figure 24c-d**. To further illustrate the modulation of CNT growth rate with time, the CNTs having the slowest and fastest initial rate as well as a CNT having a population average initial growth rate of 50 nm/step, are plotted in **Figure 24e** as a function of simulation time. The forces generated by the CNT interactions are sufficient to vary the growth rate of CNTs by approximately 1 nm/step for the slowest and fastest growing CNTs. Note that the fastest-growing CNT decreases growth rate with interactions, and the slowest-growing CNT increases growth rate with interactions, as expected. By contrast, the CNT having the population-average initial growth rate experiences both increases and decreases in growth rate, as interactions are both tensile and compressive in nature. The self-modulating behavior of growth rate over time shown in **Figure 24e** is in agreement with findings from [122]. We note that the force-modulated growth rate model used here, represented by Eq. (7-8), was derived from the application of relatively small compressive force to the top surface of growing CNT forests, and further research is required to predict a more suitable mechanochemical kinetics model. Nevertheless, the force-modulation of CNT growth rate is shown to greatly impact the forces generated during the CNT forest growth assembly process and may present an opportunity for enhanced control of CNT forest properties.

2.3.11 The Mechanical behavior of single and multiple-generation CNT forests

In an experimental study [113], three-dimensional carbon nanotube (CNT) forest microstructures are synthesized using sequenced, site-specific synthesis techniques. Thin film layers of Al_2O_3 and Al_2O_3/Fe are patterned to support film-catalyst and floating-catalyst chemical vapor deposition (CVD) in specific areas. Sequenced application of the two CVD methods produced heterogeneous 3D CNT forest microstructures, including regions of only film-catalyst CNTs, only floating-catalyst CNTs, and vertically stacked layers of each. We believe that similar structures may be beneficial for electronic switches, tactile sensors, prescribed energy absorption surfaces, and as scaffolds for complex 3D microstructures. Here, the compressive

mechanical behavior of the heterogeneous CNT forests was evaluated, with the stacked layers exhibiting two distinct buckling plateaus.

The mechanical behavior of single and multiple-generation CNT forests was examined using the finite-element mechanical model. Each simulated CNT forest was first synthesized numerically using growth parameters consistent with experimentally obtained parameters, described in details in [113]. The simulation span for both CNT forests was 25 μm, with periodic boundary conditions in the horizontal direction. A total of 250 CNTs were simulated for film-catalyst CNT forests (100 nm CNT-CNT spacing), and 125 CNTs were simulated for floating-catalyst growth (200 nm CNT-CNT spacing). If extrapolated to 3D, the CNT-CNT spacing correspond to an areal density of 1.0×10^{10} CNT/cm^2 for film-catalyst CNT forests and 2.5×10^{9} CNT/cm^2 for floating-catalyst CNT forests, comparable to the density of a typical CNT forest [82-84, 126-128]. The outer diameter was 10 nm for film-catalyst CNTs, and 40 nm for floating-catalyst CNTs. The inner diameter of all CNTs was 70% that of the outer diameter, consistent with experimental results shown in [113]. The population growth rate was based on a Gaussian population distribution with a mean of 60 nm per simulation step and a standard deviation of 5 nm/step. Each CNT forest was synthesized to a nominal height of 75 μm.

Following the simulated CNT forest syntheses, compressive loading was applied to the top surface of the forests [10]. The compressive displacement was applied at a constant rate of 30 nm per time step, while the synthesis substrate was treated as a fixed rigid boundary. Periodic boundary conditions were applied to the horizontal boundaries at 0 and 25 μm. The vertical reaction force contributed by each CNT contacting the compression surface was summed to obtain the cumulative compressive force. The force applied to the top surface was identical to the force transmitted to the growth surface.

When compressed in isolation, both the film-catalyst and the floating-catalyst CNT forest exhibited force-displacement characteristics of foam materials, similar to the nanoindentation data shown in [113]. The initiation of the extended force plateau for each forest corresponds to the onset of coordinated buckling. The coordinated buckling initiated at the top compression surface and propagated downward towards the growth substrate until cellular densification occurred, denoted by a marked increase in load. The buckling load was approximately 3.8 μN for the film-catalyst CNT forest and 35 μN for the floating-catalyst forest. We note that the buckling load of a CNT scales approximately with its moment of inertia

$$I = \frac{\pi}{4}(r_o^4 - r_i^4) \tag{9}$$

where I represents the area moment of inertia, r_o is the outer radius, and r_i is the inner radius of the CNT. Therefore, even though the floating-catalyst forest has lower CNT areal density, its resultant buckling load is significantly greater than that of the film-catalyst forest. The corresponding buckling engineering strain, defined as the compressive displacement divided by the forest height, is between 3-5% for both forests, consistent with nanoindentation data.

To simulate a double-layer CNT forest, the film-catalyst forest was placed atop the floating-catalyst forest. Interactions between the two forests at the interface were governed by van der Waals forces, modelled as linear elastic potentials. Compression was applied to the top surface of the film-catalyst forest at a rate of 30 nm / step. In response, the top-most film-catalyst forest buckled in a manner similar to its buckling in isolation. The resulting buckling load was approximately 3.8 μN (**Figure 25a**), similar to that obtained when compressed in isolation (see **Figure 26**). Buckling of the top CNT forest layer progressed from the top to the bottom of the layer. The floating-catalyst layer exhibited significant deformation only after the densification front reached the interface between the CNT forest layers. As the bottom CNT forest layer buckled, a second buckling plateau profile was observed as a reduced slope in the loading curve. The second plateau is observed as a localized decrease in the loading stiffness profile (**Figure 25b**), obtained by dividing the incremental load by the incremental displacement step. Much like the experimental data, the buckling force plateau of the bottom layer is superimposed upon the densification of the top CNT forest layer. Significant compression of the bottom CNT forest layer occurred at the onset of densification of the top CNT layer. A deformation sequence is displayed in **Figure 25c**.

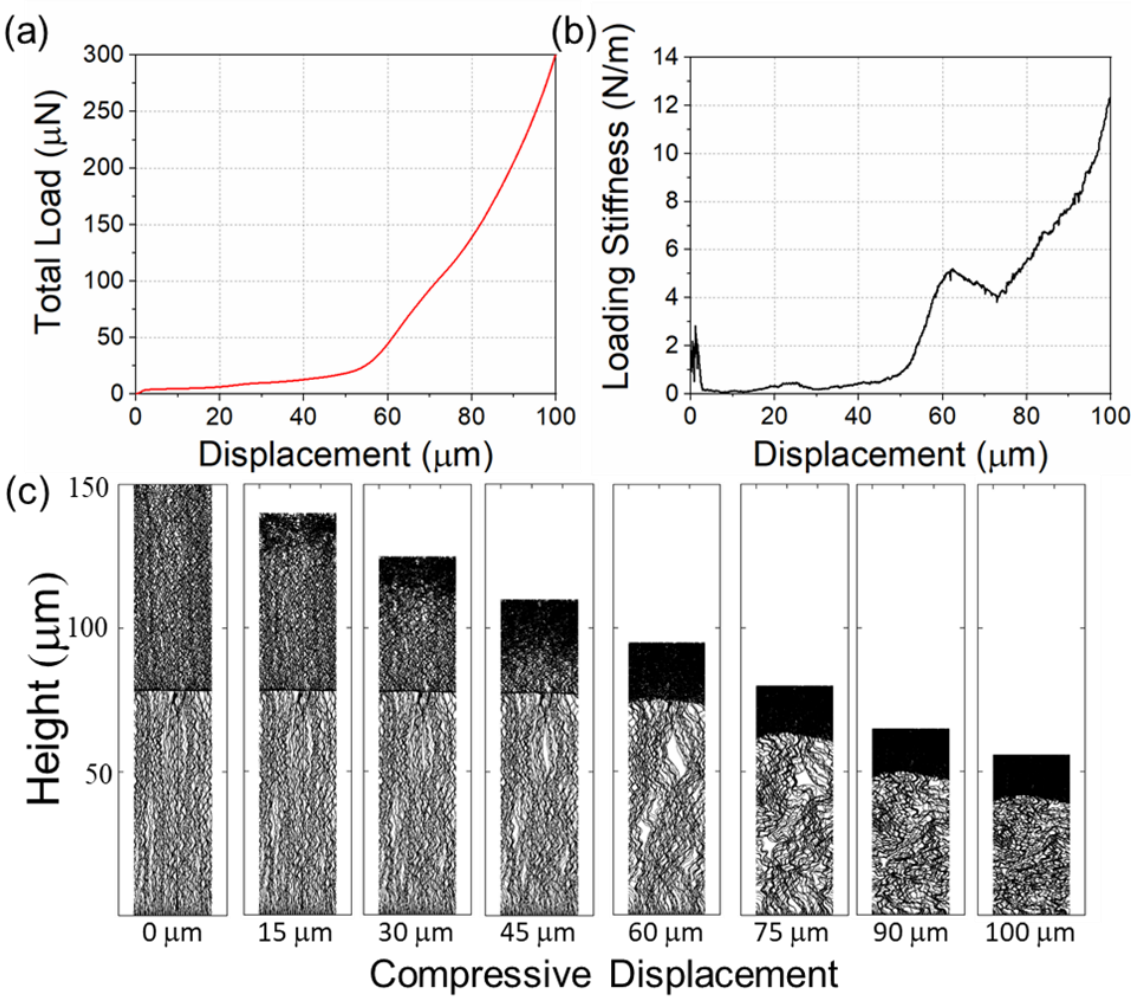

Figure 25. The simulated compression of double-layer CNT forest. (a) The total load vs. displacement and (b) incremental load vs. displacement showing the increase in load per 30 nm compression increment. Note that the plots demonstrate an extended plateau from approximately 5 – 40 μm, followed by a rapidly increasing load, a slowly decreasing load slope between 50 – 75 μm, and an increased loading slope. (c) The CNT forest morphology during compression shows that the top (film-catalyst) forest buckles and densifies prior to the large-scale deformation of the bottom (floating-catalyst) CNT forest [113].

The loading profile of the stacked CNT forests is expected to behave similarly to two non-linear springs connected in series, whereby each CNT forest layer acts as a spring element. The spring element with the lowest stiffness will exhibit the greatest deformation at low loads, as demonstrated by the buckling of the top-most film-catalyst CNT forest. Note that the deformation of the bottom-most layer is small, but non-zero, as load from the top CNT forest layer is transmitted to the bottom layer. Because the critical buckling load of the top CNT forest layer is significantly less than the bottom layer, the top layer progresses though significant deformation and buckling with little deformation observed in the bottom layer.

The fixed-catalyst and floating-catalyst CNT forest layers used to construct the composite CNT forest layers were compressed in isolation. The load vs. displacement plots are shown in **Figure 26**. Note that the buckling load for the film catalyst is approximately 3.8 μN, similar to the initial buckling load observed in the double-layer CNT forest shown in **Figure 25**. The buckling load of the floating-catalyst CNT forest in isolation was approximately 75μN, compared to approximately 50 μN for the second plateau of the double-layer CNT forest (**Figure 25**). We note that the isolated fixed-catalyst CNT forest was compressed by a horizontal compression front moving strictly in the vertical direction. The interface between layers in the double-layer CNT forest was non-uniform in geometry, and the transmitted load was not strictly uniaxial.

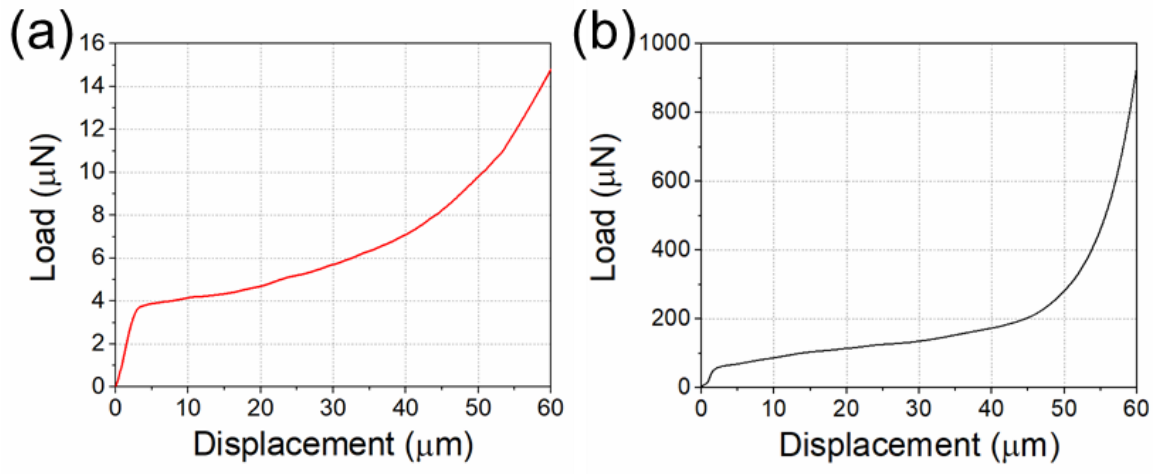

Figure 26. The simulated load-displacement curve for (a) fixed-catalyst and (b) floating-catalyst CNT forests. Note that these forests were the exact forests that were stacked to form the double-layer forest, whose response is shown in **Figure 25** [113].

2.3.12 Delamination Mechanics of Carbon Nanotube Micropillars

To better understand how the non-uniform load sharing and complex CNT forest morphology influence the experimentally measured delamination force of a CNT forest pillar, the finite element mechanical simulation was employed. Briefly, nominally 100 μm tall CNT forests were synthesized in silico using the 2D finite element simulation. The simulation span was 30 μm, to replicate the width of a representative

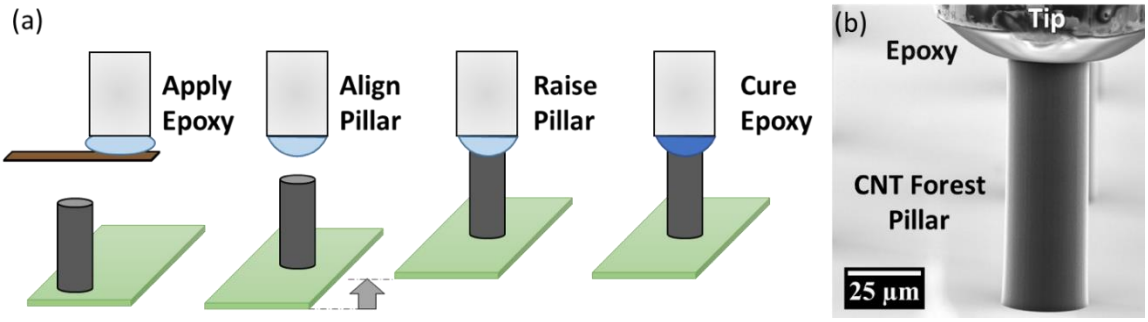

Figure 27. Adhesion of a CNT forest micropillar to an epoxy-coated test tip. (a) Schematic of epoxy application, pillar alignment, pillar insertion into epoxy, and epoxy curing. (b) SEM image showing the application of epoxy to the top surface of a cylindrical CNT forest micropillar [112].

CNT forest pillar shown in **Figure 27**. A total of 670 CNTs were contained within the simulation domain, corresponding to an average CNT-CNT spacing of 44.8 nm (5×10^{10} CNT/cm^2). The outer diameters of the CNTs were assigned based on a log-normal cumulative density function in which the mode was 10 nm. A plot of the log-normal probability density function may be found in **Figure 28**. The simulated growth of CNT forests assumed a Gaussian population growth rate distribution characterized by a mean of 60 nm/step and a standard deviation of 3 nm/step. A total of 1500 simulated growth steps were employed to achieve a CNT forest height on the order of 100 µm.

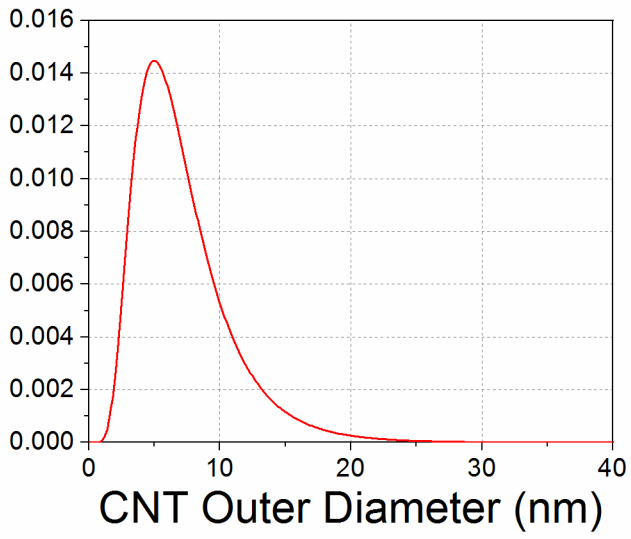

Figure 28. The log-normal CNT diameter distribution used for analysis and simulation [112].

After the simulated CNT synthesis, tensile loading was applied to the top surface of the simulated forest. To replicate the encapsulation of the top surface in a rigid epoxy, all CNT nodes within 2 μm of the top surface were assumed to be rigidly affixed to a surface that translated vertically at 1-2 nm per time step. The cumulative load was computed at each time step by summing the vertical component of force acting on each node within the simulated epoxy. Each CNT node residing at the growth substrate was assigned an identical adhesion strength, with separate simulations considering strengths of 200, 300, and 400 MPa. If the stress at the interface exceeded the adhesion strength, the CNT was removed from the substrate.

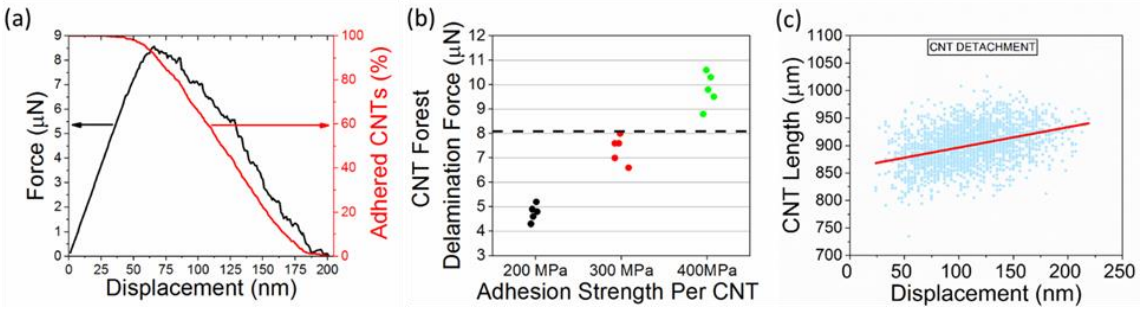

Figure 29. (a) The tensile load and percentage of adhered CNTs as a function of vertical displacement. (b) The simulated CNT forest delamination force for 5 representative CNT forests versus CNT adhesion strength. An average delamination force 12.2 nN per CNT was observed experimentally, corresponding to a delamination force of 8.17 μN in the simulations (with 670 CNTs), denoted by the dashed horizontal line. (c) The length of each delaminated CNT was plotted as a function of the tensile displacement at which the CNT detached. A linear trend line indicates that shorter CNTs delaminate at early stages of delamination. All simulations used a CNT-CNT spacing of 44.8 nm, corresponding to a CNT density of 5 x 10^{10} CNT/cm^2 [112].

A representative curve of the simulated tensile force vs displacement is shown in **Figure 29a** for a CNT forest having a substrate adhesion strength of 400 MPa. The loading slope initially increases linearly with displacement before reaching a maximum and rapidly decreasing. The decrease in slope can be directly correlated to a decrease in the number of adhered CNTs, also shown in **Figure 29a**. The peak load of approximately 8.7 μN, denoted as the CNT forest delamination force, is achieved at approximately 65 nm displacement, followed by a decrease in force and quantity of adhered CNTs. The CNT forest completely delaminated at 200 nm displacement, denoted by both zero force and zero adhered CNTs.

Simulations were conducted using 5 distinct CNT forests grown from different simulations. The delamination simulations examined uniform CNT adhesion strengths of 200, 300, and 400 MPa, with resulting CNT forest delamination forces shown in **Figure 29b**. Note that horizontal line at 8.17 μN in **Figure 29b** represents the experimentally-obtained average delamination force of 12.2 nN/CNT. Based on

simulations, the experimental CNT delamination force corresponds with a CNT adhesion strength of approximately 350 MPa (**Figure 29b**). This CNT adhesion strength exceeds the Monte Carlo-based estimation of 269 MPa, likely because the finite element simulation explicitly considers non-uniform load distribution and progressive loss of CNT adhesion. Note that the adhesion strength is significantly less than the yield strength of multi-walled CNTs (11 – 63 GPa) indicating that CNTs observed on the catalyst pad after delamination experiments were likely short CNTs rather than fractured CNT segments.

The tensile displacement at which each CNT delaminated was examined relative to the individual CNT length and cross-sectional area. Because each CNT was assigned an identical adhesion strength, it may be anticipated that small-diameter CNTs would experience higher strain, and thus lose adhesion first. Surprisingly, no correlation between delamination initiation and CNT diameter was found. Rather, a positive trend between CNT length and the delamination was found. A plot of CNT delamination as a function of CNT length and tensile displacement is shown in **Figure 29c**. The linear trend line shows that CNT delamination progresses from the shortest to longest CNTs within the population. The shortest CNTs in the forest are typically vertically oriented, with little excess waviness to accommodate tensile loading. Longer CNTs can accommodate tensile strain by straightening, whereas shorter CNTs cannot and the load is directly transmitted to the substrate. These results indicate that short CNTs disproportionately carry tensile force to the substrate during initial displacement and serve as initiation sites for delamination. The trend of relatively straight CNTs delaminating before wavy CNTs may be seen qualitatively in **Figure 30**.

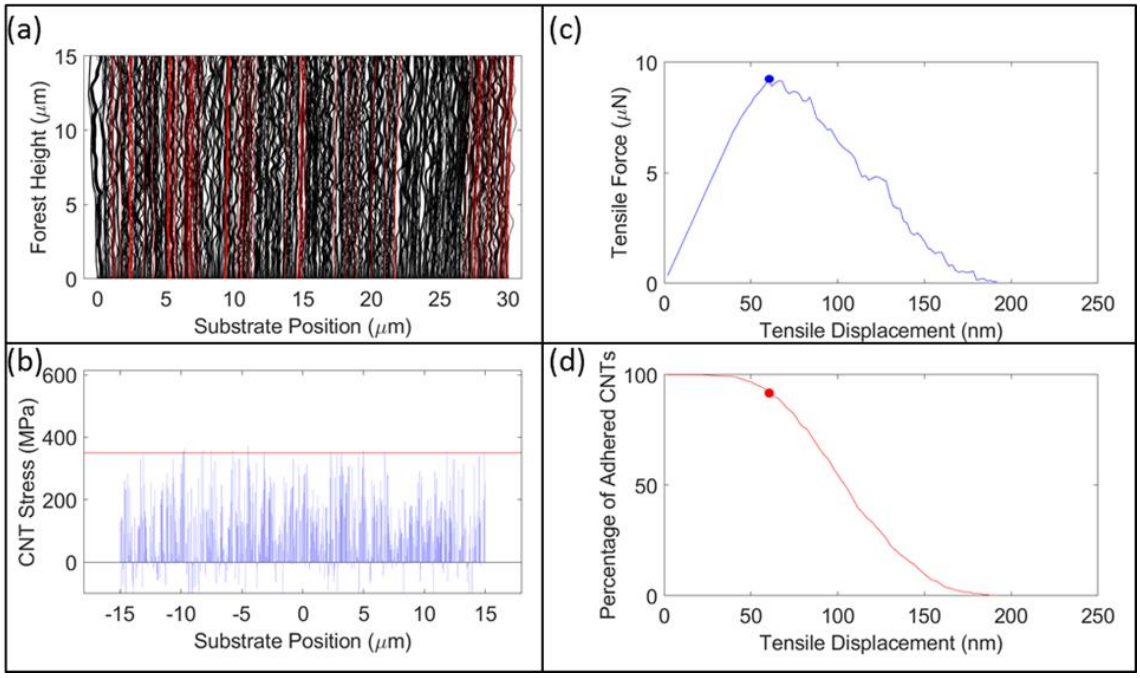

Figure 30. Simulated delamination of CNT forest (670 CNTs on 30 μm substrate) shown at maximum tensile load (60 nm). (a) CNT morphology, with black CNTs depicting adhered CNTs and red CNTs depicting delaminated CNTs. (b) Bar chart of CNT stress per CNT. The horizontal red line depicts the CNT adhesion strength of 350 MPa. (c) Tensile force vs. tensile displacement. (d) Percentage of adhered CNTs vs. tensile displacement [112].

The stress distribution at the base of the CNT forest was highly non-uniform throughout the tensile loading because of natural variations in CNT tortuosity, length, and diameter. A representative progression of CNT morphology and interfacial stress generated by each CNT during a delamination simulation is shown in **Figure 30a-b**. The CNT adhesion strength was 350 MPa in the simulation depicted in the figure, indicated by a horizontal line in the bottom panel of each image panel. CNTs with tensile stress that exceeded the adhesion strength were removed from the substrate in the subsequent time step. A fraction of the CNT population experienced a compressive (negative) stress at the substrate during the initial stages of tensile testing. These CNTs were generally wavy and were acted upon by constriction of neighboring CNTs via the Poisson effect. On average, the tensile stress increases with increasing tensile displacement. **Figure 30b** represents a tensile displacement of 64 nm, just past peak loading of 8.7 μN for this simulation. Note that delamination occurred within the center of the forest rather than at the edges (**Figure 30a**).

Initiation sites are stochastic in nature based on the morphology and parameter distributions within a given forest. By identifying the catalyst-substrate interface as the location of interfacial de-bonding for our catalyst and synthesis parameters, potential avenues to engineer interfacial adhesion strength may be

explored. Qualitatively, we suggest that methods to increase the bonding and interaction between catalyst particles and a substrate or buffer layer is a direct route for increasing the CNT forest delamination strength. Previous reports that utilized annealing steps [129, 130] to promote subsurface diffusion of catalyst particles appear to validate this suggestion. Further exploration of bond energies between catalyst particles and substrate materials using atomistic simulation may also identify new buffer layers to promote superior adhesion.

2.4 Conclusions

The time-resolved mechanical forces generated by the self-assembly of CNT forests were simulated with a finite element code, with an emphasis placed on the axial force transmitted to catalyst nanoparticles residing at the base of CNTs. We found that these axial forces were strongly correlated to CNT forest parameters including CNT diameter, areal density, and growth rate. CNTs with growth rates less than average growth rate experienced tensile loads while those with faster growth rates exerted compressive forces to catalyst particles residing on the substrate. Surprisingly, the existence of persistence van der Waals contact had little influence over CNT forest morphology when compared to van der Waals contacts that break at a tensile load exceeding 5 nN. The magnitude of forces scaled with the forth power of CNT outer diameter and the third power of areal density. Further, we found that CNTs at the physical boundary of CNT forests experience a reduction in force magnitude relative to CNTs located within the interior of a forest, as fewer CNTs are available to generate CNT-CNT reaction forces. Two distinct models were used to investigate CNT forests comprised of heterogeneous CNT diameters. One model considered a positive correlation between CNT diameter and growth rate, while the other assumed that growth rate and diameter were decoupled. Both methods produced similar CNT morphologies, and the time-averaged axial stresses between the two models followed a similar trend when plotted as a function of CNT growth rate. Finally, a mechanochemical kinetic coupling was introduced in which force transmitted to a catalyst particle altered its activation energy and subsequent CNT growth rate. The rate modulation decreased the magnitude of forces within the forest, as it decreased the growth rate of relatively fast growing CNTs and increased the growth rate of relatively slowly growing CNTs within the forest. Future studies may investigate the role of mechanochemistry in the abrupt termination of CNT forest growth. Understanding and controlling the forces generated during CNT forest

self-assembly could lead to application-specific CNT forest property sets to broaden the adoption of CNT forests in engineering applications.

Furthermore, the delamination simulations show that the entangled and wavy morphology of the CNT forests generated non-uniform load sharing. Consequently, the simulation suggests that the actual adhesion strength of individual CNTs to the growth substrate was approximately 350 MPa. These findings provide new insights into the magnitude of CNT-substrate adhesion, the non-uniformity of substrate loading during uniaxial delamination experiments, and identification of the catalyst-substrate interface as the site for CNT forest debonding. Increasing the strength of the catalyst-substrate interaction is expected to enhance the bonding of CNT forests for applications.

Finally, simulation confirms that the top CNT forest layer deforms and buckles in a manner similar to the layer in isolation. Deformation of the relatively stiff bottom layer is activated as the top layer begins to densify. In general, finite element simulation of the stacked layers demonstrated that the relatively soft film-catalyst CNT forests were nearly fully buckled prior to large-scale deformation of the bottom floating-catalyst CNT forests.

CHAPTER 3

IN-SITU GROWTH OF CARBON NANOTUBE FORESTS INSIDE ENVIRONMENTAL SCANNING ELECTRON MICROSCOPE (ESEM)

3.1 Introduction

It is clear that the pace of development of new materials has fallen far behind the speed at which product development is conducted. The lengthy time frame for materials to move from discovery to market is due in part to the continued reliance of materials research and development programs based on scientific intuition and trial and error experimentation. Much of the design and testing of materials is currently performed through time-consuming and repetitive experiment and characterization loops. Some of these experiments could potentially be performed virtually with powerful and accurate computational tools, but that level of accuracy in such simulations does not yet exist. Effective models of materials behavior can only be developed from accurate and extensive sets of data on materials properties. Experimental data is required to create models as well as to validate their key results. Where computations based on theoretical frameworks fall short, empirical testing will fill in the gaps. In order to study the nanoscale behavior of any advanced material including CNT forests at real time and high resolution, in situ synthesis and characterization techniques offer promising benefits. Determining the materials properties during processing will be paired with computational tools to enable rapid screening of materials, reactions, and processes over a wide range of length and time scales. Experimental outputs will additionally be used to provide model parameters, validate key predictions, and supplement and extend the range of validity and reliability of the models.

CNTs are grown inside an environmental scanning electron microscope (ESEM) on thermal E-chips to determine the relationships between diverse synthesis parameters and the resultant CNT forest morphology and ensemble property sets. The main novelty of this approach is that a growth furnace with the size of about

1 m^3 is converted into a chip of the size of a mobile sim card so that the CNT growth can be observed in real time using an SEM. The stage can be quickly heated/cooled at a ramp of 1000 °C/ms up to 1200 °C, powered by an external adapter. The experimental setup can simultaneously or separately investigate the thermal and electrical behavior of CNT forests. In addition to validate our simulation model and to better understand the synthesis and self-assembly of CNT forests, there is a high demand for image-based analysis of CNT forest synthesis at various stages of the growth and assembly process. For example, it is instructive to carry out image analysis after annealing to observe how thin film of catalysts are converted into nanoparticles. This imaging yields diameter and distribution of catalyst particles that is used to refine CNT forest growth simulation assumptions. Hence, the in-situ CNT synthesis experiments are developed to examine how my simulation model assumptions agree with experimental results by addressing fundamental characteristics of CNT nucleation, self-assembly, growth termination, and ensemble forest behavior.

These experiments can measure the CNT growth parameter distributions (diameter, growth rate, orientation, areal density, etc.) while observing evolving CNT-CNT interactions from initial CNT-CNT contact until growth termination employed. Also, it is intended to make a database of the SEM morphology images for training an active-learning deep neural network that predicts material properties of a CNT forest in real time. The data-driven prediction model and results are further explained in detail in the next chapter. Briefly, in-situ SEM growth of CNT forests will provide data that is inaccessible to other techniques and is essential for understanding the fundamental mechanisms of CNT forest kinetics and self-assembly. It is important to note that it is a novel approach to perform the in-situ SEM CNT synthesis that represents a new capability for in-situ nanomaterial synthesis. In addition, in the future, it seems necessary to characterize CNT forests to obtain electrical, thermal and mechanical properties to complete the AI-driven model dataset; hence the same synthesized CNT forests will be subjected to in-situ SEM electro-mechanical compression to complete the synthesis-structure-property analysis. This setup can readily be used to study the chemical, thermal and structural behavior of any materials subject to heating and electrical testing at high vacuum or exposed to water vapor at low vacuum to characterize materials oxidation behavior. In-situ electron microscopy will significantly accelerate the pace of building fundamental understanding and developing new materials.

3.2 CNT Forest Synthesis on Thermal E-Chips

In this study, actively growing CNT forests will be directly observed and measured using in-situ scanning electron microscope (SEM) syntheses. This research focuses on obtaining time-resolved behavior of CNT forest self-assembly, growth, and termination using in-situ SEM synthesis. This capability has not previously been reported and will greatly expand the observation capability of in-situ nanomaterials synthesis. Accordingly, in-situ SEM observations are used as inputs to validate the finite element simulation tool already discussed in the previous chapter.

We will use our simulation model to understand CNT forest process-structure-property interactions to predict the synthesis parameters required to yield desired CNT forest properties with statistical certainty. Accomplishing this goal could unlock the full potential of CNTs originally envisioned shortly after their discovery and would propel industrial adoption of CNT-based technologies. The governing kinetics of individual CNTs will first be examined and then placed within the context of a large and interactive CNT population. Understanding and abating the sources of morphological variation will lead to unprecedented synthesis control and access to the full property range of CNT forests. Investigating, predicting, and ultimately controlling the ensemble CNT forest properties will be addressed using advanced in-situ SEM synthesis and dynamic numerical simulations techniques.

The in-situ experimentation is conducted at MU Electron Microscopy Core Facility (EMC) where FEI Quanta 600F Environmental Scanning Electron Microscopy (ESEM) equipped with Protochips Fusion Heating/Electrical Biasing Stage is transformed into an in-situ laboratory (see **Figure 31**). The proposed research plan is integrated across multiple length scales, and across experimental and numerical platforms. The experimental objectives, address fundamental characteristics of CNT nucleation, self-assembly, growth termination, and ensemble forest behavior. Addressing these objectives and hypotheses will be instructive towards the goal of understanding the process-structure-property relationships governing CNT forests.

SEM-based capability builds from in-situ TEM techniques and significantly expands the observational envelope of in-situ synthesis techniques from hundreds of nanometers to hundreds of microns. The synthesis platforms will use the Protochips Fusion E-chips (see **Figure 32**) designed specifically for high-temperature in-situ electron microcopy. In-situ experimental data will serve as input to a complementary simulation tool

used to model and predict CNT forest process-structure-property relationships and unite experimental findings.

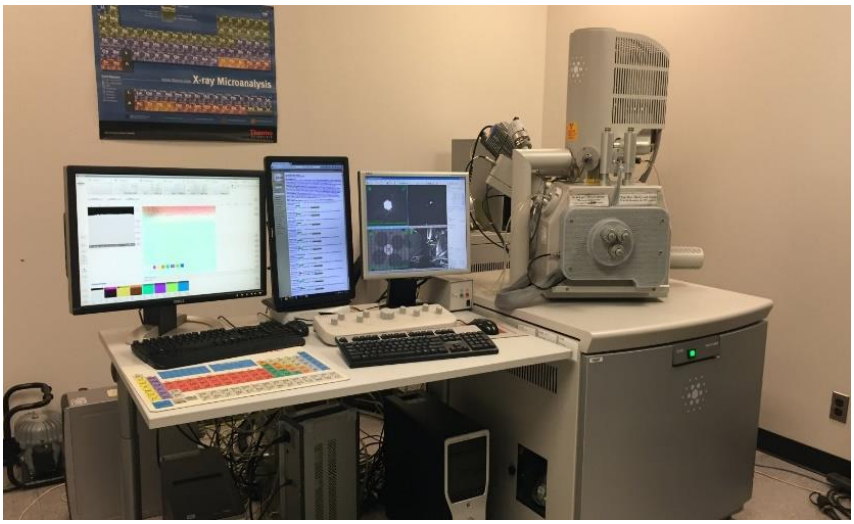

Figure 31. FEI Quanta 600F Environmental Scanning Electron Microscope (ESEM).

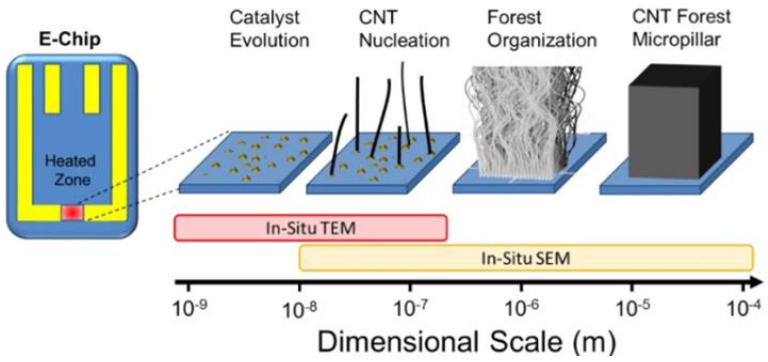

Figure 32. Schematic showing the in-situ synthesis experiments planned using the thermal E-Chip platform.

In-situ synthesis conditions for SEM will be varied about established TEM protocols for few-walled CNT forests, including a synthesis temperature of 600 ℃- 900 ℃, catalyst films of 10-30 nm Al_2O_3 and 1-3 nm Fe, and partial pressures of H_2 and C_2H_2 of 40 and 10 mTorr, respectively [98]. Variations in these conditions will be utilized to suit the needs of individual experiments. A 5 kV acceleration will be used for SEM imaging. The Quanta SEM provides a capture rate of up to 40 frames/sec.

At the onset of acetylene gas introduction, CNTs are expected to nucleate in a nonuniform and staggered manner with time. The latency time between the introduction of acetylene gas and CNT nucleation to initiate CNT forest growth may contribute to structural disorder, but the relationship between latency time and catalyst diameter due to variable diffusion lengths or diameter-dependent carbon saturation is unknown. Varying the annealing time, temperature, and gas environment will alter the particle size distribution to force variable catalyst distributions prior to growth. Upon nucleation, chemical kinetics suggests that the carbon diffusion rate (growth rate) of CNTs should increase with catalyst diameter due to increased particle surface area [87, 88]. As discussed in chapter 2, the mechanical properties of CNTs are also diameter-dependent, with bending stiffness $\propto D^4$ and tensile stiffness $\propto D^2$. These phenomena suggest that larger-diameter CNTs grow faster and have greater stiffness than smaller-diameter CNTs in a forest. Finally, time-staggered deactivation of catalyst particles due to amorphous carbon buildup (or 'poisoning') will lead to an accumulation of "dead" CNTs that may tether to actively growing CNTs, causing them to deform, and interrupting structural order. Chemical kinetics suggests that catalyst lifetime increases with diameter and catalyst surface area. Analysis of forests *after* synthesis cannot resolve these functional relationships, necessitating in-situ techniques. In-situ experiments facilitate observing dynamic interactions and fast reactions that results in obtaining new insights to achieve accelerated research discovery.

Based on outcomes of growth kinetics of individual CNTs, synthesis conditions can be set to encourage large growth rate variation within the CNT population to generate large reaction forces [10, 114]. Unfortunately, this objective is not achieved yet, but it exhibits a great potential towards understanding CNT kinetics. While TEM offers superior resolution to SEM and will readily capture internal CNT wall structure in response to strain, SEM-based synthesis offers a larger focal plane for readily viewing both CNT and catalyst response to loading. Thermal E-chips featuring through holes will be examined to facilitate cross sectional analysis of CNTs growing from the side walls of the holes. Growth rate, catalyst size, and catalyst motion may be measured using ImageJ. Based on observed CNT-CNT kinematics, finite element mechanical simulations will estimate the spatiotemporal force distributions between interacting CNTs using our finite element mechanical model. Here, experimental CNT deformation sequences will be converted into nodal points interconnected by discrete elements. Changes in nodal locations with time will be used to estimate forces based on assumed elastic properties. Deformation in the out of plane direction will be estimated as

best as possible. CNT delamination, buckling, kinking, and CNT-CNT bond breaking will be similarly simulated to estimate the critical forces and energies of these respective events. These parameters and behaviors will be integrated into our CNT forest synthesis-structure-property simulation such that these events may be reliably simulated.

3.3 Experimental Set-up Description and Steps

A Protochips Fusion Thermal E-Chips setup is used to grow CNT forests. The fusion stage can be used to manipulate and explore a wide variety of material properties. SEM can be used to simultaneously study the structure, processing, properties, and performance of material systems in real-time. Another capability is while characterizing the size, morphology, reactivity, and evolution of 1D, 2D, and 3D nanomaterials often only provides "snapshots" of the underlying process of interest, with in situ electron microscopy, one can directly observe nucleation and growth, oxidation/reduction reactions, morphology evolution, sample mobility, chemical gradients, and other dynamic changes in real-time. It can also be used to examine catalysis, electronic devices, and energy materials.

The main components of the experimental setup are shown in **Figure 33**. In this work, we have only used the thermal experiments while the setup has dual electrical and thermal characterization capabilities. Some important features of the fusion platform are:

- Transforms SEM or TEM into an in-situ laboratory
- MEMS-based E-chips with imbedded electrical leads and silicon carbide heaters
- Dual-channel thermal and electrical analysis capability
- Swift temperature changes up to 1200 °C (thermal ramp rate of 1000 °C per millisecond)
- Real time adjustment of thermal and electrical conditions
- Characterize samples using EBSD, EDS and Raman capabilities
- Open and closed loop temperature control options

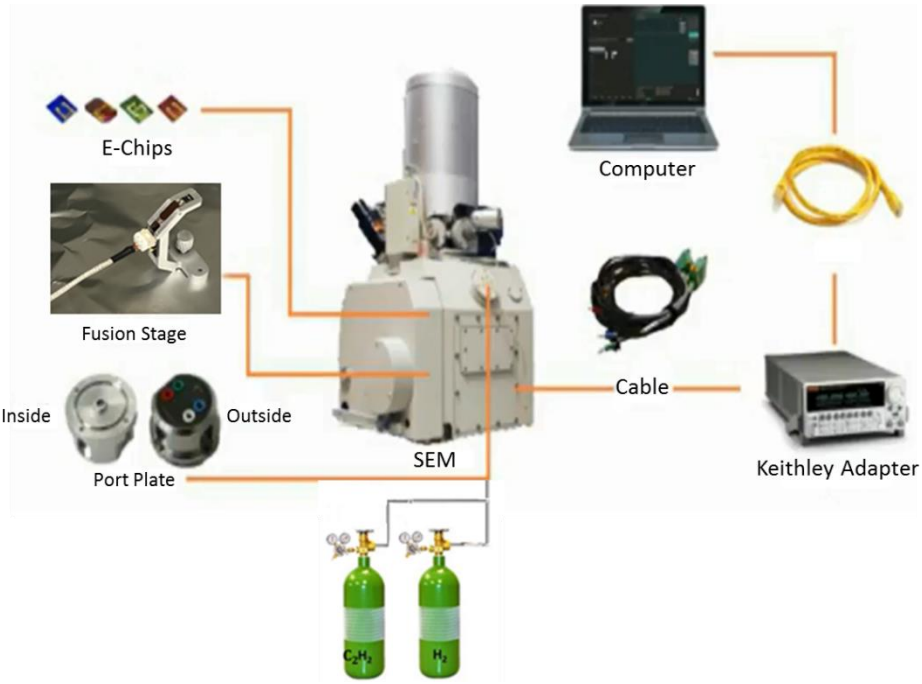

Figure 33. Schematic of a Protochips Fusion Thermal E-Chips setup connected to Scanning Electron Microscope (SEM) consisting of Laptop with Clarity workflow-driven software, Keithly power supply, fusion stage, E-chips, port plates installed on SEM, stainless steel gas piping line, and C_2H_2/H_2 cylinders.

As seen in **Figure 33**, gas cylinders (hydrogen and acetylene) are connected to bottom inlets of SEM (from behind) through a T-junction that mixes gases with user-defined mass flow rates before entering the chamber. Two port plates are installed permanently on both inside and outside of SEM that lets the fusion staged be connected to the Keithley power supply. When performing a new experiment, first a thin film of catalyst consisting of Fe and Al_2O_3 underlayer is deposited using ion beam sputtering system (South Bay Technologies). Then, the E-chip is placed on the fusion stage and later mounted inside the SEM. It should be noted that the stage should be connected to the inner port plate. The power supply should be also connected to the outer port plate to be able to provide necessary power to the stage for further heating experiments. An Ethernet cable connects the laptop to the Keithley, and an AMP dongle is connected to Keithley.

After launching the Clarify software, parameters for each specific E-chip should be set up. After selecting the intended type of experiment (electrical, thermal or both), a locally stored calibrated file (on a sperate CD provided for each E-chip gel pack) should be loaded. In this work, we only use environmental thermal experiments. There are two types of thermal configurations available for performing experiments, namely Vacuum and Environmental. In order to use the Environmental Heating Mode, a closed loop chip with a

closed loop calibration file has to be used. Once all chip setup is adjusted a “Device Check” has to be performed. The check will be passed when the E-chip has been loaded correctly and that the sample preparation will not affect the heating profile. A screenshot of software for device check is shown in **Figure 34a.** The heating/cooling mode should be selected that can be either manual or to follow a specific pattern like waveform. The manual mode of the Fusion software executes individual temperature changes to the heating membrane on a thermal E-chip. The target temperature and ramp rate should be also selected. It should be noted that in closed-loop control case, there is a limitation of 30 °C/s rate of change. Although, it is slower to get to the target temperature with closed-loop control, the prescribed temperature setpoint is assured, regardless of the operating pressure. Once the desired settings are appointed the stimuli can be started by clicking the Apply button. During the experiment a stimulus can be held at a certain level by pressing Hold. The experiment will be continued by pressing Resume at any time. The Stop button will end stimuli to the chip and the data logging of the experiment. The System Status informs you of the current state of a session. A screenshot of this step is depicted in **Figure 34b.**

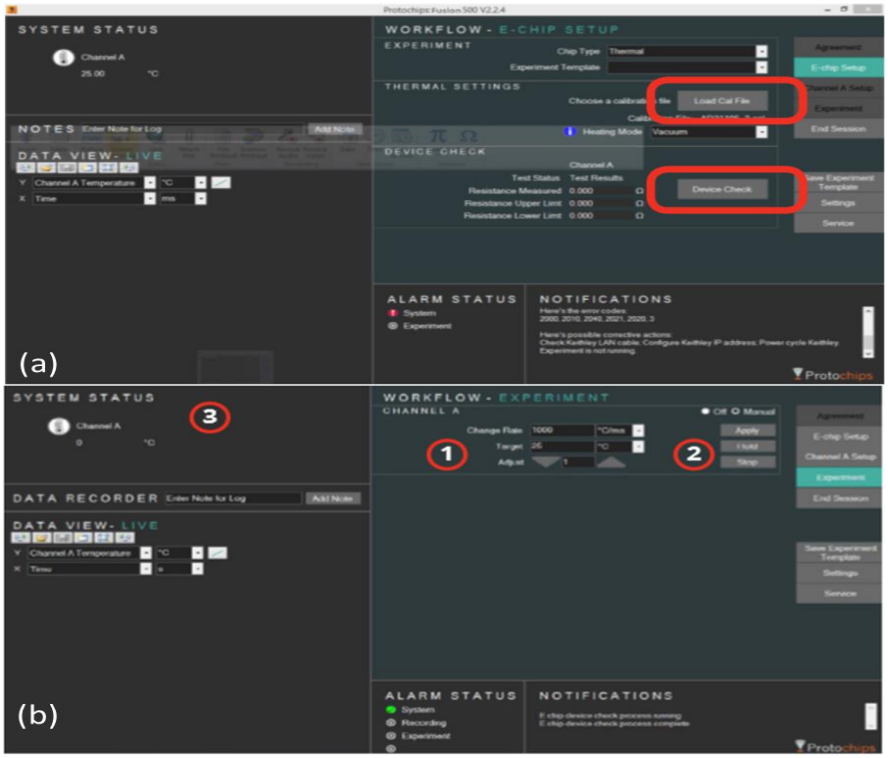

Figure 34. A screenshot of software (a) device check step where a calibration file is loaded and checked if E-chip passes the test for the selected experiment type (b) 1- setting experiment target temperature and rate change, 2- applying settings and 3- monitoring system status (temperature profile).

Although there are different types and shapes of E-chips, only thermal E-chips coated by SiN are used for our experiments. A schematic of thermal E-chip with the zoomed heated area and chip holder is shown in **Figure 35**.

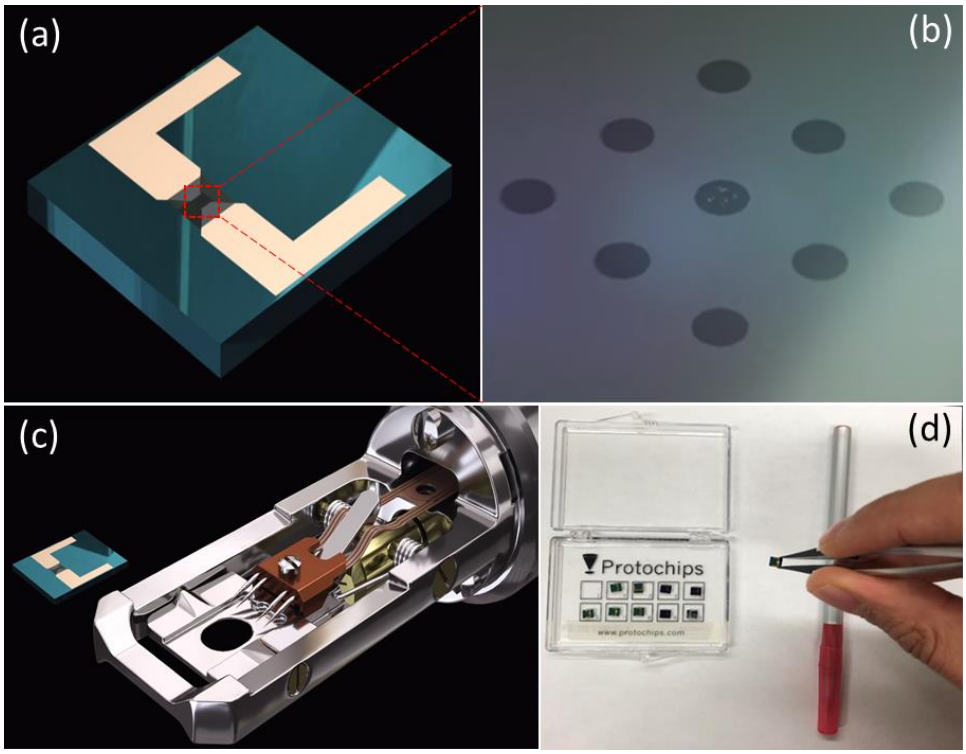

Figure 35. Fusion heating E-chips (a) isometric view showing gold contacts and the central heated area (150×150 μm) (b) zoomed view of heated area showing 9 holes (7 µm diameter) transparent to electron beam (c) a typical chip holder (d) a gel pack of thermal E-chips coated by SiN used for our experiments.

3.4 Result of Experiments

In-situ synthesis conditions for SEM include a synthesis temperature of 700-900 ℃, catalyst films of 10 nm Al_2O_3 and 1-2 nm Fe, and partial pressures of H_2 and C_2H_2 of 40 and 10-40 mTorr, respectively. Also, 5 kV acceleration will be used for SEM imaging. Catalyst film deposition is performed within a "South Bay Technologies" Ion Sputtering Machine. Catalyst film reduction into particles, i.e. annealing, is carried out at 700 ℃ for 5-10 minutes using only H_2, followed by introducing C_2H_2 to start growth for approximately 15 minutes.

We had several unsuccessful growths (see **Figure 36**) before the last two successful growth. In such experiments, the catalyst layer was converted to nanoparticles but no CNTs was nucleated. However, catalyst particles were evident on SEM images. We believe that the reason why we could not grow CNTs in the central heated area was due to the hyrdrophobic characteristics of SiN layer. Generally, nanoparticles in organic solvents such as carbon nanotubes will not readily disperse on the silicon nitride membrane surface. This idea is supported by the forest grown far from SiN layer in a circular pattern as shown in **Figure 37**. It is worth mentioning that for high resolution imaging at low vacuum and high magnifications, a pressure limiting aperture is employed.

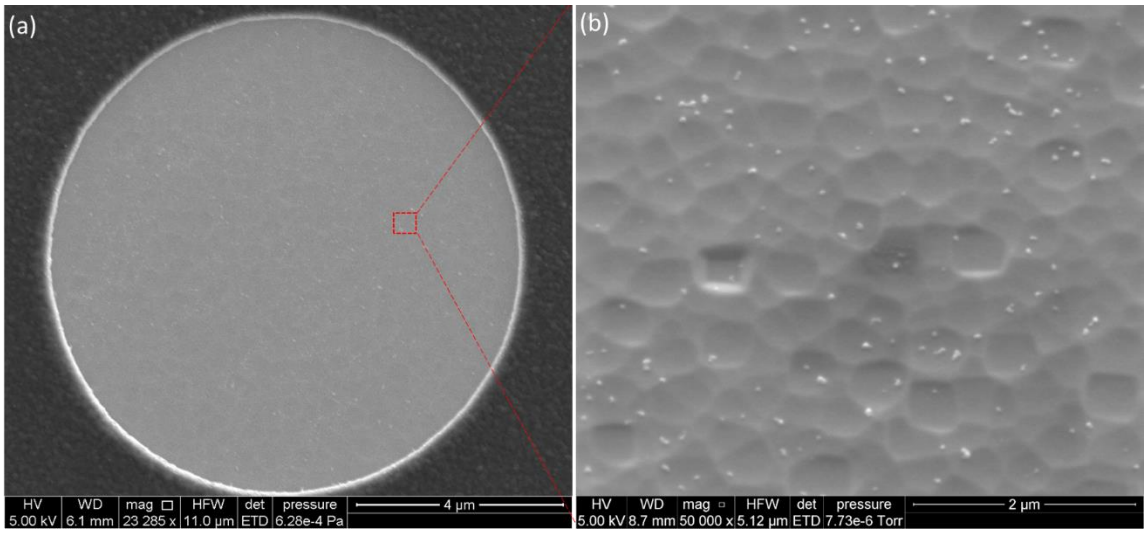

Figure 36. (a) SEM image of central hole of heated area after growth at high vacuum (white particles are Fe nanoparticles) (b) zoomed image of central hole of heated area after growth at high vacuum.

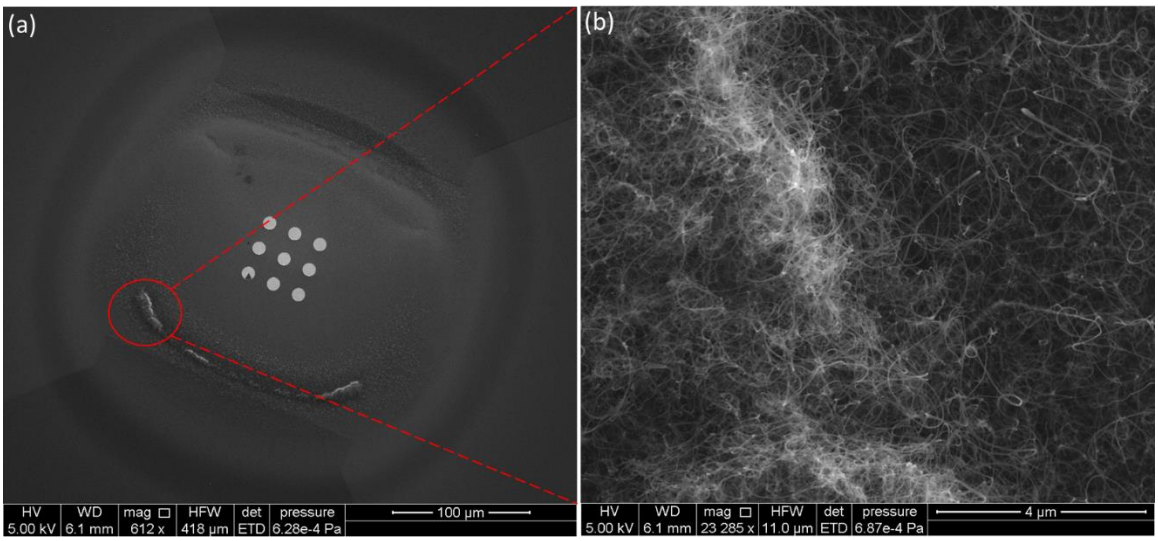

Figure 37. (a) SEM image of a dense CNT forests grown on SiN coated E-chips around the perimeter of heated zone (b) a zoomed SEM image of CNT forests (bottom left corner).

In another successful in-situ experiment, CNTs were synthesized mainly on top side of heated area as shown in **Figure 38**. This is another instance where catalyst particles migrate from the central heated zone. To passivate the SiN surface and combat the particle migration, E-chips were plasma treated for 2-3 minutes at MU EMC using Pelco Easiglow glow discharge cleaning system.

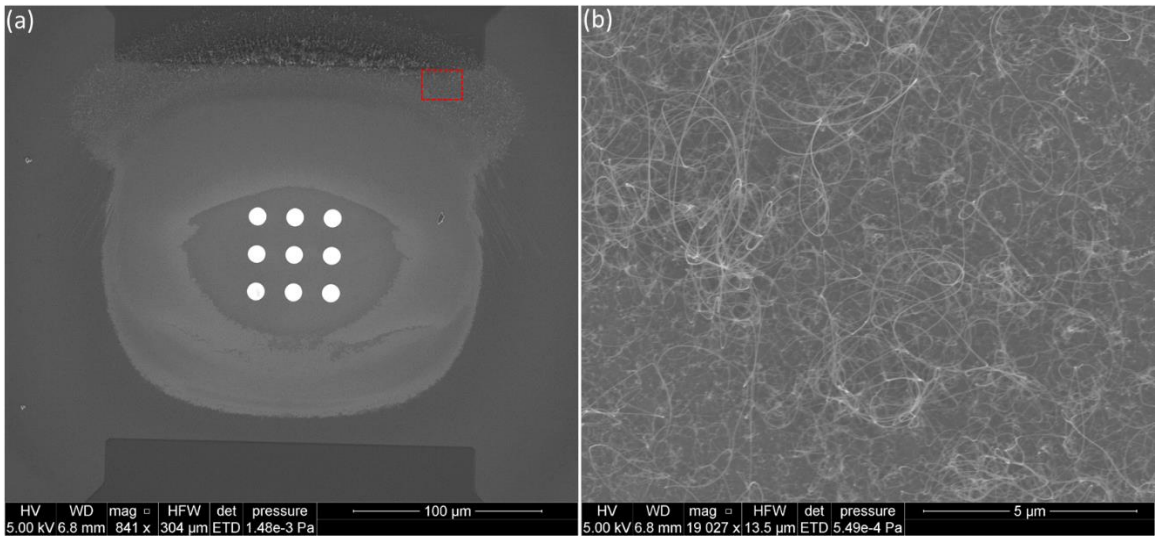

Figure 38. SEM image of (a) successful CNT forest growth on top of heated area (b) represent regions examined in higher magnification in (a).

A glow discharge treatment (see **Figure 39a**) with air will make the film surface negatively charged which stables nanoparticles. The Easiglow temporarily alters the charge on a carbon film – this charge can be

selected by altering the composition of the gas molecules in the chamber of the unit. This could stabilize the iron catalyst layer and prevent migration around heated area but did not end in any growth or only resulted in sparse growth. It is worth noting that the optimized vacuum level for glow discharge procedures is in the range of 0.45 to 1.1 mbar.

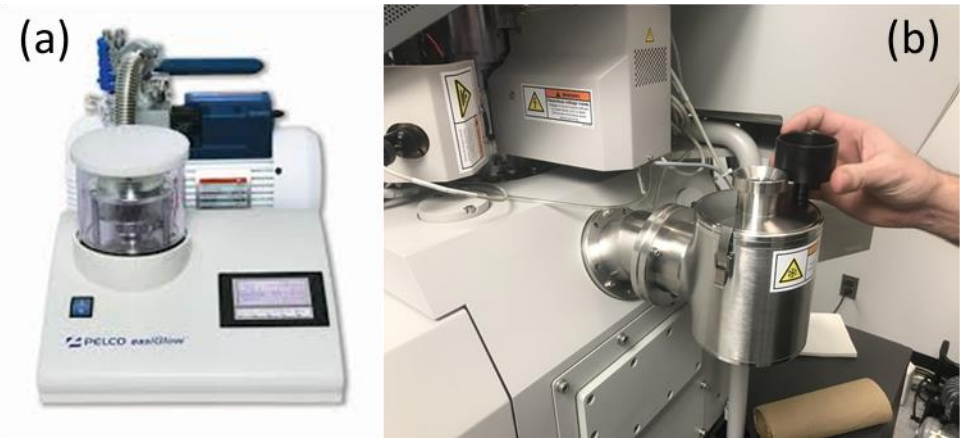

Figure 39. (a) Pelco Easiglow glow discharge cleaning system used for plasma treating SiN E-chips (b) cold trap cooled with liquid nitrogen installed on ESEM to remove contaminants and reduce chamber pressure

It was determined that the chamber base pressure was not suitable to enable CNTs nucleation and synthesis. Other in-situ TEM synthesis of CNTs [98] report that the chamber base pressure should be $<10^{-7}$ Torr, while our SEM base pressure barely reached 10^{-6} Torr. Achieving such low chamber pressure is crucial to remove water vapor that is so harmful to CNT growth. Accordingly, many efforts were made to reduce the SEM base pressure, including pumping the chamber for a longer period of time, e.g. over 2-3 days or overnight. Unfortunately, this longer pumping time was not also helpful to achieve the appropriate pressure. Another solution sought was to use a cold trap that is cooled with liquid nitrogen as shown in **Figure 39b**. Unfortunately, we employed a shared Quanta ESEM at MU core facility where different types of experiments are performed that leaves various contaminants inside the chamber. A cold trap is a device that condenses vapors existing gases of SEM chamber (except the non-condensable gases) into a solid. Cold trap, however, not only decreases the chamber pressure quickly but also removes water vapor and other contaminants that are unfavored for CNT growth.

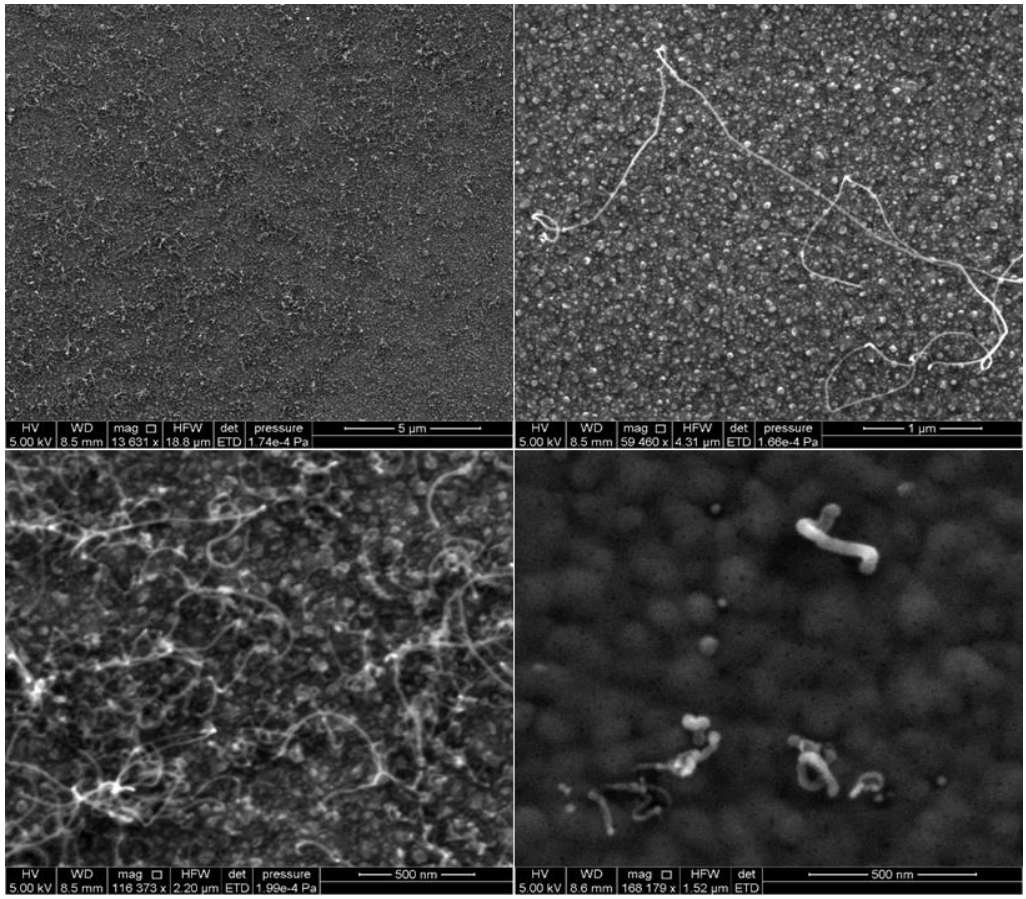

Figure 40. Some sparse growth of CNTs at different magnifications obtained from different CNT forest synthesis inside SEM

In addition, various catalyst thicknesses of 10-30 nm and 1-3 nm were examined systematically for alumina and iron, respectively. Also, different combination of hydrogen and acetylene mass flow rates were employed at different temperatures ranging from 650 °C to 900 °C. In **Figure 40**, some sparse CNTs are shown while implementing plasma treatment, cold trap and other modifications discussed earlier.

3.5 Conclusion

In situ experiments are conducted inside ESEM to grow CNT forests with the goal of observing forest synthesis and self-assembly in real time to investigate ensemble kinetics. The successful implementation of this method would represent a significant step towards using advanced experimentation to gain in-depth understanding of CNT growth and self-assembly to accelerate their adoption into industrial applications. This approach also will allow making an SEM image database that serves as input of a deep neural network

(discussed in more details in chapter 4) to predict CNT properties and design desired property sets. Although about 30 experiments have been conducted to grow CNTs inside ESEM, only a few experiments were successful. We believe that these difficulties are due to residual water vapor in the SEM. It is expected that conducting more experiments with a dedicated SEM will result in successful CNT forest growth. Unfortunately, the desired outcomes for the in-situ CNT growth experiments inside SEM were not reached, but many improvements were made to these experiments, including stabilizing catalyst nanoparticles in the heated area using plasma treatment, improving high vacuum pressure using cold trap, improving imaging resolution using a pressure limiting aperture, that leads to better imaging at higher pressures (at low vacuum mode). The successful growths are promising evidence that the ambitious goal of understanding CNT forest synthesis mechanics using in-situ SEM synthesis is achievable. Hence, I believe that the SEM experiments have the capabilities (spatial and time resolutions) required to be successful.

CHAPTER 4

EXPLORATION OF CARBON NANOTUBE FOREST PROCESS-STRUCTURE-PROPERTY RELATIONSHIPS USING PHYSICS-BASED SIMULATION AND DATA SCIENCE

4.1 Introduction

As already discussed in the previous chapters, carbon nanotubes (CNTs) are widely studied for their promising mechanical, electrical, and thermal properties [2] that make them suitable for diverse applications. However, a significant performance gap between individual CNTs and CNT forests is observed. To date, overcoming the performance gaps has not been achieved due to a lack of understanding about how the processing mechanisms of CNT synthesis control the CNT self-assembly process [9, 29, 100-104]. The wavy and entangled morphology of CNT forest caused by the mechanical competition of concurrently growing CNTs during self-assembly process is considered the main source of the performance degradation [82-86, 131]. An internal morphology of a relatively straight and a wavy CNT forest is shown in **Figure 7**. Deterministically achieving a desired property set from CNT forests is currently an unfulfilled challenge. Most CNT synthesis recipes rely on previously successful results rather than a fundamental understanding of CNT forest kinetics and the assembly process. The CNT forest processing parameter space includes numerous variables including catalyst composition, catalyst thickness, synthesis temperature, processing gas composition, synthesis time, operating pressure, among others. An experimental exploration of the full synthesis parameter space is both cost and time prohibitive. Numerical simulation of CNT forests synthesis and self-assembly is an alternative approach that may increase the speed and diversity of synthesis parameters examined. Such simulations can predict both the CNT forest structural morphology and the resulting CNT forest properties. By systematically varying CNT synthesis parameters, one may arrive at a set of conditions that product the desired CNT forest performance metrics such as mechanical stiffness and thermal conductivity.

These desired performance metrics are intricately related to the structural morphology of the CNT forest itself, although the functional relationships between CNT forest structural morphology and CNT forest properties are currently not well understood. The CNT forest morphology, in terms of CNT length, waviness, and density, may be tuned according to specific applications [132]. For instance, thin-film-type transistors require dense and parallel single-walled carbon nanotubes (SWCNTs) to sustain large current [133, 134], while their ultralong length enables easy fabrication of numerous devices out of one individual SWCNT and the construction of logic circuits at a single nanotube level [135, 136]. In addition, advanced and time-consuming post-synthesis material characterization techniques like nanoindentation should be applied to determine the ensemble properties such as mechanical (like stiffness, strength and buckling load), thermal and electrical conductivity, etc. Therefore, predicting the combination of processing parameters required to grow application-tailored CNT forests would represent a significant advance that could enable new CNT forest-based applications that fully exploit the beneficial properties of individual CNTs. Here we employ a physics-based numerical simulation of CNT forest growth and assembly to generate images of CNT forest morphology using variable synthesis parameters. Following CNT forest growth, a compression simulation was employed to obtain bucking load (the load necessary to bend CNT forests) and stiffness of CNT forests. The simulated imagery is used to train a ML model to predict the growth attributes of a CNT forest. Also, DL models were trained to predict forest properties based on their structures.

Machine learning is a powerful technique to identify patterns governing the behavior of nanomaterials synthesis to accelerate the search for optimal materials. Recent developments in the field of machine learning (ML) and Deep Learning (DL) combined with the current materials data infrastructure have made the data driven techniques popular and increasingly popular within the materials science community. Machine learning algorithms excel at finding patterns in a dataset and identifying qualitative trends and outliers that would otherwise be extremely difficult to find. Hence, ML exhibits a great potential in assisting materials design and synthesis in the future with the ambitious goal of accelerated and application-tailored materials design and discovery [137]. Recently, ML is successfully employed to design organic light-emitting diodes [138], metal-organic frameworks [139], classifying steel microstructures [140], construction materials [141-143], to accelerating post-disaster processes to mitigate natural disaster impacts [144-146] and in combination with computational materials to predict graphene bandgap [147]. A paradigm shift in the field

of material science is inevitable in the upcoming years as ML and DL becoming increasingly powerful to accelerate high-performance and low-cost material discovery. Unfortunately, the amount of available experimental data of CNT forest growth is not sufficient to be used as labeled data for training the machine learning model due to the vast range of CNT forest synthesis conditions, growth recipes and resultant morphologies reported in literature. Experimental results are usually noisy, expensive and time consuming, and the CNT forest attributes (CNT diameter, areal density, growth rate) are poorly characterized and time variant. Therefore, the physics-based simulation of CNT forests may present a reliable and powerful tool for training ML and DL models in the absence of suitable experimental data. When unseen patterns of material structures are determined by ML, the desired properties can be targeted tuning proper synthesis conditions. Material researchers hope that new material discovery and commercialization into various industrial applications become faster and more affordable by using closed-loop research systems [137]. AI-driven experimentation will be guided by autonomous systems that learn from the previous experiments and in real time to efficiently predict the next generation of experiments. This active learning model will best employ high-throughput modeling and simulation to improve quality and speed of future experiments [147-149]. This approach will hopefully help to commercialize CNTs into various industrial applications, an unfulfilled mission since CNTs were discovered in 1991 by Iijiama [1].

4.2 Exploration of Carbon Nanotube Forest Synthesis-Structure Relationships Using Physics-Based Simulation and Machine Learning (Hand-Crafted Descriptors)

In this study, the time-resolved mechanical simulation model is employed to nucleate and synthesize CNT forests. The finite element model is discussed in detail in chapter 2 and elsewhere [10, 105, 114]. Here, we have grown CNT forests with different user-defined synthesis inputs, namely CNT number density and CNT outer diameter to evaluate their effect on the forest structure. As there is a vast input parameter space that may result in different morphologies, investigating all process conditions is impractical. In this preliminary study, the resulting forest morphology is used to train a machine learning model to predict synthesis properties. Local feature extractors, individually and in combination, followed by random forest classifier were employed to create the class predictor model. We used four local descriptors that are derived from both

Local Binary Pattern (LBP) and Motif Cooccurrence Matrix (MCM) descriptors [150-152]. The descriptors are Rotation Invariance Cooccurrence among Local Binary Patterns (RICLBP), Joint Adaptive Median Binary Patterns (JAMBP), Joint Motif Labels (JML), and Motif Patterns (MP) encoded with RIC-LBP [152]. The reason behind using multiple local descriptors is to capture more texture features and to ultimately improve the final classification accuracy.

4.2.1 Methods

In this study, we classify twelve distinct CNT forest classes using different local descriptors to extract the texture features from the CNT forest images. In our proposed framework, the descriptors based on LBP [153] and Motif Peano scan methods [154] are used. The first two descriptors are called RIC-LBP and JAMBP which are a very powerful variation of the original LBP descriptor. The other descriptors are called JML and MP and are a modification of the original MCM descriptor. The reason we choose these set of local features is their ability to capture image texture and the high classification performance generated using challenging databases. In the following, we will explain how each method is used to extract features and the number of features used with respect to each descriptor.

A. LBP-Based Descriptors

1) RIC-LBP: The Rotation Invariant Co-occurrence among LBP (RIC-LBP) proposed by Nosaka et. al [155] was used successfully to classify Human Epithelial type-2 HEp-2 cell images. RIC-LBP makes use of the relationships among the binary patterns by finding the co-occurrence patterns among the histogram features as shown in **Figure 41a**. Moreover, RICLBP histogram is represented in the form of many LBP pairs, and each pair will be attached with a specific label to account for rotation invariance which makes it very powerful to capture important image texture. As proposed in [155], 408 bins from the three schemes were extracted.

2) JAMBP: The Joint Adaptive Median Binary Patterns (JAMBP) descriptor was introduced in [156] by Hafiane et. al. It builds upon the powerful AMBP [157] descriptor by joining more information extracted from the original image. This information represents the mean of the image and the window size used around each pixel to compute the threshold value. The power of AMBP descriptor is that it uses an adaptive window size around the center pixel as shown in **Figure 41b**. As a result, it has the ability to better capture texture features. Moreover, JAMBP uses multiscale scheme by computing AMBP descriptor using different ranges

and sampling points from the center pixel. In our work, we extracted 320 bins from JAMBP and used them in the classification phase.

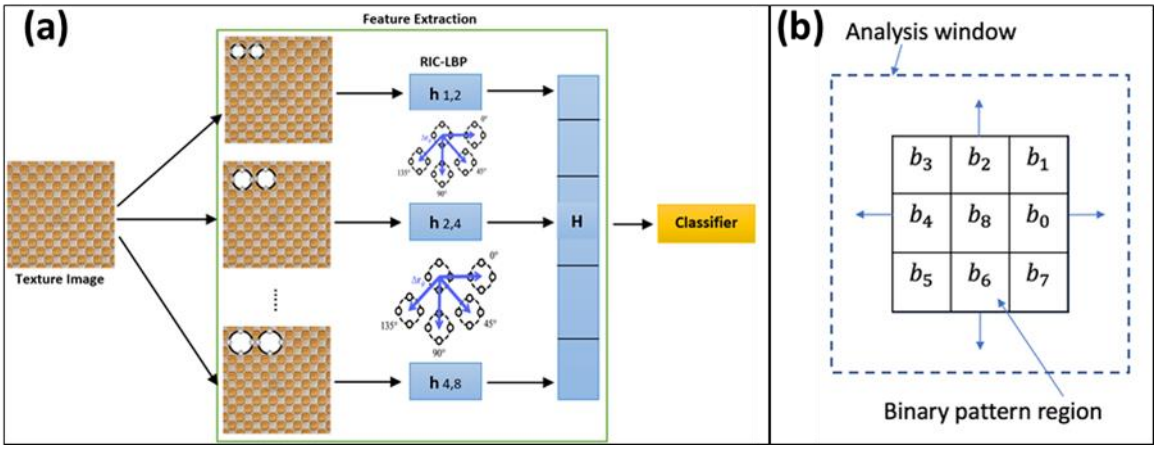

Figure 41. (a) RIC-LBP descriptor computed using three different radii. The final histogram is the concatenation of the three-radius RIC-LBP descriptor, (b) Illustration of the Adaptive Median Binary Pattern (AMBP) window [158].

B. Motif-Based Descriptors

1) JML: The Joint Motif Labels (JML) descriptor was proposed by Oraibi et. al [152]. The descriptor exploits the spatial relationship among intensity pixel in a 2 × 2 image neighborhood. This is done by finding the Optimum Peano scans among pixels by minimizing the energy of the intensities in a small image region based on the equation below:

$$\delta = |p_1 - p_2| + |p_2 - p_3| + |p_3 - p_4| \quad (10)$$

Figure 42a shows the 12 motif patterns extracted from a 2 × 2 neighborhood image with the corresponding letters for each pixel that are used in the minimization equation. In order to compute this descriptor, the twelve motif patterns are extracted from the 2 × 2 neighborhood. Then, these patterns are labeled from 1 - 12. Later, three moments are found: minimum, median, and maximum patterns. Then, the corresponding labels of these patterns are stored in 3 separate matrices. We repeat this process for all image pixels. At the end, we join each matrix with the mean and variance of the image in a 3D joint histogram mechanism. More details can be found in [152]. We also consider the translational invariance property of the descriptor by computing it on four different images: the original one, the original image shifted by one pixel horizontally, vertically, and diagonally by one pixel. As a result, we gain a descriptor that has 576 bins. **Figure 43** and **Figure 44** illustrate the computation of JML before and after translational invariance.

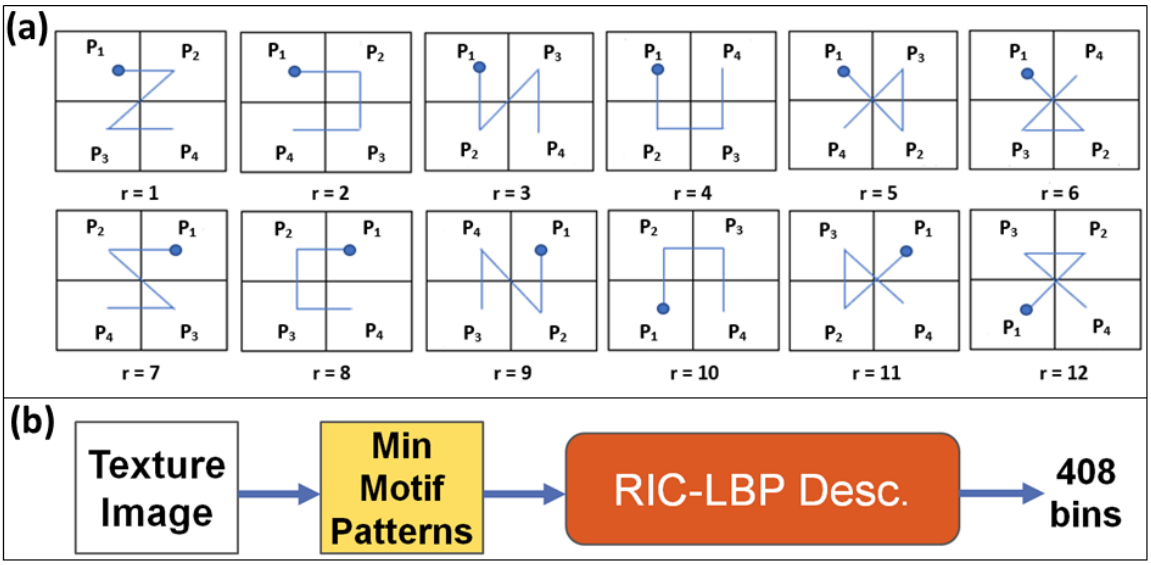

Figure 42. (a) The twelve Motif Patterns used in our approach, (b) Motif Patterns descriptor illustration. The minimum Motif Patterns matrix is encoded with RIC-LBP and 408 bins features are extracted [158].

2) MP: The Motif Patterns (MP) descriptor, which was also proposed by Oraibi et. al [152], works by exploiting the motif patterns extracted during the process of constructing the JML descriptor. These patterns are considered as intensity values since they represent the variation of intensity pixels in a specific neighborhood. As a result, we can exploit these patterns by encoding them using any texture descriptor as shown in **Figure 42b**. We selected the RIC-LBP descriptor to encode the minimum patterns only since it generates powerful features that result in high classification performance. To cope with translational invariance, we applied the same approach as in JML and extracted features from 4 images. The result is a descriptor that has 1632 bins which can be used during the classification stage. **Figure 43** and **Figure 44** illustrate the computation of JML before and after translational invariance.

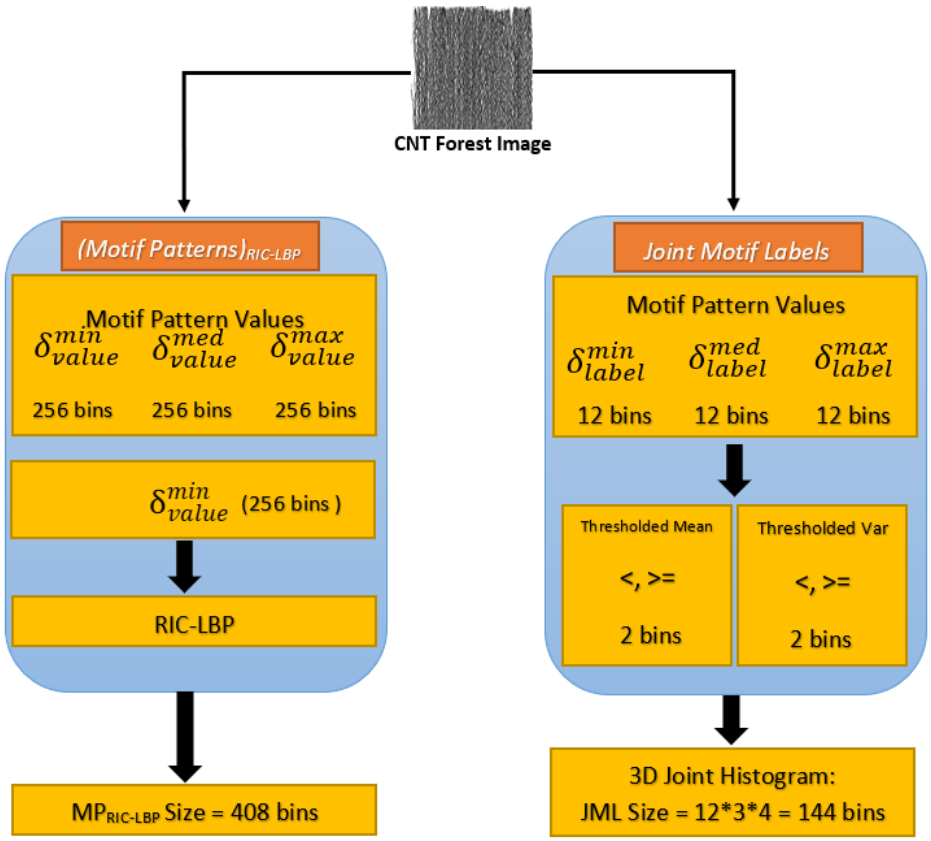

Figure 43. Feature Vector Calculations of JML and MP Descriptors before Applying the Translational Invariance.

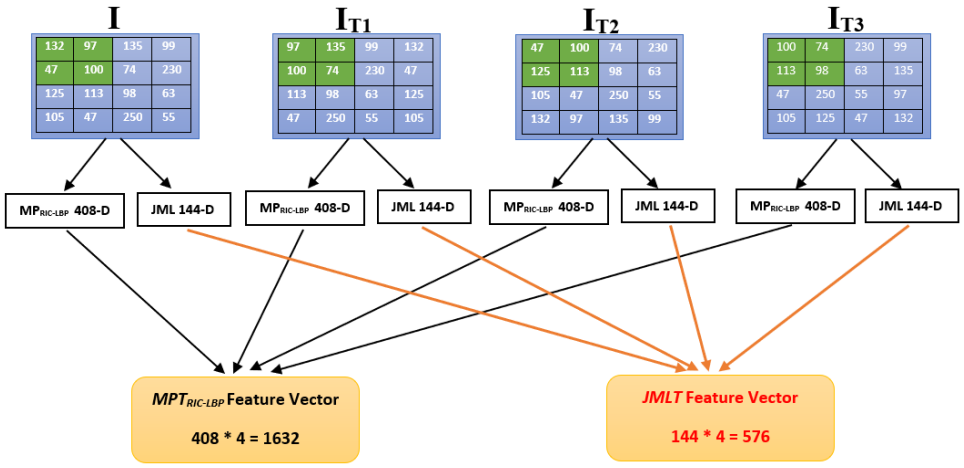

Figure 44. Computation of JML and MP descriptors after applying three different local translations including one pixel horizontal (T1), one pixel vertical (T2) and one pixel diagonal (t3) for translational invariance [158].

C. Random Forests (RF) Classifier

Random Forests (RFs) are an ensemble learning method for classification and regression. RFs operate by creating multiple decision trees and outputting the class that is the mode of the classes or mean prediction in

the case of the regression task [159]. The first algorithm for random decision was created by Tin Kam Ho. After that, an extension of Ho's algorithm was developed by Breiman et al. [160] which involves combining Breiman's "bagging" idea and random selection of features, introduced first by Ho et. al and resulted in the RFs classifier. The training algorithm for random forests applies the general technique of bootstrap aggregating, or bagging, to tree learners. The number of trees is a free parameter. Typically, a few hundred to several thousand trees are used, depending on the size and nature of the training set.

4.2.2 Results and discussion

In this section, we demonstrate the performance of our approach for classifying 12 CNT classes, defined later. We perform classification using 1000 trees RF classifier, which previously proved to be very efficient [150, 151]. During training and testing, we used 5-fold cross-validation, where 80% of data was used for training and the remaining 20% was used for testing. The evaluation metric used is the Mean Class Accuracy (MCA) which is defined as:

$$MCA = \frac{1}{K}\sum_{k=1}^{K} CCR_k \tag{11}$$

where K is the number of classes and CCR_k is the correct classification rate for each class. The dimensions of CNT forest images range between 192×730 and 627×730 where rows vary in size while columns have a fixed size. In the experiments, we did not re-size the images or alter them. This is because we are using local feature descriptors that accept any image size. In addition, the number of images per class ranges between 100 - 230.

A) CNT Forest Simulation:

CNT forests are simulated for a total number of twelve distinct classes employing three different CNT densities and four outer diameters. Population of CNTs with 250, 500 and 750 CNTs were grown on a 50 μm simulation domain, corresponding to a pitch of 200, 100 and 66.67 nm between CNT nucleation cites, respectively. For simplicity, the outer diameters are 5, 10, 15 and 20 nm, and deemed constant for all CNTs within the forest. CNTs are modeled as hollow cylinders assigned with inner diameters that were 70% of magnitude of outer diameters. The CNT forests were grown up to 1200 total growth steps that corresponds to a height of nearly 55 μm. The CNT growth rate undergoes a sigmoid behavior such that it is highest at the

onset of growth, gradually decreases, typically over the subsequent 20 minutes, and finally terminates [161]. However, our ML model training can be trained by simulating CNT forests for a relatively short length, i.e. up to 55 m in this study. This corresponds to the early stages of growth that is fulfilled within a few minutes [161]. Due to computational resources limitations, it takes about a few hours to simulate CNT forests by our finite-element simulation model. For instance, it takes about 2.5 hours to grow a forest of 55 m height with a pitch of 100 nm between nucleation cites while such forest is grown in less than 2 minutes experimentally [161]. Therefore, the growth rate of each CNT within the population was assigned stochastically from a Gaussian probability density function with an average growth rate of 50 nm per time step and a standard deviation of 5%. The orientation angle of CNTs was also assigned to each CNT based on a Gaussian distribution having a standard deviation of 5 relative to the growth substrate normal. Each class of CNT forests is simulated for several times to generate sufficient amount of data to train the ML model. CNT morphologies are plotted and saved every 100 time steps starting from time step of 300 up to 1200. The first 300 time steps are disregarded due to the short length of forests. Note that each forest morphology generated using similar synthesis attributes is different because of the stochastic assignment of attributes from user-defined distributions.

As discussed earlier, the twelve classes shown above have different densities and outer diameters. A representative image of each CNT forest class may be found in **Figure 45**. It should be noted that all simulation growth parameters are the same except for the CNT number density and outer diameters. The typical density of a CNT forest is 10^9-10^{13} [82-84, 127], while classes 1-to-4 corresponding to **Figure 45a-d** have CNT number densities of 0.25×10^{10} CNTs/cm^2, that exhibits similar morphology to **Figure 7b**. Classes 5-8 correspond to **Figure 45e-h** and have CNT number densities of 1×10^{10} CNTs/cm^2. Classes 9-12, as shown in **Figure 45i-l**, have CNT number densities of 2.25×10^{10} CNTs/cm^2, which resembles **Figure 7a**. A summary of synthesis parameters for the twelve class is shown in **Table 2**. The morphological changes arise from the interactions between adjacent CNTs that make neighboring CNTs bonded by the van der Waals forces and make bundles. The bonds are subject to breaking when the generated forces during the forest self-

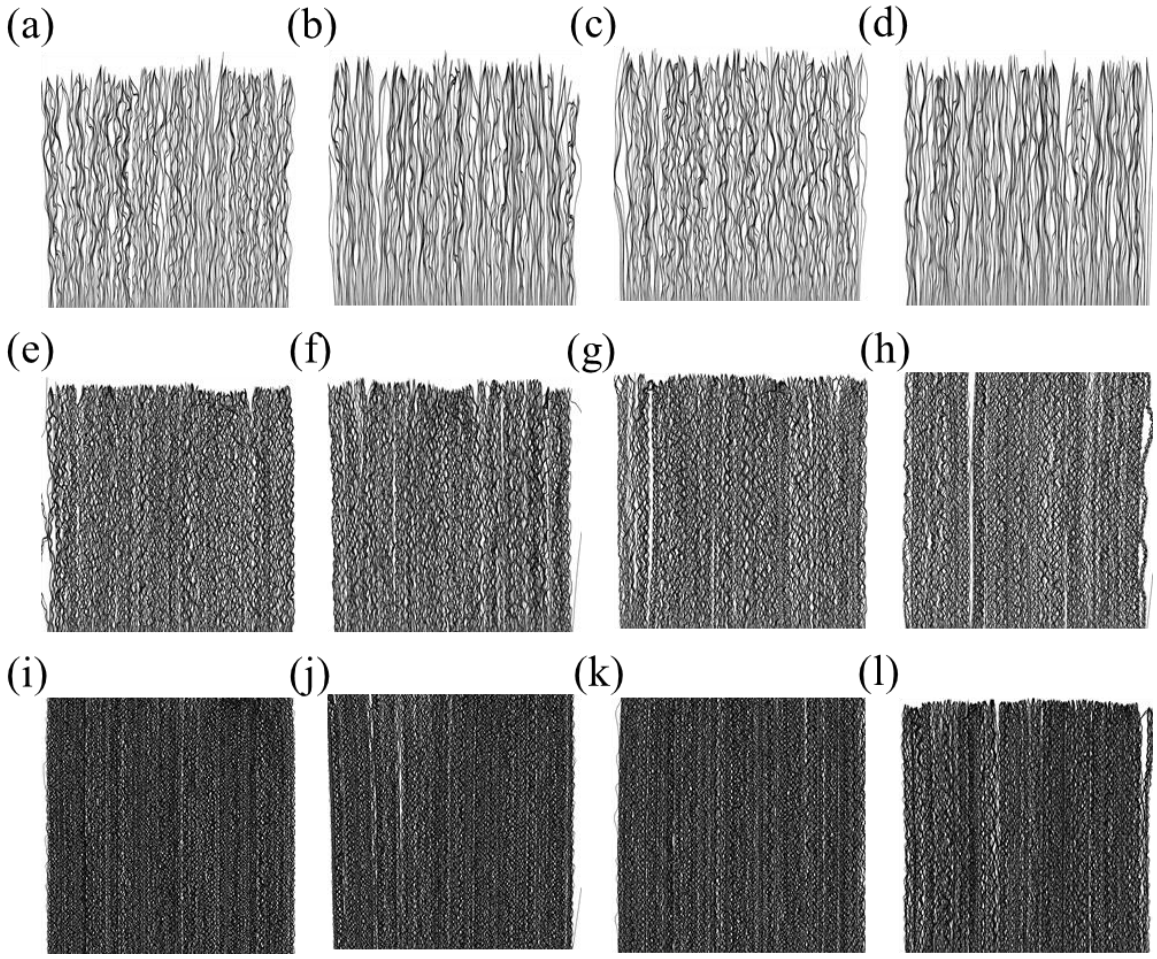

Figure 45. The CNT forest morphologies (a)class1: 250 CNTs - OD=5 nm (b) class2: 250 CNTs - OD=10 nm (c) class3: 250 CNTs - OD=15 nm (e) class4: 250 CNTs - OD=20 nm (e) class5: 500 CNTs - OD=5 nm (f) class6: 500 CNTs - OD=10 nm (g) class7: 500 CNTs - OD=15 nm (h) class8: 500 CNTs OD=20 nm (i) class9: 750 CNTs - OD=5 nm (j) class10: 750 CNTs - OD=10 nm (k) class11: 750 CNTs - OD=15 nm (l) class12: 750 CNTs - OD=20 nm [158].

assembly exceed a threshold force of 10 nN [105, 114]. It is worth noting that the x-y axis is cropped in **Figure 45** in order to convert plots to images that can be used to train the ML model.

Table 2. A summary of CNT forest simulation growth parameters with average growth rate of 50nm per timestep and growth STD of 5% [158].

Class No.	Outer Diameter (nm)	Inner Diameter (nm)	CNT Number (/50μm)	Avg. Growth Rate (nm/step)	Growth Rate STD (%)
1	5	3.5	250	50	5
2	10	7	250	50	5
3	15	10.5	250	50	5
4	20	14	250	50	5
5	5	3.5	500	50	5

6	10	7	500	50	5
7	15	10.5	500	50	5
8	20	14	500	50	5
9	5	3.5	750	50	5
10	10	7	750	50	5
11	15	10.5	750	50	5
12	20	14	750	50	5

B) Local Features Experiments:

Our experiment starts by classifying the CNT forest classes using our framework of four local descriptors: RIC-LBP, JAMBP, JML, and MP. The classification results were reported for each single descriptor as shown in **Table 3**. Then, the combination of descriptors is examined to further improve the classification performance.

Table 3. Results of applying our local features framework using 1000 trees RF with five-fold cross validation. After combining the four sets of feature descriptors, the MCA results improved by more than 3% [158].

Descriptor	**Size**	**MCA**
RIC-LBP	408	80.0
JAMBP	320	76.2
JML	576	80.5
MP	1624	79.4
RIC – LBP + JAMBP	728	79.9
RIC – LBP + JAMBP + JML	1304	81.6
RIC – LBP + JAMBP + JML + MP	2936	83.5

From **Table 3**, the best accuracy of a single local descriptor was obtained by JML. This is because JML uses the spatial relationship among the intensity pixel in a 2×2 neighborhood efficiently. JAMBP exhibited the lowest performance since it was not able to capture the important texture features from the dense tubes of CNT forest. This is mainly because JAMBP proved to work very well with noisy images while CNT forest images are very clean. It is observed that the combination of multiple local descriptors also enhanced the

classification performance. In the best case, combining the four descriptors resulted in a performance improvement by more than 3%. RF classifier with 1000 trees was tested before to classify Human Epithelial type 2 (HEp-2) images and it was very successful in recognizing six and seven classes of cells and specimen samples respectively [150, 151]. Hence, the RF classifier was selected to classify CNT forest images that yields impressive results as shown in Table II, when adopting the RF with many trees to aid the voting process within the classifier.

4.2.3 Conclusions

In this section, a framework of multiple local descriptors to classify 12 CNT forest classes corresponding to different synthesis conditions was presented. We split the dataset into 5 folds in order to perform 5-fold cross-validation. Then, the Random Forests classifier with 1000 trees was applied on the extracted local descriptors. We have studied several descriptors and demonstrated that the accuracy of a single local descriptor can be improved by concatenating multiple local descriptors and feeding them to the classifier. The accuracy of JML (the best single performance descriptor) was improved from 80.5% to 83.5% by combining all four descriptors: RIC-LBP, JAMBP, JML, and MP. This high classification accuracy promotes discovering the CNT forest synthesis-structure relationships so that their promising performance can be adopted in real world applications. We foresee this work as a meaningful step towards creating an unsupervised simulation using machine learning techniques that can seek out the desired CNT forest synthesis parameters to achieve desired property sets for diverse applications.

4.3 Discovering Carbon Nanotube Forest Process-Structure-Property Relationships Using High-Throughput Simulation and Deep Learning

It is essential to discover and fully control the underlying mechanism of synthesis and self-assembly of carbon nanotube (CNT) forests to accomplish the application-tailored CNT growth. One major step is to determine the process conditions based on the desired set of properties to achieve. However, exploring the broad range of growth parameters that dictate the CNT forest structure and properties is impractical due to the large number of parameters, the extensive possible combinations of synthesis conditions and the stochastic nature of CNT self-assembly. In this section, deep convolutional neural networks combined with

the physics-based simulation tool are employed to study the process-structure-property of CNTs. Deep learning (DL) enables prediction of ensemble properties based on morphological images that can further be correlated to the synthesis parameters though a DL classification algorithm. The simulation model is employed to generate CNT forests structural morphology using user-defined parameters. Another simulation is utilized to model the nanoindentation process to compress the forest to yield mechanical properties, namely buckling load and stiffness in this section. The investigated input parameters of simulation are CNT number density, the standard deviation of growth rate mismatch and CNT radius. These parameters are alternated to produce 63 different classes of CNT forest that are used along with corresponding morphological images and mechanical properties as the training dataset. A deep learning model referred to as "CNTNet" is developed and trained on 5 splits experiments of training, validation and test subsets data with outstanding accuracies of > 0.91 for predicting the process parameters and $R^2 > 0.96$ for buckling load and $R^2 > 0.94$ for stiffness prediction. These are promising results towards designing and manufacturing CNTs by design.

4.3.1 Methods

In **Figure 46**, we describe the process to explore process-structure-property relations of CNT forests. First, the finite element simulation model is employed to grow CNT forests of different synthesis attributes. The process parameters and the resulting structure are used to train a DL classification algorithm to correlate each CNT morphological structure to the corresponding synthesis parameters. Later, the synthesized CNT forest is compressed axially from the top surface to obtain ensemble properties, i.e. buckling load and stiffness in this work. As there are many growth conditions that result in a wide range of properties, a DL regression model is trained to predict the forest properties based on their structures.

4.3.1.1 Finite Element Simulation

In this section, among different input parameters, only CNT number density, growth rate standard deviation and outer radius are selected for investigation. It should be noted that other parameters like inner/outer radius ratio, average growth rate, standard deviation of angle of orientation and stiffness are kept constant for all realizations. CNT numbers per forest growth span (10 μm in this section) that determines the number density of forests takes 7 different values while the other two parameters, namely CNT outer radius and growth rate standard deviation, will take three different values to yield 63 distinct class of synthesis

conditions for the classification purpose. It was found that forest structure and properties are most sensitive to changes in CNT number density and CNT diameter (see **Figure 49**). Hence, simulations with higher variation in number density are let to run to produce a continuous buckling load space for a more accurate property prediction. The values that each parameter may take will be further discussed in details in the proceeding section.

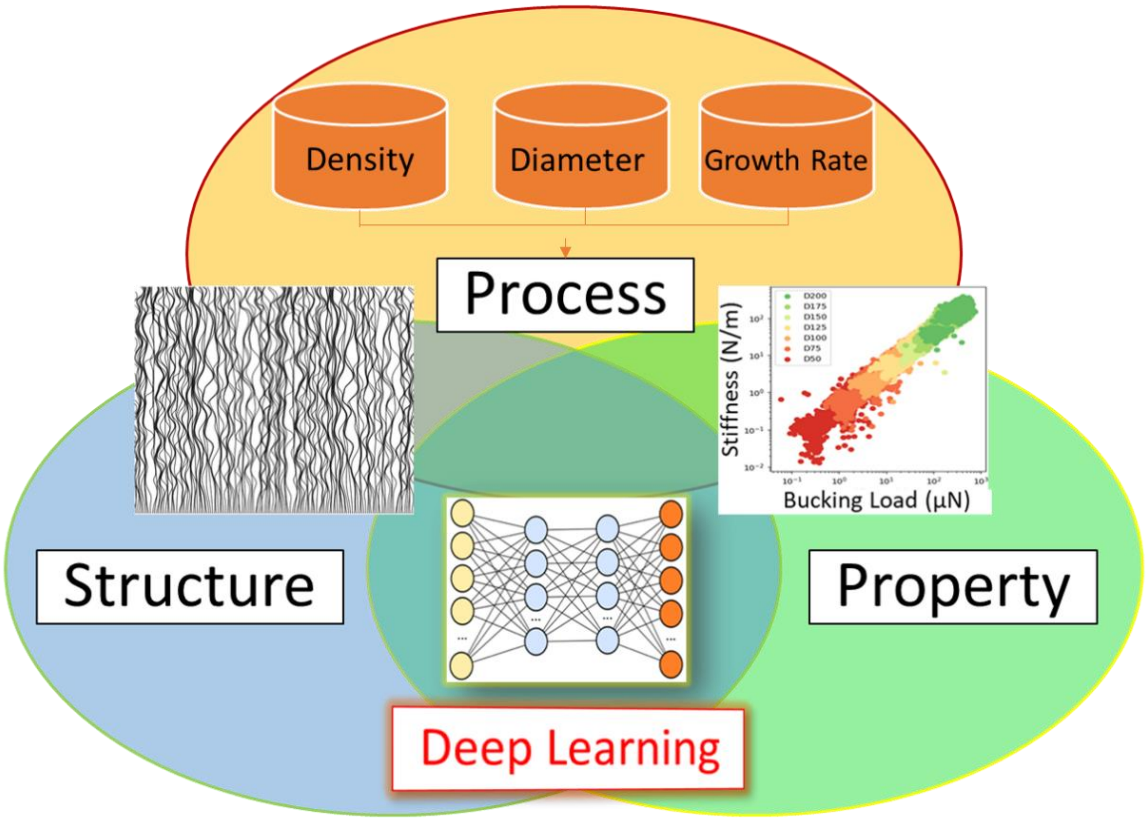

Figure 46. The proposed Process-Structure-Property mechanism using simulation and deep learning.

CNT forests are compressed using the compression simulation model as described in Chapter 2 to obtain the force necessary to buckle CNT forests. Compression of forests was simulated by a vertically translating and rigid platen that contacts the top surface of the forests. After the compressive load was applied to the top surface of forest, similar finite-element analysis concepts are used to solve for displacement and forces. The compression is applied by a constant platen translation per compression step and normal to the forest while the substrate is conceived as a rigid body. The reaction forces are calculated at each node in contact with the moving platen and summed up to obtain the compression force. The compression simulation is discussed in

detail in [10]. A typical CNT forest morphology at the end of growth and compression simulation are shown in **Figure 47a** and **Figure 47b**, respectively, as well as the corresponding force-displacement curves. **Figure 47c** shows the compression period when the buckling load is reached and how the buckling load and stiffness are calculated, while **Figure 47d** illustrates a longer compression time.

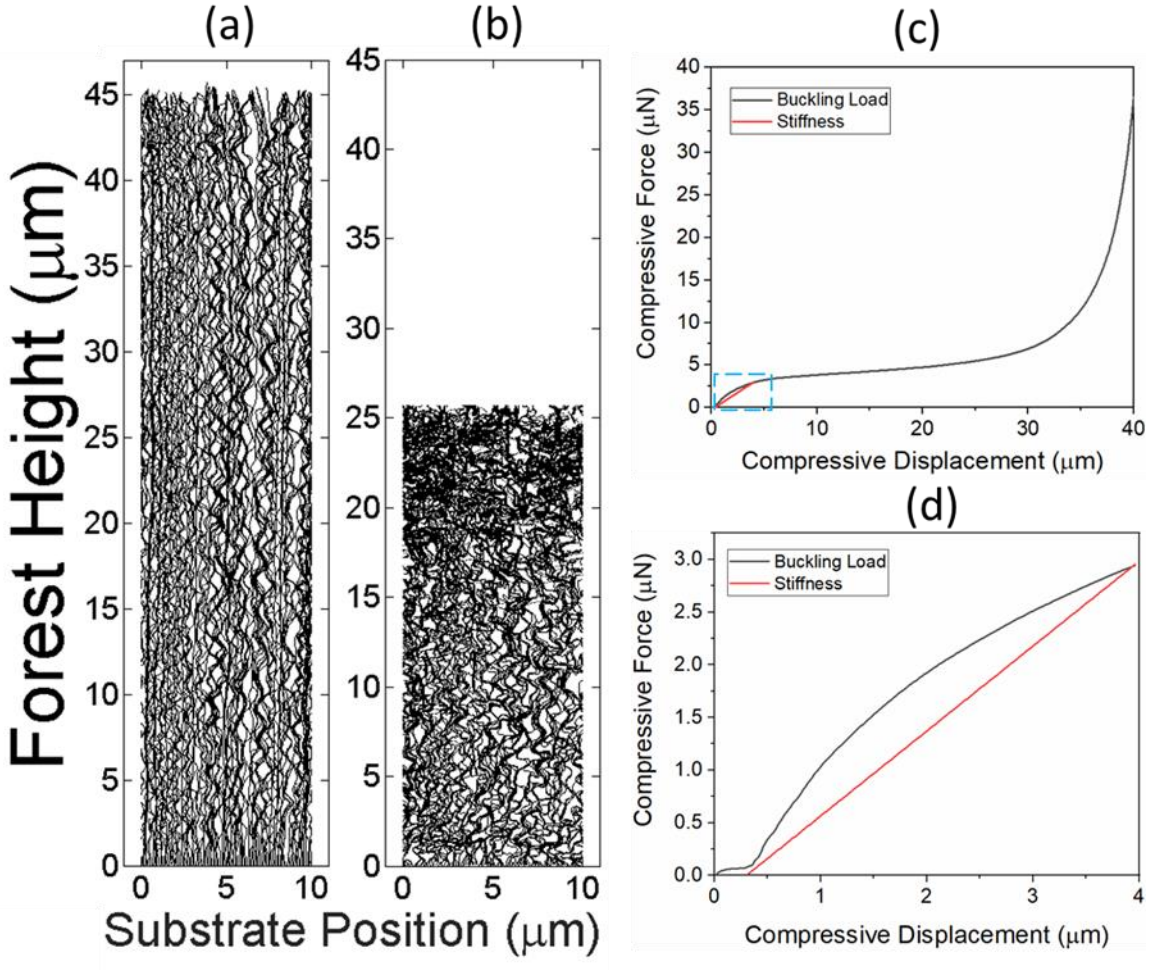

Figure 47. A typical simulated (a) internal structure morphology of CNT forest at the end of growth (b) internal structural morphology of CNT forest at the end of compression; and force-displacement plot (d) at the end of all compression steps corresponding to morphology of (b) exhibiting densification (d) the blue box in (c) representing buckling load and stiffness curves at the onset of forest buckling.

As discussed earlier, unfortunately there is no labeled CNT forest morphology (internal structure) dataset from physical experiments that can be used for ML/DL model training. Furthermore, as the parameter space of synthesis conditions is so vast, it is impractical, slow, and expensive to grow CNTs with different growth parameters. Hence, the physics-based simulation is employed to grow and characterize CNT forests to train various DL models to investigate their process-structure-property relationships. Accordingly, thousands of

simulations are run to generate sufficient amount of data. During mass simulation runs, attributes of each simulation realization, i.e. run number, number density, outer radius, and growth rate standard deviation, as well as labeled class numbers and the resulting buckling load and stiffness are stored in a database. Also, images are stored by their run number to correlate the image to the right property and labeled class as the input streamlines of DL model. The CNT forest images labeled with their respective classes are used to train a classification model that later will be employed to determine the synthesis conditions. On the other hand, the buckling load and stiffness obtained from compressing CNT forests are correlated to the structural morphology to construct a regression model that will be able to predict forest properties. Combining the classification and regression models will result in predicting synthesis conditions according to desired properties. This is a significant step towards growing CNTs by design.

4.3.1.2 Deep Learning Framework

In this section, we the proposed network framework for investigating the CNT forest process-structure-property relationships. As shown in **Figure 48**, there are totally five components in the proposed mechanism framework: Simulation Conditions, Physical Controlling, Algorithm Supervision, and CNTNet which is consisted of two DL modules: Structure Classification and Property Regression. Here, based on the forest structure (as the input to our DL models) we discuss how to predict the CNT synthesis parameters tuned for desired properties by means of classification and regression models. For both tasks, the supervision information is provided by the simulation. The proposed CNTNet is designed to handle two tasks together with shared feature representation space by transferring knowledge from structure to properties prediction. In the following sections, the details of each task design are stated.

A) CNT Classification

For the classification task, the CNT structural images are employed to classify CNT forests to different classes (63 for this study) based on combination of three growth parameters. This is treated as an image classification problem, which has been pervasively studied in many areas, such as natural object image classification [162], aerial scene classification[163], etc.

In our previous work [158], we proposed non-deep-learning based methods to explore the classification of CNT images. We exploited several representative hand-crafted descriptors for classification, i.e. Rotation

Invariant Co-occurrence among Local Binary Patterns (RIC-LBP) [155], Joint Adaptive Median Binary Patterns (JAMBP) [156], Joint Motif Labels (JML) [152], Motif Patterns (MP) [152], and investigate their effectiveness in texture analysis of morphology images. Upon development of deep learning which has successfully been applied to object recognition [162], object detection [164], point cloud segmentation, object tracking, etc., we believe that materials science should benefit from deep-learning based methods, and leverage the advantages of deep representations. The objective of this work is to utilize deep learning to facilitate exploring synthesis-structure-property relations of CNT forests. Hence, the popular convolutional neural networks (CNNs) are implemented to tackle the classification problem.

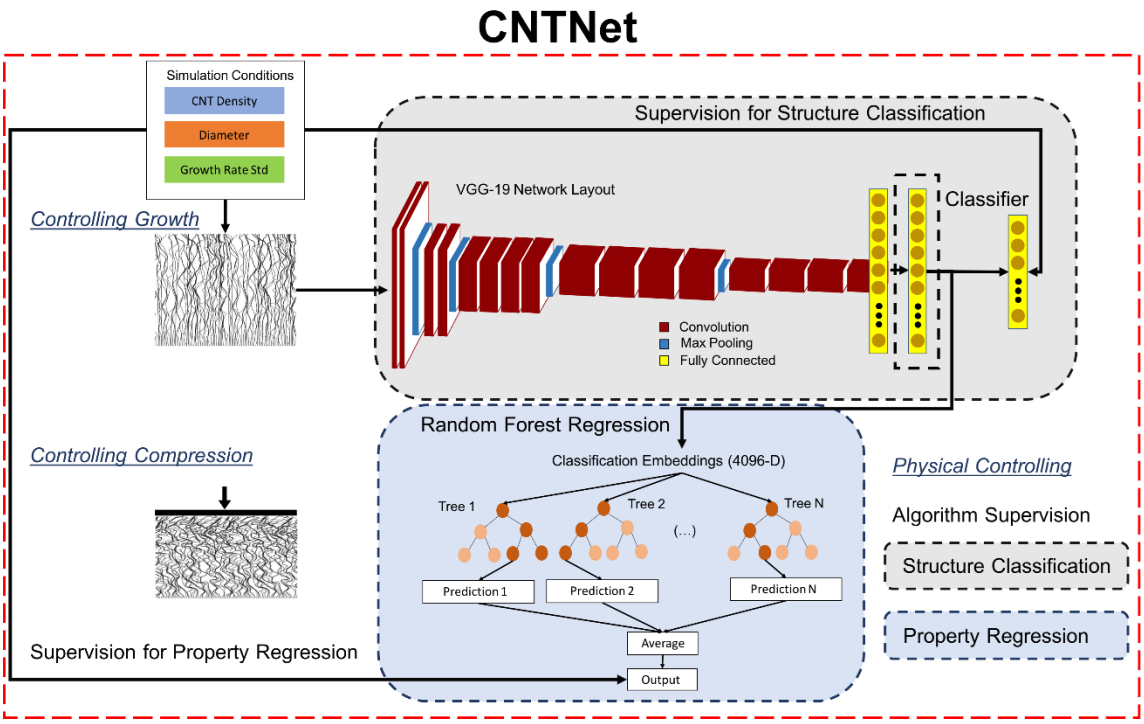

Figure 48. Framework of our proposed CNTNet for using machine learning to predict CNT material properties from (simulated) growth images. The top VGG-19 deep learning network is used to classify the image sample into one of 63 CNT classes. The network captures texture properties and was trained by initialization using ImageNet weights. The bottom Random Forest regression trees learns a 2-D regression function for mapping a 4096-D feature representation vector to two physical properties, namely buckling load and stiffness.

Here, we give mathematical formulation of proposed framework. Given the morphology images of CNT structures, $X_i \in X_{CNT}$, X_{CNT} is the training set of CNT images. In our approach, we propose to use convolutional neural network to learn the mapping function from CNT structure (images) to CNT classes. We define the $f_{\theta_{cls}}(\cdot)$ (parameterized by the network parameters θ_{cls}) as the mapping function from input image X_i to the class label p_i, which is presented in:

$$\hat{p}_i = Softmax(f_{\theta_{cls}}(X_i)) \tag{12}$$

$$Softmax(z)_i = \frac{e^{z_i}}{\sum_{j=1}^{K} e^{z_j}} \quad for\ i = 1, \dots, K \ \ and\ z = (z_1, \dots, z_K) \in \mathbb{R}^K$$

where $\hat{p}_i$ is the prediction label.

During training, we use the cross-entropy loss, as computed:

$$L_{cls} = -\frac{1}{N}\sum_{i=1}^{N}(p_i \log(\hat{p}_i) + (1 - p_i)\log(1 - \hat{p}_i)) \tag{13}$$

where p_i is the true label (1 for target class label and 0 for other classes), $\hat{p}_i$ is the predicted probability of the predicting label of X_i, and N is the mini-batch-size during training. In our experiments, we implemented VGG-19 [165] as the backbone network, and used the Stochastic Gradient Decent (SGD) optimizer to optimize the parameter space θ_{cls}. More details are discussed in the following section.

B) CNT property regression

To facilitate exploring the vast space of properties of CNTs, and later correlate Process-Structure-Property relations, a non-linear regression is applied on CNT mechanical properties, namely buckling load and stiffness in this work. For Structure-Property mechanism learning procedure, based on the input images of CNT structures, a regression model is trained to predict the properties of CNTs.

We propose a network which transfers the classification embeddings to property regression, i.e. CNTNet, as shown in **Figure 48**. The framework is designed by the motivation that the proper ties are strongly correlated to the CNT structures as depicted in **Figure 49** where only buckling load and stiffness values for the three CNT numbers of 100, 150 and 200 are shown. Non-linear regression is applied on the dataset presented in **Figure 49** to find how the relationship between the properties (buckling load and stiffness) and synthesis conditions (CNT number, outer diameter, and growth rate STDV) scaled, when a single variable is isolated at a time. The resulting regression equations are shown in **Table 4** that tries to approximate the synthesis-property relationships. The suggested framework of regression is illustrated in **Figure 48**. Instead of directly learning from CNT structures (morphology images), we propose a transfer learning method which utilizes the prior knowledge we learn from the classification task to facilitate the learning of CNT properties such as bucking load and stiffness. Experiments present promising results of our CNTNet in which the

knowledge from classification of CNTs is transferred to predict the properties of CNTs as an effective and efficient transfer learning method.

Table 4. The regression equations that fit the data presented in **Figure 49** as a function of CNT number (density), diameter, and growth rate std. dev.

	CNT Number (N)	**Outer Diameter (D)**	**Growth Rate STDV (G)**
Buckling Load (BL)	$BL= 2E\text{-}07N^{3.923}$	$BL = 0.957D^{2.015}$	$BL = -0.964G^2 + 21.708G + 23.75$
Stiffness (S)	$S= 0.008N^2 - 1.195N + 49.807$	$S= 1.079D^2 - 1.437D - 4.073$	$S= -0.638G^2 + 10.117G + 25.861$

We utilize the learning space of the embeddings of 63 classes to boost the prediction of regression. There are two components of CNTNet. The first component is the classification embedding extraction network, which is learned by the above classification task. After the network finishes training, all the parameters θ_{cls} is frozen, so that the learning knowledge in the training can be kept during property prediction procedure. The second component is Random Forest regression (RF regression) [166, 167].

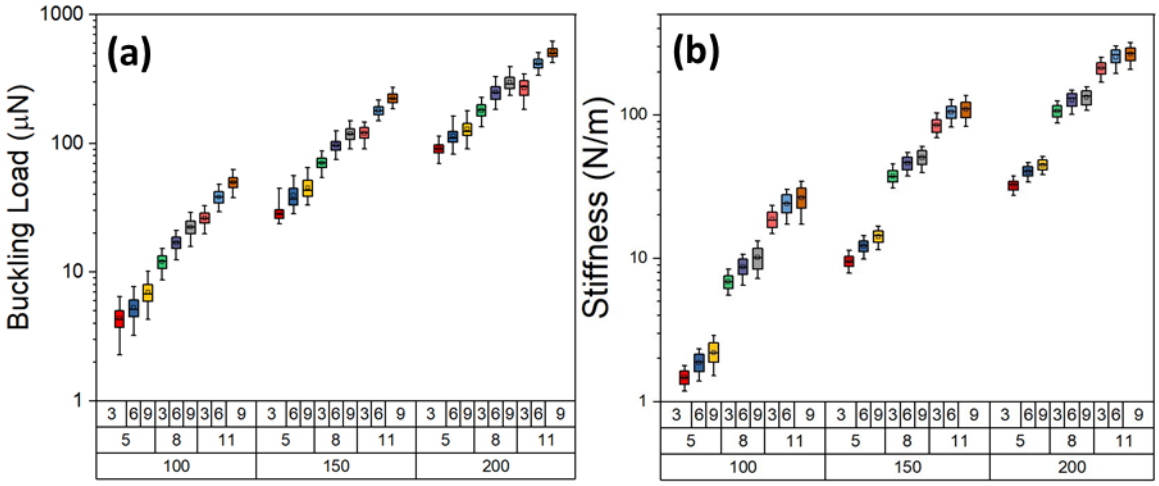

Figure 49. Nested box plot of (a) buckling load, and (b) stiffness for all combinations of the input simulation parameters. The bottom most level is the CNT density, then Growth Rate Standard Deviation (3, 6, 9) and Outer Radius (5, 8, 11).

The classification embedding is defined as $d_{cls}^{i} \in \mathbb{R}^{E}$ of the CNT image input X_i, where E is the dimension of the classification embedding vector. The $f_{\theta_{cls}}(\cdot)$ (parameterized by the RF regression θ_{reg}) is defined as the mapping function from the classification space to the property space. We define the property output is $y_i \in R^2$ where one dimension out for buckling load, and the other dimension output is stiffness, as described in Eq.

(14). The reason we use one RF regression to predict the properties of buckling load and stiffness together is based on the observation of **Figure 50** where the linear correlation of two properties are clearly demonstrated.

$$d_{cls}^{i} = f_{\theta_{cls}}(X_i) \tag{14}$$

$$\hat{y}_{reg}^{i} = f_{\theta_{reg}}(d_{cls}^{i})$$

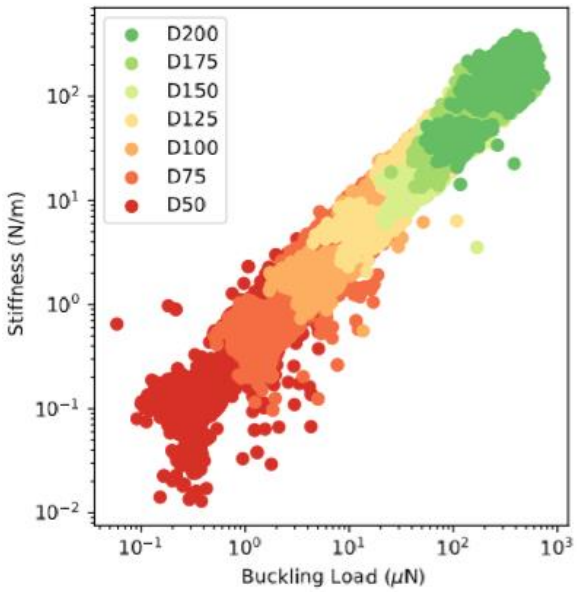

Figure 50. Correlation of Buckling Load vs Stiffness

4.3.2 Results and discussion

A) Simulation

The finite-element simulation is used here to synthesize and characterize CNT forests. Several user defined parameters are employed to simulate CNT forests such as growth span, CNT numbers, growth rate, angle of orientation, outer and inner radii, Young's modulus, etc. Later, the compression simulation model is employed to model CNT forest post-synthesis characterization that yields forest properties like buckling load and stiffness. Whereas in this study, due to the large number of growth input variables, only three parameters were selected to investigate their effect on the resulting forest morphology, namely CNT number density (D), CNT outer radius (R) and growth rate mismatch standard deviation (G). The common synthesis input parameters are shown in **Table 5**. Also, the studied synthesis conditions as the variable inputs of the growth simulation is displayed in **Table 6**. It is worth noting that for simplicity, the outer radius is considered

constant for all CNTs within the forest. Here, among various properties, only buckling load and stiffness are studied for the regression model. The outputs of growth and compression simulation used for ML/DL training are the CNT internal morphology stored as images and the forest properties stored as numerical values. It should be noted that the input synthesis parameters are also used for classification purposes.

Table 5. Common synthesis conditions used as the inputs of the growth simulation.

Parameter	**Value**
Growth Domain	100 (μm)
Average Growth Rate	60 (nm/step)
Growth Steps	400
Inner Diameter	70% Outer Diameter
Average Angle of Orientation	90 (degrees)
Standard Deviation of Angle of Orientation	5 (degrees)
Young's Modulus	1 (TPa)

Table 6. The investigated input synthesis parameters used as the inputs of the growth simulation.

Parameter	**Value**						
Number Density (/10μm)	50	75	100	125	150	175	200
Outer Diameter (nm)	10	16	22				
Growth Rate STD. Dev.	3	6	9				

Growth and compression simulation are conducted for over 22,000 times for all possible combination of input parameters to provide sufficient number of images for DL modeling. Each CNT forest is let to grow until it reaches 20 μm of height where the morphology is saved as the forest structure images. Following, the compression simulation is run until the force necessary to buckle the forest is reached. The buckling load and the corresponding stiffness are also stored as numerical values. A nested box plot of buckling load and stiffness is shown in **Figure 49** for only three CNT number values, i.e. 100, 150, and 200, including all other combinations of simulated process conditions.

The DL models are trained for classification and regression to explore the process-synthesis-property relations of CNT forests. At first, a DL classification with 12 classes is carried out to classify forests based on their structure. An accuracy of 95.5% is achieved using VGG19 architecture which is a great improvement

to the accuracy of similar classification with hand-engineered feature extractors with an accuracy of about 83.5% [158]. As 12 classes only could cover a few synthesis parameters, other classifications with higher number of classes is tried that resulted in slightly lower accuracies of 91% due to the increased number of classes. Although classification is a good step towards exploration of synthesis-structure relations, it is not solely helpful when predicting CNT forest properties. Hence, regression models are trained using the forest morphology images to predict the forest buckling load and stiffness.

B) Deep Learning Implementation

The details of our experimental data are listed in **Table 7** where a total of 22,106 synthesized images are used. 60% of images are used for training, while 20% for validation, and 20% for testing are allocated. For both classification and regression tasks, the VGG-19 network [165] is employed as the backbone network. The size of our generated images is 907 × 725. while the input size of a standard VGG-19 is 224×224. Thus, during training, the images are resized to 256×256 initially, followed by the random crop application to get to the image size of 224×224. During validation and testing, we first resize image to 256 × 256, and then do center cropping of image to size 224×224. All hyperparameters are listed in **Table 8**. The learning rate for training is 0.001, with a mini-batch-size of 32. We trained the network for 200 epochs and used the validation data to select the best model. Then, the selected model is tested on the testing data. The applied optimizer is SGD with a momentum of 0.9 and weight decay of 1e−4. For the regressor, the classification embedding is extracted from the last fully connected layer, whose dimension is 4096. We use the random forest regressor for the regression of final property values. The Scikit-learn [168] is employed for the implementation of RF. Totally, 1000 decision trees are used, and the stopping condition is all leaves are pure. All other settings of RF are the same as Scikit-learn default settings. During training, we use common augmentation processing; random cropping for each image, and random flip with 0.5 probability. All experiments are conducted in 5-Fold cross-validation settings. For regression tasks, we compute log values of buckling load and Stiffness.

Table 7. Descriptions of Dataset.

Classes No.	Total # of images	Training	Validation	Testing
63	22,106	13,263	4,421	4,422

Table 8. Details of Hyper-parameters in different experiments.

Initial LR	Optimizer	Weight Decay	Momentum	Mini-Batch Size
0.001	SGD	$1e^{-4}$	0.9	32

C) Data Details

In **Figure 51**, we show one image of 9 classes for each CNT density. We enlarge the red box of CNT50 images and green box of CNT200 images. In **Figure 52**, we show the distributions of controlling attributes of the whole dataset. Each class has about 200 to 400 images. Also, the typical buckling load and stiffness values for CNT forests with 100, 150 and 200 CNTs are already shown in **Figure 49**.

D) Evaluation Metrics

For the classification task, we use the standard accuracy evaluation metric, while for the regression, we use two evaluation metrics; R^2 and RMSE to evaluate our performance. The implementations are from Scikit-learn [168].

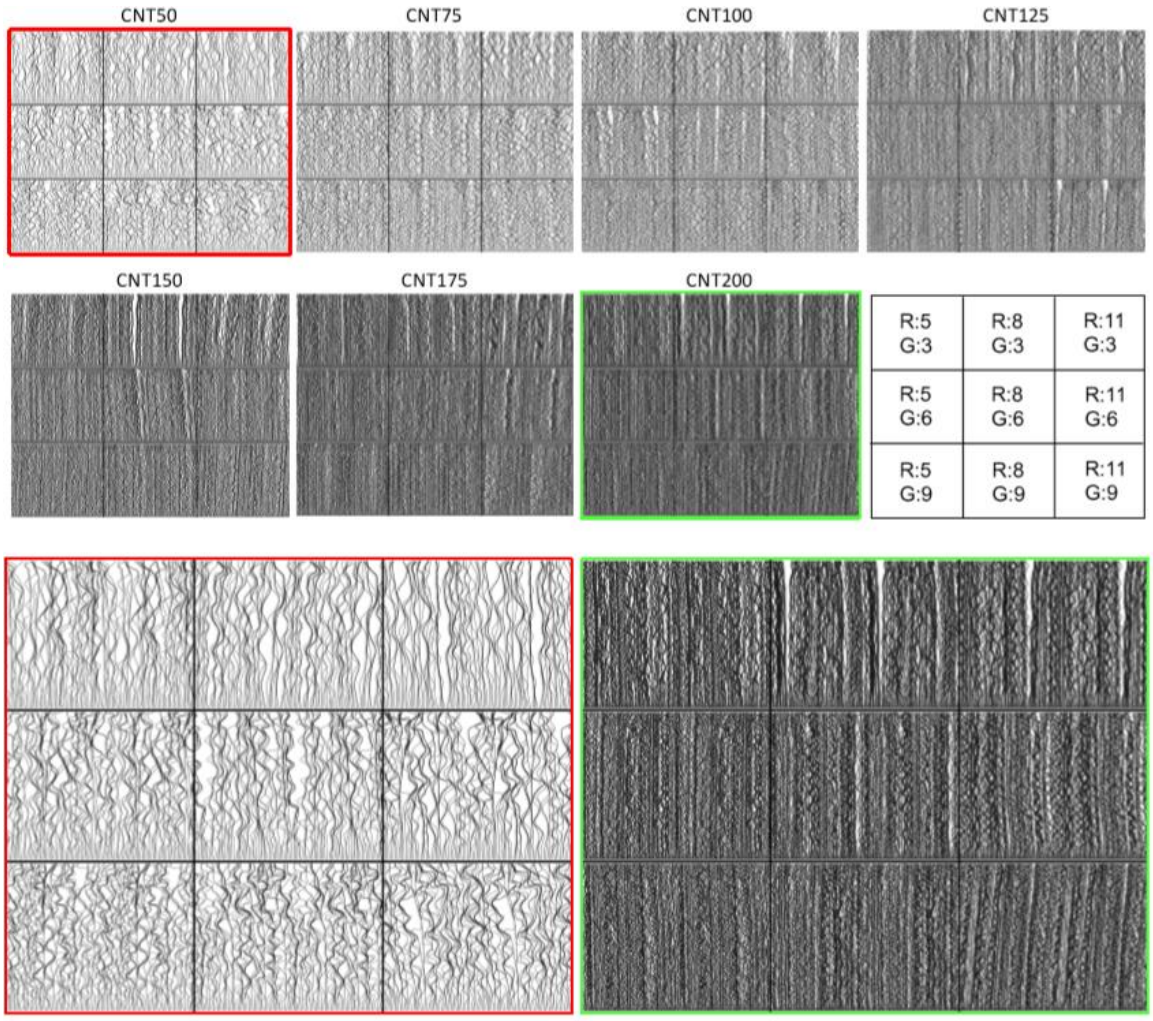

Figure 51. Sample simulation images for 63 total classes composed of three radii and three growth rate standard deviation combinations, for seven CNT density values. We abbreviate Outer Radius as R, and Growth Rate Standard Deviation as G. Sample images for CNT50 (red highlight) and CNT200 (green highlight) are shown at zoomed scale in the third row for each CNT density.

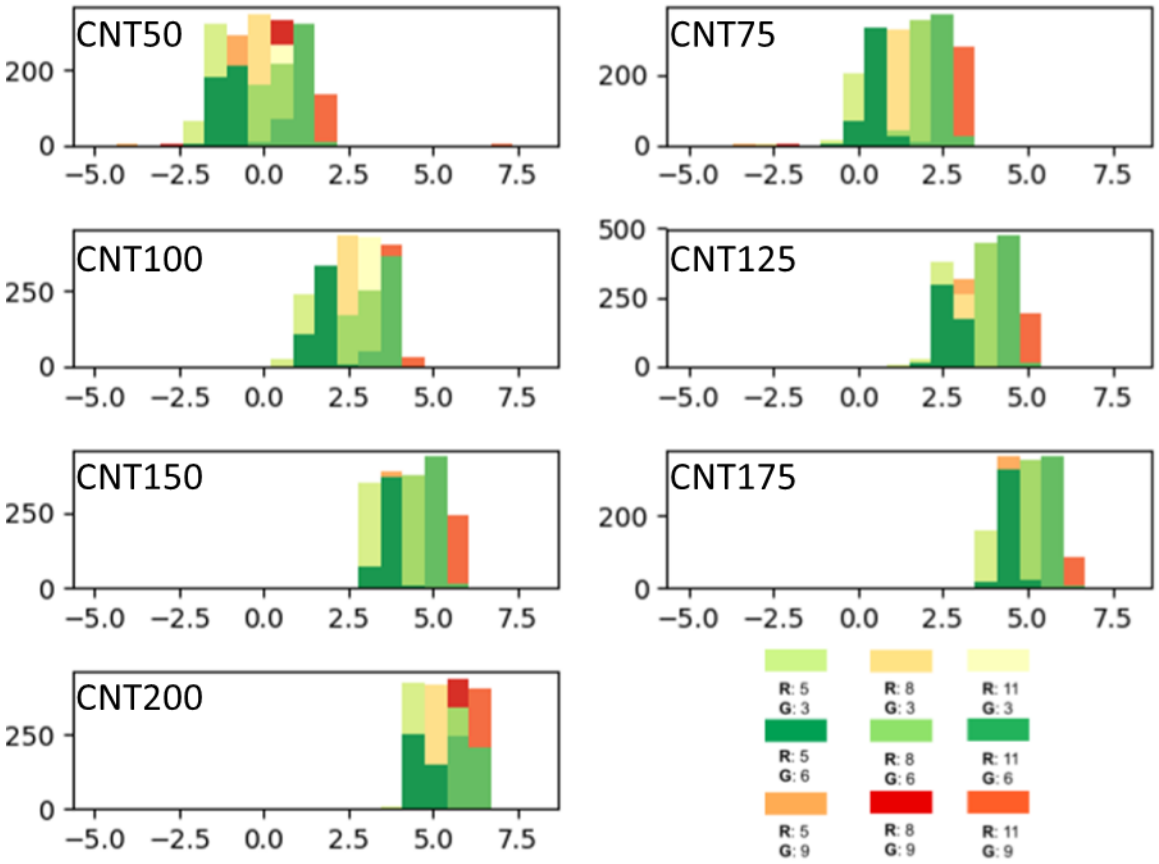

Figure 52. Distribution of sample synthetic simulation images. For each plot the x-axis is the logarithm of buckling load and the y-axis is frequency. We abbreviate Outer Radius as R, and Growth Rate Standard Deviation as G. For each CNT density, histogram of the number of samples for each CNT density with 9 classes.

(I) R^2 score computed as:

$$R^2(y, \hat{y}) = 1 - \frac{\sum_{i=1}^{n}(y_i - \hat{y}_i)}{\sum_{i=1}^{n}(y_i - \bar{y})^2} \tag{15}$$

$$\bar{y} = \frac{1}{n}\sum_{i=1}^{n} y_i$$

$$\sum_{i=1}^{n}(y_i - \hat{y}_i)^2 = \sum_{i=1}^{n} \in_i{}^2$$

(II) RMSE computed as:

$$RMSE = \sqrt{\sum_{i=1}^{n} \frac{(y_i - \hat{y}_i)^2}{n}} \tag{16}$$

E) Experimental Results

We mainly compared current results with our previous work [158] which used hand-crafted features based on RIC-LBP, JAMBP, JML, MP. In **Table 9**, we also show our results using VGG-19 with 12 number of classes. We can see that the results of deep learning network VGG-19 significantly suppresses the previous non-DL method accuracies. In this work, we have investigated classification for 63 classes while only 12 classes were studied for previous studies. However, the accuracy of 91.01% is promising for 63 classes.

Table 9. Performance of hand-crafted non-deep learning vs deep learning (DL) methods for the CNT classification task using 12 and 63 classes. Performance decreases by only 4.5 percent for significantly more classes.

Method	**Class No.**	**Accuracy (%)**
Hand-crafted ML model **[158]**	12	83.5
DL VGG-19	12	95.5
DL VGG-19 (Extended)	63	91.0

i) Classification Analysis

In **Table 10**, we report the classification accuracy of each CNT densities values. The confusion matrix results of 63 classes classification is visualized in **Figure 53a**. It is seen that most confusions of classes are in self CNT density space.

Table 10. Classification accuracy using 5-fold validation on the testing data with the results shown as mean accuracy and standard deviation.

Overall	**D50**	**D75**	**D100**	**D125**	**D150**	**D175**	**D200**
91.01±0.54	79.64±2.34	84.65±0.88	89.72±0.90	92.81±0.25	96.88±0.51	97.08±0.45	97.75±0.29

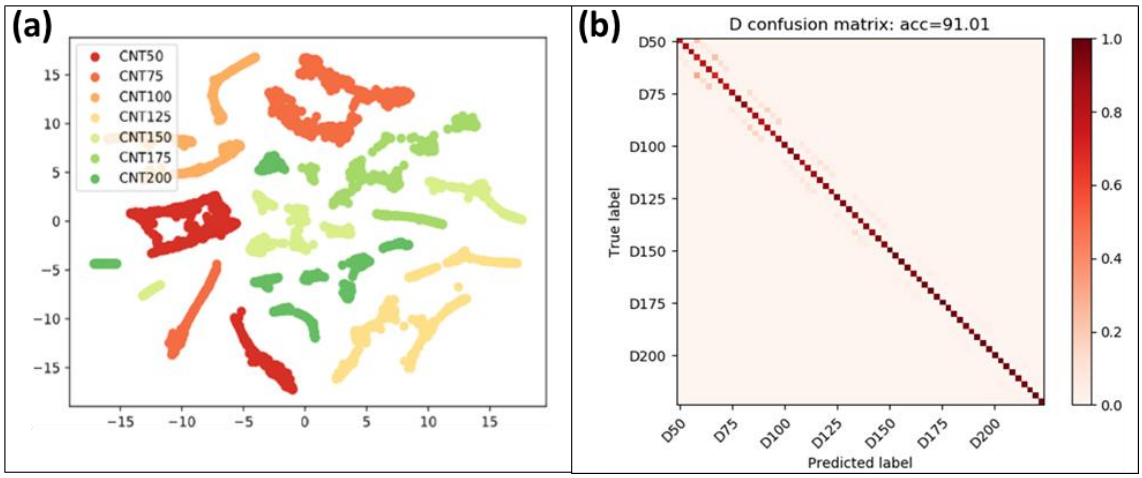

Figure 53. (a) t-SNE visualization of the 63 classes grouped into the 7 CNT densities for better visual display showing the separation of the groups using the VGG-19 feature embedding sub-space (b) Confusion Matrix of 63 classes from 7 CNT densities.

In order to visualize the performance of our learned embeddings, we chose classical visualization methods t-SNE [169] to visualize the learned space of classification, as shown in **Figure 53b**. We first use PCA [170] to reduce the dimension of classification embeddings from 4096 to 50, and then used t-SNE to visualize them in 2D space. For clear visualization, we plot the testing data classification embedding distribution. It is clearly observed that the different CNT densities are well-separated. The confusions mainly happen in each CNT densities own sub 9 classes space.

ii) Property Regression Analysis

In **Table 11** and **Table 12**, the quantitative results are reported. The visualization of regression results in log scale is shown in **Figure 54**, which demonstrate that our CNTNet is very promising and encouraging for CNT property prediction. We report the common regression evaluation metric R^2 and RMSE of each CNT density in **Table 11** and **Table 12** where the overall R^2 is 0.96 for buckling load and 0.94 for stiffness. Interestingly, the overall metrics represent better results compared to each CNT density since the whole distribution is aligned better with the simulation computation results than each CNT density range.

Table 11. Performance of buckling load regression in $\log_e$ scale.

	Overall	D50	D75	D100	D125	D150	D175	D200
R^2	0.96±0.00	0.66±0.05	0.75±0.02	0.80±0.02	0.83±0.01	0.89±0.00	0.88±0.01	0.86±0.02
RMSE	0.39±0.01	0.58±0.03	0.46±0.02	0.38±0.02	0.32±0.01	0.23±0.01	0.22±0.01	0.22±0.02

Table 12. Performance of stiffness regression in loge scale.

	Overall	D50	D75	D100	D125	D150	D175	D200
R^2	0.94±0.03	0.62±0.04	0.72±0.02	0.81±0.01	0.85±0.00	0.91±0.01	0.91±0.00	0.91±0.01
RMSE	0.49±0.02	0.74±0.04	0.61±0.02	0.46±0.02	0.38±0.01	0.27±0.02	0.25±0.00	0.23±0.14

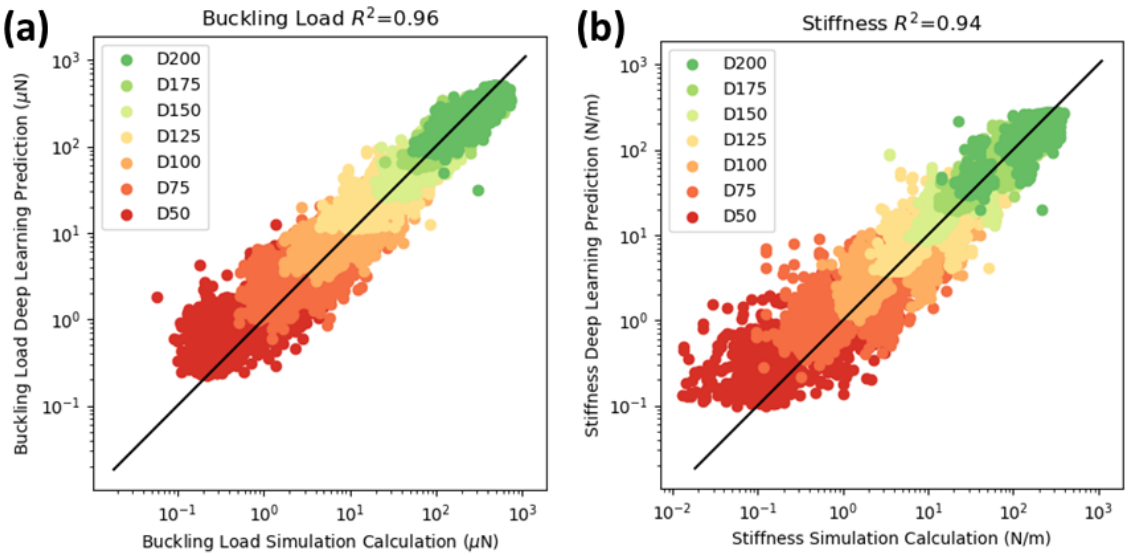

Figure 54. (a) Buckling load (b) Stiffness regression compared to simulation ground-truth for seven different CNT densities using a random forest regression method with deep learning VGG-19 texture features (4096-D).

F) Summary of Deep Learning Method

We modelled the proposed mechanism of Process-Structure-Property of CNT forests using our designed DL method, i.e. CNTNet. We studied the Process-Structure relations as classification problem, and the Structure-Property ones as regression problem. For the whole mechanism, we propose CNTNet to tackle both classification and regression problem which leverage the knowledge from structure to help predict proper

ties, specifically, CNTNet leverages the prior knowledge from CNT structure to boost the property predictions of CNT which efficiently combine the structure knowledge and property knowledge. Experiments demonstrate the promising results on classification and property predictions. This encouraging outcome supports our proposed concepts of modeling the mechanism with deep learning framework.

4.3.3 Conclusion

In this work, in order to investigate the process-structure-property relations of CNT forests, advanced high-throughput computation modeling is combined with emerging deep learning algorithms. This cutting-edge data-driven model represents a promising approach to engineer CNT synthesis based on intended ensemble applications. Hence, over 22,000 CNT forest are synthesized numerically followed by a compression simulation to obtain forest structures and properties, namely buckling load and stiffness. A deep neural network model is trained to correlate each forest structure to process conditions through classification (63 classes, here); subsequently another regression model is applied to predict CNT properties using morphological images as inputs. The results present fabulous accuracies of > 0.91 for classification and R^2 > 0.96 and 0.94 for the prediction of buckling load and stiffness, respectively. This is a successful step towards building an active learning, closed-loop system that employs multiple sources of information including SEM CNT imagery, finite element simulation predictions, physical measurements and a knowledgebase of previous experimental results or mined from the literature to accelerate adoption of CNT forest within various industrial applications.

CHAPTER 5

CONCLUSIONS AND FUTURE WORK

5.1 Conclusions

The existing paradigm for developing new materials is slow, serial, data-poor, and artificially bound by human preconception of anticipated results. New advanced computational, experimental and data-driven tools should be used to achieve control, function, and integration of nanoscale building blocks, however, it will likely be more difficult than the creation of the nanoscale units themselves. The barriers inhibiting the control of nanoscale materials are many, including: (1) equipment sets to observe dynamic nanoscale phenomena in-situ have only recently become available; (2) digital analysis techniques of experimental data is often incomplete or non-existent; (3) iteratively navigating multi-dimensional parameter spaces requires vast financial and time resources; (4) human observation is often biased, error-prone, and is serial in nature; (5) simulations of multi-scale phenomena are sparse and must be validated with experimental data that often do not yet exist. This work attempted to address these areas by examining the growth kinetics and assembly of CNT forests. Exploring how these fundamental mechanisms are influenced by the vast synthesis parameter space for CNTs will provide new understanding of the processing-structure-property relationships of CNT forests. This new integrated design continuum — incorporating greater use of computing and information technologies coupled with advances in characterization and experiment — will significantly accelerate the discovery and development time of materials by replacing lengthy and costly empirical studies with mathematical models and computational simulations.

An experimental exploration of the full synthesis parameter space is both cost and time prohibitive. Numerical simulation of CNT forests synthesis and self-assembly is an alternative approach that may increase the speed and diversity of synthesis parameters examined. Such simulations can predict both the CNT forest structural morphology and the resulting CNT forest properties. By systematically varying CNT synthesis parameters, one may arrive at a set of conditions that product the desired CNT forest performance metrics

such as mechanical stiffness and thermal conductivity. These desired performance metrics are intricately related to the structural morphology of the CNT forest itself, although the functional relationships between CNT forest structural morphology and CNT forest properties are currently not well understood. Moreover, the time-resolved simulation is able to calculate the mechanical forces due to CNT-CNT interactions (arising from growth rate mismatch) at any time step during growth. As well, post synthesis characterizations like compression and tension tests are modelled by the simulation to obtain mechanical properties of CNT forests.

In-situ SEM experiments are carried out to study growth kinetics at individual CNT scale. Although, many improvements are made to facilitate growth and enhance imaging resolution, only some successful growth experiments are observed. There are some barriers (most importantly the low chamber base pressure) that should be resolved to hopefully end in an effective synthesis recipe.

Finally, modern machine and deep learning algorithms are used in this work to build a prediction model on CNT forest properties based on their structure which can then be used to predict the synthesis conditions. We have achieved significant accuracies of (~>94%) that is a good indicative how efficient data-driven approach is to explore process-structure-property relationships of CNT forests. This work is a meaningful step towards creating an unsupervised simulation using machine/deep learning techniques that can seek out the desired CNT forest synthesis parameters. Therefore, predicting the combination of processing parameters required to grow application-tailored CNT forests would represent a significant advance that could enable new CNT forest-based applications that fully exploit the beneficial properties of individual CNTs.

5.2 Future Work

Although there is a decent amount of work dedicated to developing the simulation model, still there are other areas that can be further developed and implemented to the simulation package such as:

1- Studying the force-modulated growth rates in depth to accommodate mechanochemical kinetics.
2- Applying non-linear finite-element analysis
3- Correlating user-defined inputs of simulation with experimental processing conditions
4- Implementing variable density behavior during growth to resemble densification, decay and termination stages and validating with experimental results

5- Deriving electrical and thermal properties of CNT forests considering wider conditions

In-situ CNT growth seems very promising to understand ensemble collective kinetics. Although, many improvements are made, but more experiments with better tools of decreasing chamber base pressure should be conducted to study various synthesis conditions and their effect on forest morphology and properties. This is an integral part of the finite-element simulation validation. Also, numerous SEM imaging should be performed to make a database to train DL models as an important part of the active-learning model.

Finally, construction of the closed-loop AI-driven model requires implementing image analysis of SEM imaging that should take place in real-time on a cloud environment. So, preparing such an infrastructure is essential to provide a robust, deterministic methodology for discovering materials with prescribed property sets for specific engineering applications.

BIBLIOGRAPHY

[1] S. Iijima, Helical microtubules of graphitic carbon, nature 354(6348) (1991) 56.
[2] G. Dresselhaus, S. Riichiro, Physical properties of carbon nanotubes, World scientific1998.
[3] M.J. Treacy, T.W. Ebbesen, J.M. Gibson, Exceptionally high Young's modulus observed for individual carbon nanotubes, nature 381(6584) (1996) 678-680.
[4] M. Zhang, K.R. Atkinson, R.H. Baughman, Multifunctional carbon nanotube yarns by downsizing an ancient technology, Science 306(5700) (2004) 1358-1361.
[5] M.D. Lima, S. Fang, X. Lepró, C. Lewis, R. Ovalle-Robles, J. Carretero-González, E. Castillo-Martínez, M.E. Kozlov, J. Oh, N. Rawat, Biscrolling nanotube sheets and functional guests into yarns, Science 331(6013) (2011) 51-55.
[6] A.M. Marconnet, N. Yamamoto, M.A. Panzer, B.L. Wardle, K.E. Goodson, Thermal conduction in aligned carbon nanotube–polymer nanocomposites with high packing density, ACS nano 5(6) (2011) 4818-4825.
[7] T. Ebbesen, H. Lezec, H. Hiura, J. Bennett, H. Ghaemi, T. Thio, Electrical conductivity of individual carbon nanotubes, Nature 382(6586) (1996) 54-56.
[8] A.D. Franklin, Z. Chen, Length scaling of carbon nanotube transistors, Nature nanotechnology 5(12) (2010) 858-862.
[9] M.R. Maschmann, G.J. Ehlert, S.J. Park, D. Mollenhauer, B. Maruyama, A.J. Hart, J.W. Baur, Visualizing strain evolution and coordinated buckling within CNT arrays by in situ digital image correlation, Advanced Functional Materials 22(22) (2012) 4686-4695.
[10] M.R. Maschmann, Integrated simulation of active carbon nanotube forest growth and mechanical compression, Carbon 86 (2015) 26-37.
[11] D. Walters, L. Ericson, M. Casavant, J. Liu, D. Colbert, K. Smith, R.J.A.P.L. Smalley, Elastic strain of freely suspended single-wall carbon nanotube ropes, 74(25) (1999) 3803-3805.
[12] W. Ding, L. Calabri, K. Kohlhaas, X. Chen, D. Dikin, R.J.E.M. Ruoff, Modulus, fracture strength, and brittle vs. plastic response of the outer shell of arc-grown multi-walled carbon nanotubes, 47(1) (2007) 25-36.
[13] B. Peng, M. Locascio, P. Zapol, S. Li, S.L. Mielke, G.C. Schatz, H.D.J.N.n. Espinosa, Measurements of near-ultimate strength for multiwalled carbon nanotubes and irradiation-induced crosslinking improvements, 3(10) (2008) 626.
[14] G. Overney, W. Zhong, D. Tomanek, Structural rigidity and low frequency vibrational modes of long carbon tubules, Zeitschrift für Physik D Atoms, Molecules and Clusters 27(1) (1993) 93-96.
[15] S. Iijima, C. Brabec, A. Maiti, J. Bernholc, Structural flexibility of carbon nanotubes, The Journal of chemical physics 104(5) (1996) 2089-2092.
[16] L. Vaccarini, C. Goze, L. Henrard, E. Hernandez, P. Bernier, A. Rubio, Mechanical and electronic properties of carbon and boron–nitride nanotubes, Carbon 38(11-12) (2000) 1681-1690.
[17] L.J.P.o.t.R.s.o.L.S.A. Brazier, containing papers of a mathematical, p. character, On the flexure of thin cylindrical shells and other" thin" sections, 116(773) (1927) 104-114.
[18] K. Jensen, W. Mickelson, A. Kis, A.J.P.R.B. Zettl, Buckling and kinking force measurements on individual multiwalled carbon nanotubes, 76(19) (2007) 195436.
[19] O. Blakslee, D. Proctor, E. Seldin, G. Spence, T.J.J.o.a.p. Weng, Elastic constants of compression-annealed pyrolytic graphite, 41(8) (1970) 3373-3382.
[20] J. Bernholc, C. Brabec, M. Buongiorno Nardelli, A. Maiti, C. Roland, B. Yakobson, Theory of growth and mechanical properties of nanotubes, Applied Physics A: Materials Science & Processing 67(1) (1998).
[21] S.C. Chowdhury, B.Z.G. Haque, J.W. Gillespie Jr, D.R. Hartman, Molecular simulations of pristine and defective carbon nanotubes under monotonic and combined loading, Computational materials science 65 (2012) 133-143.
[22] N. Hu, Z. Masuda, C. Yan, G. Yamamoto, H. Fukunaga, T. Hashida, The electrical properties of polymer nanocomposites with carbon nanotube fillers, Nanotechnology 19(21) (2008) 215701.
[23] M. Dresselhaus, G. Dresselhaus, A.J.A.R.M.R. Jorio, Unusual properties and structure of carbon nanotubes, 34 (2004) 247-278.

[24] B. Wei, R. Vajtai, P.J.A.P.L. Ajayan, Reliability and current carrying capacity of carbon nanotubes, 79(8) (2001) 1172-1174.
[25] T.J. Sisto, L.N. Zakharov, B.M. White, R. Jasti, Towards pi-extended cycloparaphenylenes as seeds for CNT growth: investigating strain relieving ring-openings and rearrangements, Chemical science 7(6) (2016) 3681-3688.
[26] M. Dresselhaus, G. Dresselhaus, J.-C. Charlier, E. Hernandez, Electronic, thermal and mechanical properties of carbon nanotubes, Philosophical Transactions of the Royal Society of London. Series A: Mathematical, Physical and Engineering Sciences 362(1823) (2004) 2065-2098.
[27] R.S. Ruoff, D.C.J.c. Lorents, Mechanical and thermal properties of carbon nanotubes, 33(7) (1995) 925-930.
[28] T. Yamada, Y. Hayamizu, Y. Yamamoto, Y. Yomogida, A. Izadi-Najafabadi, D.N. Futaba, K. Hata, A stretchable carbon nanotube strain sensor for human-motion detection, Nature nanotechnology 6(5) (2011) 296.
[29] M.R. Maschmann, G.J. Ehlert, B.T. Dickinson, D.M. Phillips, C.W. Ray, G.W. Reich, J.W. Baur, Bioinspired Carbon Nanotube Fuzzy Fiber Hair Sensor for Air-Flow Detection, Advanced Materials 26(20) (2014) 3230-3234.
[30] M.R. Maschmann, B. Dickinson, G.J. Ehlert, J.W. Baur, Force sensitive carbon nanotube arrays for biologically inspired airflow sensing, Smart Materials and Structures 21(9) (2012) 094024.
[31] M. Arabghahestani, S. Poozesh, N.K. Akafuah, Advances in Computational Fluid Mechanics in Cellular Flow Manipulation: A Review, Applied Sciences 9(19) (2019) 4041.
[32] M. Arabghahestani, S. Karimian, Molecular dynamics simulation of rotating carbon nanotube in uniform liquid argon flow, Journal of Molecular Liquids 225 (2017) 357-364.
[33] B.A. Cola, X. Xu, T.S. Fisher, Increased real contact in thermal interfaces: A carbon nanotube/foil material, Applied physics letters 90(9) (2007) 093513.
[34] B.A. Cola, J. Xu, C. Cheng, X. Xu, T.S. Fisher, H. Hu, Photoacoustic characterization of carbon nanotube array thermal interfaces, Journal of applied physics 101(5) (2007) 054313.
[35] J. Xu, T.S. Fisher, Enhancement of thermal interface materials with carbon nanotube arrays, International Journal of Heat and Mass Transfer 49(9-10) (2006) 1658-1666.
[36] R.A. DiLeo, M.J. Ganter, M.N. Thone, M.W. Forney, J.W. Staub, R.E. Rogers, B.J. Landi, Balanced approach to safety of high capacity silicon–germanium–carbon nanotube free-standing lithium ion battery anodes, Nano Energy 2(2) (2013) 268-275.
[37] R.A. DiLeo, A. Castiglia, M.J. Ganter, R.E. Rogers, C.D. Cress, R.P. Raffaelle, B.J. Landi, Enhanced capacity and rate capability of carbon nanotube based anodes with titanium contacts for lithium ion batteries, Acs Nano 4(10) (2010) 6121-6131.
[38] M.W. Forney, R.A. DiLeo, A. Raisanen, M.J. Ganter, J.W. Staub, R.E. Rogers, R.D. Ridgley, B.J. Landi, High performance silicon free-standing anodes fabricated by low-pressure and plasma-enhanced chemical vapor deposition onto carbon nanotube electrodes, Journal of power sources 228 (2013) 270-280.
[39] R.A. DiLeo, S. Frisco, M.J. Ganter, R.E. Rogers, R.P. Raffaelle, B.J. Landi, Hybrid germanium nanoparticle–single-wall carbon nanotube free-standing anodes for lithium ion batteries, The Journal of Physical Chemistry C 115(45) (2011) 22609-22614.
[40] R. Carter, B. Davis, L. Oakes, M.R. Maschmann, C.L. Pint, A high areal capacity lithium–sulfur battery cathode prepared by site-selective vapor infiltration of hierarchical carbon nanotube arrays, Nanoscale 9(39) (2017) 15018-15026.
[41] A. Anvari, Effect of nano carbon percentage on properties of composite materials, J. Chem. Eng. Mater. Sci 8(4) (2017) 31-36.
[42] A. Anvari, Fatigue life prediction of unidirectional carbon Fiber/epoxy composite on Mars, Journal of Chemical Engineering and Materials Science 8(8) (2017) 74-100.
[43] A. Anvari, Thermal fatigue life of carbon nanotube wire and unidirectional carbon fiber/epoxy composite (UCFEC) in earth orbit, Journal of Chemical Engineering and Materials Science 8(8) (2017) 101-111.
[44] A. Anvari, Thermal Life of Carbon Structures: From the Earth to after the Titan, International Journal of Aerospace Engineering 2018 (2018).
[45] M. Ishida, H. Hongo, F. Nihey, Y. Ochiai, Diameter-controlled carbon nanotubes grown from lithographically defined nanoparticles, Japanese journal of applied physics 43(10B) (2004) L1356.
[46] M. Ramezani, Y.H. Kim, B. Hasanzadeh, Z. Sun, Influence of Carbon Nanotubes on SCC Flowability, 8th Int. RILEM Symp. Self-Compacting Concr., Washington DC, USA 15-18 May, 2016, pp. 397-406.

[47] M. Ramezani, Y.H. Kim, Z. Sun, Mechanical Properties of Carbon Nanotube Reinforced Cementitious Materials: Database and Statistical Analysis, Magazine of Concrete Research (2019) 1-62.
[48] M. Ramezani, Y.H. Kim, Z. Sun, Modeling the mechanical properties of cementitious materials containing CNTs, Cement and Concrete Composites (2019) 103347.
[49] M. Taherzadeh, M. Baghani, M. Baniassadi, K. Abrinia, M. Safdari, Modeling and homogenization of shape memory polymer nanocomposites, Composites Part B: Engineering 91 (2016) 36-43.
[50] M. Park, B.A. Cola, T. Siegmund, J. Xu, M.R. Maschmann, T.S. Fisher, H. Kim, Effects of a carbon nanotube layer on electrical contact resistance between copper substrates, Nanotechnology 17(9) (2006) 2294.
[51] M. Nihei, A. Kawabata, D. Kondo, M. Horibe, S. Sato, Y. Awano, Electrical properties of carbon nanotube bundles for future via interconnects, Japanese journal of applied physics 44(4R) (2005) 1626.
[52] T. Palma, M. Munther, P. Damasus, S. Salari, A. Beheshti, K.J.J.o.M.P. Davami, Multiscale mechanical and tribological characterizations of additively manufactured polyamide 12 parts with different print orientations, 40 (2019) 76-83.
[53] H. Peng, Q. Li, T. Chen, Industrial applications of carbon nanotubes, William Andrew2016.
[54] B. FIEDLER, F.H. GOJNY, M.H. WICHMANN, W. BAUHOFER, K. SCHULTE, Can carbon nanotubes be used to sense damage in composites?, Annales de chimie, Lavoisier, 2004, pp. 81-94.
[55] E.T. Thostenson, T.W. Chou, Carbon nanotube networks: sensing of distributed strain and damage for life prediction and self healing, Advanced Materials 18(21) (2006) 2837-2841.
[56] F. Mobadersani, H. Safari, T. Hajilounezhad, P. Kahroba, The Effect of Fluid Properties on the Operation of Thermal Bubble jet, arXiv:.07901 (2019).
[57] O. Kimizuka, O. Tanaike, J. Yamashita, T. Hiraoka, D.N. Futaba, K. Hata, K. Machida, S. Suematsu, K. Tamamitsu, S. Saeki, Electrochemical doping of pure single-walled carbon nanotubes used as supercapacitor electrodes, Carbon 46(14) (2008) 1999-2001.
[58] N. Muralidharan, E. Teblum, A.S. Westover, D. Schauben, A. Itzhak, M. Muallem, G.D. Nessim, C.L. Pint, Carbon Nanotube Reinforced Structural Composite Supercapacitor, Scientific reports 8(1) (2018) 17662.
[59] X. He, N. Fujimura, J.M. Lloyd, K.J. Erickson, A.A. Talin, Q. Zhang, W. Gao, Q. Jiang, Y. Kawano, R.H. Hauge, Carbon nanotube terahertz detector, Nano letters 14(7) (2014) 3953-3958.
[60] E. Artukovic, M. Kaempgen, D. Hecht, S. Roth, G. Grüner, Transparent and flexible carbon nanotube transistors, Nano letters 5(4) (2005) 757-760.
[61] Q. Cao, H.-s. Kim, N. Pimparkar, J.P. Kulkarni, C. Wang, M. Shim, K. Roy, M.A. Alam, J.A. Rogers, Medium-scale carbon nanotube thin-film integrated circuits on flexible plastic substrates, Nature 454(7203) (2008) 495.
[62] T. Hajilounezhad, Numerical evaluation of dry-cooling towers interaction in different arrangement, (2019).
[63] Z. Wu, Z. Chen, X. Du, J.M. Logan, J. Sippel, M. Nikolou, K. Kamaras, J.R. Reynolds, D.B. Tanner, A.F. Hebard, Transparent, conductive carbon nanotube films, Science 305(5688) (2004) 1273-1276.
[64] Y. Huang, P.V. Palkar, L.-J. Li, H. Zhang, P. Chen, Integrating carbon nanotubes and lipid bilayer for biosensing, Biosensors and Bioelectronics 25(7) (2010) 1834-1837.
[65] L. Qu, L. Dai, Gecko-foot-mimetic aligned single-walled carbon nanotube dry adhesives with unique electrical and thermal properties, Advanced materials 19(22) (2007) 3844-3849.
[66] L. Qu, L. Dai, M. Stone, Z. Xia, Z.L. Wang, Carbon nanotube arrays with strong shear binding-on and easy normal lifting-off, Science 322(5899) (2008) 238-242.
[67] C. Liang, L. Ji, H. Mousavi, C. Sandu, Evaluation of Tire Traction Performance on Dry Surface Based on Tire-Road Contact Stress, SIAR International Congress of Automotive and Transport Engineering: Science and Management of Automotive and Transportation Engineering, Springer, 2019, pp. 138-152.
[68] B. Mashadi, H. Mousavi, M.J.I.J.o.A.E. Montazeri, Obtaining relations between the Magic Formula coefficients and tire physical properties, 5(1) (2015) 911-922.
[69] A. Ghabussi, N. Ashrafi, A. Shavalipour, A. Hosseinpour, M. Habibi, H. Moayedi, B. Babaei, H.J.M.B.D.o.S. Safarpour, Machines, Free vibration analysis of an electro-elastic GPLRC cylindrical shell surrounded by viscoelastic foundation using modified length-couple stress parameter, (2019) 1-25.
[70] A. Ghorbanpour Arani, M. Emdadi, H. Ashrafi, M. Mohammadimehr, S. Niknejad, A. Ghorbanpour Arani, A.J.J.o.S.M. Hosseinpour, Analysis of Viscoelastic Functionally Graded Sandwich Plates with CNT Reinforced Composite Face Sheets on Viscoelastic Foundation, 11(4) (2019) 690-706.

[71] A. Ghorbanpour Arani, B. Rousta Navi, M. Mohammadimehr, S. Niknejad, A. Ghorbanpour Arani, A.J.J.o.S.M. Hosseinpour, Pull-In Instability of MSGT Piezoelectric Polymeric FG-SWCNTs Reinforced Nanocomposite Considering Surface Stress Effect, 11(4) (2019) 759-777.
[72] M. Shokrieh, M.S.J. Kondoria, Effects of adding graphene nanoparticles in decreasing of residual stresses of carbon/epoxy laminated composites, 2(1) (2020) 53.
[73] T. Hajilounezhad, S. Safari, M. Aliehyaei, Multi-Objective Optimization of Solid Oxide Fuel Cell/GT Combined Heat and Power System: A comparison between Particle Swarm and Genetic Algorithms, (2020).
[74] R. Rao, C.L. Pint, A.E. Islam, R.S. Weatherup, S. Hofmann, E.R. Meshot, F. Wu, C. Zhou, N. Dee, P.B. Amama, Carbon nanotubes and related nanomaterials: critical advances and challenges for synthesis toward mainstream commercial applications, ACS nano 12(12) (2018) 11756-11784.
[75] Y. Ando, X. Zhao, T. Sugai, M. Kumar, Growing carbon nanotubes, Materials today 7(10) (2004) 22-29.
[76] S. Ncube, Electronic properties of single walled carbon nanotubes synthesized by laser ablation, 2014.
[77] C. Bower, O. Zhou, W. Zhu, D. Werder, S.J.A.P.L. Jin, Nucleation and growth of carbon nanotubes by microwave plasma chemical vapor deposition, 77(17) (2000) 2767-2769.
[78] I. Song, Y. Cho, G. Choi, J. Park, D.J.D. Kim, r. materials, The growth mode change in carbon nanotube synthesis in plasma-enhanced chemical vapor deposition, 13(4-8) (2004) 1210-1213.
[79] S. Esconjauregui, B. Bayer, M. Fouquet, C. Wirth, C. Ducati, S. Hofmann, J. Robertson, Growth of high-density vertically aligned arrays of carbon nanotubes by plasma-assisted catalyst pretreatment, Applied Physics Letters 95(17) (2009) 173115.
[80] S.M. Kim, C.L. Pint, P.B. Amama, D.N. Zakharov, R.H. Hauge, B. Maruyama, E.A. Stach, Evolution in catalyst morphology leads to carbon nanotube growth termination, The Journal of Physical Chemistry Letters 1(6) (2010) 918-922.
[81] P.B. Amama, C.L. Pint, S.M. Kim, L. McJilton, K.G. Eyink, E.A. Stach, R.H. Hauge, B. Maruyama, Influence of alumina type on the evolution and activity of alumina-supported Fe catalysts in single-walled carbon nanotube carpet growth, ACS nano 4(2) (2010) 895-904.
[82] M. Bedewy, A.J. Hart, Mechanical coupling limits the density and quality of self-organized carbon nanotube growth, Nanoscale 5(7) (2013) 2928-2937.
[83] M. Bedewy, E.R. Meshot, M.J. Reinker, A.J. Hart, Population growth dynamics of carbon nanotubes, ACS nano 5(11) (2011) 8974-8989.
[84] M. Bedewy, E.R. Meshot, H. Guo, E.A. Verploegen, W. Lu, A.J. Hart, Collective mechanism for the evolution and self-termination of vertically aligned carbon nanotube growth, The Journal of Physical Chemistry C 113(48) (2009) 20576-20582.
[85] E.R. Meshot, A.J. Hart, Abrupt self-termination of vertically aligned carbon nanotube growth, Applied Physics Letters 92(11) (2008) 113107.
[86] E.R. Meshot, M. Bedewy, K.M. Lyons, A.R. Woll, K.A. Juggernauth, S. Tawfick, A.J. Hart, Measuring the lengthening kinetics of aligned nanostructures by spatiotemporal correlation of height and orientation, Nanoscale 2(6) (2010) 896-900.
[87] D.B. Geohegan, A.A. Puretzky, I.N. Ivanov, S. Jesse, G. Eres, J.Y. Howe, In situ growth rate measurements and length control during chemical vapor deposition of vertically aligned multiwall carbon nanotubes, Applied Physics Letters 83(9) (2003) 1851-1853.
[88] A.A. Puretzky, D.B. Geohegan, S. Jesse, I.N. Ivanov, G. Eres, In situ measurements and modeling of carbon nanotube array growth kinetics during chemical vapor deposition, Applied Physics A 81(2) (2005) 223-240.
[89] E.R. Meshot, D.L. Plata, S. Tawfick, Y. Zhang, E.A. Verploegen, A.J. Hart, Engineering vertically aligned carbon nanotube growth by decoupled thermal treatment of precursor and catalyst, Acs Nano 3(9) (2009) 2477-2486.
[90] E. Einarsson, Y. Murakami, M. Kadowaki, S. Maruyama, Growth dynamics of vertically aligned single-walled carbon nanotubes from in situ measurements, Carbon 46(6) (2008) 923-930.
[91] S. Hofmann, R. Sharma, C. Ducati, G. Du, C. Mattevi, C. Cepek, M. Cantoro, S. Pisana, A. Parvez, F. Cervantes-Sodi, In situ observations of catalyst dynamics during surface-bound carbon nanotube nucleation, Nano letters 7(3) (2007) 602-608.
[92] H. Yoshida, S. Takeda, T. Uchiyama, H. Kohno, Y. Homma, Atomic-scale in-situ observation of carbon nanotube growth from solid state iron carbide nanoparticles, Nano letters 8(7) (2008) 2082-2086.
[93] R. Sharma, Z. Iqbal, In situ observations of carbon nanotube formation using environmental transmission electron microscopy, Applied Physics Letters 84(6) (2004) 990-992.

[94] J.A. Rodríguez-Manzo, M. Terrones, H. Terrones, H.W. Kroto, L. Sun, F. Banhart, In situ nucleation of carbon nanotubes by the injection of carbon atoms into metal particles, Nature nanotechnology 2(5) (2007) 307.
[95] D.-M. Tang, C. Liu, W.-J. Yu, L.-L. Zhang, P.-X. Hou, J.-C. Li, F. Li, Y. Bando, D. Golberg, H.-M. Cheng, Structural changes in iron oxide and gold catalysts during nucleation of carbon nanotubes studied by in situ transmission electron microscopy, ACS nano 8(1) (2014) 292-301.
[96] M. Lin, J.P. Ying Tan, C. Boothroyd, K.P. Loh, E.S. Tok, Y.-L. Foo, Direct observation of single-walled carbon nanotube growth at the atomistic scale, Nano letters 6(3) (2006) 449-452.
[97] S. Helveg, C. Lopez-Cartes, J. Sehested, P.L. Hansen, B.S. Clausen, J.R. Rostrup-Nielsen, F. Abild-Pedersen, J.K. Nørskov, Atomic-scale imaging of carbon nanofibre growth, Nature 427(6973) (2004) 426-429.
[98] M. Bedewy, B. Viswanath, E.R. Meshot, D.N. Zakharov, E.A. Stach, A.J. Hart, Measurement of the dewetting, nucleation, and deactivation kinetics of carbon nanotube population growth by environmental transmission electron microscopy, Chemistry of Materials 28(11) (2016) 3804-3813.
[99] S. Jeong, J. Lee, H.-C. Kim, J.Y. Hwang, B.-C. Ku, D.N. Zakharov, B. Maruyama, E.A. Stach, S.M. Kim, Direct observation of morphological evolution of a catalyst during carbon nanotube forest growth: new insights into growth and growth termination, Nanoscale 8(4) (2016) 2055-2062.
[100] Y. Gao, T. Kodama, Y. Won, S. Dogbe, L. Pan, K.E. Goodson, Impact of nanotube density and alignment on the elastic modulus near the top and base surfaces of aligned multi-walled carbon nanotube films, Carbon 50(10) (2012) 3789-3798.
[101] A. Cao, P.L. Dickrell, W.G. Sawyer, M.N. Ghasemi-Nejhad, P.M. Ajayan, Super-compressible foamlike carbon nanotube films, Science 310(5752) (2005) 1307-1310.
[102] M.F. De Volder, S.H. Tawfick, R.H. Baughman, A.J. Hart, Carbon nanotubes: present and future commercial applications, science 339(6119) (2013) 535-539.
[103] M.R. Maschmann, Q. Zhang, F. Du, L. Dai, J. Baur, Length dependent foam-like mechanical response of axially indented vertically oriented carbon nanotube arrays, Carbon 49(2) (2011) 386-397.
[104] S.B. Hutchens, L.J. Hall, J.R. Greer, In situ mechanical testing reveals periodic buckle nucleation and propagation in carbon nanotube bundles, Advanced Functional Materials 20(14) (2010) 2338-2346.
[105] T. Hajilounezhad, M.R. Maschmann, Numerical investigation of internal forces during carbon nanotube forest self-assembly, ASME 2018 International Mechanical Engineering Congress and Exposition, American Society of Mechanical Engineers Digital Collection, 2018.
[106] E.R. Meshot, E. Verploegen, M. Bedewy, S. Tawfick, A.R. Woll, K.S. Green, M. Hromalik, L.J. Koerner, H.T. Philipp, M.W. Tate, High-speed in situ X-ray scattering of carbon nanotube film nucleation and self-organization, Acs Nano 6(6) (2012) 5091-5101.
[107] N.T. Dee, M. Bedewy, A. Rao, J. Beroz, B. Lee, E.R. Meshot, C.A. Chazot, P.R. Kidambi, H. Zhao, T. Serbowicz, In Situ Mechanochemical Modulation of Carbon Nanotube Forest Growth, Chemistry of Materials 31(2) (2018) 407-418.
[108] S.B. Hutchens, A. Needleman, J.R. Greer, Analysis of uniaxial compression of vertically aligned carbon nanotubes, Journal of the Mechanics and Physics of Solids 59(10) (2011) 2227-2237.
[109] Y. Won, Y. Gao, M.A. Panzer, R. Xiang, S. Maruyama, T.W. Kenny, W. Cai, K.E. Goodson, Zipping, entanglement, and the elastic modulus of aligned single-walled carbon nanotube films, Proceedings of the National Academy of Sciences 110(51) (2013) 20426-20430.
[110] M.R. Maschmann, Q. Zhang, R. Wheeler, F. Du, L. Dai, J. Baur, In situ SEM observation of column-like and foam-like CNT array nanoindentation, ACS applied materials & interfaces 3(3) (2011) 648-653.
[111] S. Sadasivam, S.L. Hodson, M.R. Maschmann, T.S. Fisher, Combined microstructure and heat transfer modeling of carbon nanotube thermal interface materials, Journal of Heat Transfer 138(4) (2016).
[112] J. Brown, T. Hajilounezhad, N.T. Dee, S. Kim, A.J. Hart, M.R. Maschmann, Delamination Mechanics of Carbon Nanotube Micropillars, ACS Applied Materials & Interfaces 11(38) (2019) 35221-35227.
[113] R. Hines, T. Hajilounezhad, C. Love-Baker, G. Koerner, M.R. Maschmann, Growth and Mechanics of Heterogeneous, 3D Carbon Nanotube Forest Microstructures Formed by Sequential Selective-Area Synthesis, ACS Applied Materials & Interfaces 12(15) (2020) 17893-17900.
[114] T. Hajilounezhad, D.M. Ajiboye, M.R. Maschmann, Evaluating the forces generated during carbon nanotube forest growth and self-assembly, Materialia 7 (2019) 100371.
[115] S. Sakurai, H. Nishino, D.N. Futaba, S. Yasuda, T. Yamada, A. Maigne, Y. Matsuo, E. Nakamura, M. Yumura, K. Hata, Role of subsurface diffusion and Ostwald ripening in catalyst formation for single-walled carbon nanotube forest growth, Journal of the American Chemical Society 134(4) (2012) 2148-2153.

[116] V. Balakrishnan, M. Bedewy, E.R. Meshot, S.W. Pattinson, E.S. Polsen, F. Laye, D.N. Zakharov, E.A. Stach, A.J. Hart, Real-time imaging of self-organization and mechanical competition in carbon nanotube forest growth, ACS nano 10(12) (2016) 11496-11504.
[117] D.M. Ajiboye, Mechanical analysis of a growing carbon nanotube forest, University of Missouri--Columbia, 2016.
[118] J.G. Hernández, C. Bolm, Altering product selectivity by mechanochemistry, The Journal of organic chemistry 82(8) (2017) 4007-4019.
[119] B. Hammer, J. Nørskov, Electronic factors determining the reactivity of metal surfaces, Surface Science 343(3) (1995) 211-220.
[120] S. Raghuraman, M.B. Elinski, J.D. Batteas, J.R. Felts, Driving surface chemistry at the nanometer scale using localized heat and stress, Nano letters 17(4) (2017) 2111-2117.
[121] A. Khorshidi, J. Violet, J. Hashemi, A.A. Peterson, How strain can break the scaling relations of catalysis, Nature Catalysis 1(4) (2018) 263-268.
[122] J.-H. Han, R.A. Graff, B. Welch, C.P. Marsh, R. Franks, M.S. Strano, A mechanochemical model of growth termination in vertical carbon nanotube forests, Acs Nano 2(1) (2008) 53-60.
[123] K. Liu, K. Jiang, C. Feng, Z. Chen, S. Fan, A growth mark method for studying growth mechanism of carbon nanotube arrays, Carbon 43(14) (2005) 2850-2856.
[124] M.J. Bronikowski, Longer nanotubes at lower temperatures: the influence of effective activation energies on carbon nanotube growth by thermal chemical vapor deposition, The Journal of Physical Chemistry C 111(48) (2007) 17705-17712.
[125] Y.T. Lee, J. Park, Y.S. Choi, H. Ryu, H.J. Lee, Temperature-dependent growth of vertically aligned carbon nanotubes in the range 800− 1100° C, The Journal of Physical Chemistry B 106(31) (2002) 7614-7618.
[126] G.D. Nessim, A.J. Hart, J.S. Kim, D. Acquaviva, J. Oh, C.D. Morgan, M. Seita, J.S. Leib, C.V. Thompson, Tuning of Vertically-Aligned Carbon Nanotube Diameter and Areal Density through Catalyst Pre-Treatment, Nano Lett. 8(11) (2008) 3587-3593.
[127] G. Zhong, J.H. Warner, M. Fouquet, A.W. Robertson, B. Chen, J. Robertson, Growth of ultrahigh density single-walled carbon nanotube forests by improved catalyst design, ACS nano 6(4) (2012) 2893-2903.
[128] X. Zhang, A. Cao, B. Wei, Y. Li, J. Wei, C. Xu, D. Wu, Rapid growth of well-aligned carbon nanotube arrays, Chemical Physics Letters 362(3) (2002) 285-290.
[129] A. Cao, V.P. Veedu, X. Li, Z. Yao, M.N. Ghasemi-Nejhad, P.M. Ajayan, Multifunctional brushes made from carbon nanotubes, Nature materials 4(7) (2005) 540-545.
[130] H.-C. Su, C.-H. Chen, Y.-C. Chen, D.-J. Yao, H. Chen, Y.-C. Chang, T.-R. Yew, Improving the adhesion of carbon nanotubes to a substrate using microwave treatment, Carbon 48(3) (2010) 805-812.
[131] P. Pour Shahid Saeed Abadi, S.B. Hutchens, J.R. Greer, B.A. Cola, S. Graham, Buckling-driven delamination of carbon nanotube forests, Applied Physics Letters 102(22) (2013) 223103.
[132] J. An, Z. Zhan, L. Zheng, Controllable Synthesis of Carbon Nanotubes, Industrial Applications of Carbon Nanotubes, Elsevier2017, pp. 1-45.
[133] S.J. Kang, C. Kocabas, T. Ozel, M. Shim, N. Pimparkar, M.A. Alam, S.V. Rotkin, J.A. Rogers, High-performance electronics using dense, perfectly aligned arrays of single-walled carbon nanotubes, Nature nanotechnology 2(4) (2007) 230.
[134] C. Kocabas, S.J. Kang, T. Ozel, M. Shim, J.A. Rogers, Improved synthesis of aligned arrays of single-walled carbon nanotubes and their implementation in thin film type transistors, The Journal of Physical Chemistry C 111(48) (2007) 17879-17886.
[135] S. Wang, Z. Zhang, L. Ding, X. Liang, J. Shen, H. Xu, Q. Chen, R. Cui, Y. Li, L.M. Peng, A Doping-Free Carbon Nanotube CMOS Inverter-Based Bipolar Diode and Ambipolar Transistor, Advanced Materials 20(17) (2008) 3258-3262.
[136] Z. Chen, J. Appenzeller, Y.-M. Lin, J. Sippel-Oakley, A.G. Rinzler, J. Tang, S.J. Wind, P.M. Solomon, P. Avouris, An integrated logic circuit assembled on a single carbon nanotube, Science 311(5768) (2006) 1735-1735.
[137] K.G. Reyes, B. Maruyama, The machine learning revolution in materials?, MRS Bulletin 44(7) (2019) 530-537.
[138] R. Gómez-Bombarelli, J. Aguilera-Iparraguirre, T.D. Hirzel, D. Duvenaud, D. Maclaurin, M.A. Blood-Forsythe, H.S. Chae, M. Einzinger, D.-G. Ha, T. Wu, Design of efficient molecular organic light-emitting

diodes by a high-throughput virtual screening and experimental approach, Nature materials 15(10) (2016) 1120.
[139] J.J. Low, A.I. Benin, P. Jakubczak, J.F. Abrahamian, S.A. Faheem, R.R. Willis, Virtual high throughput screening confirmed experimentally: porous coordination polymer hydration, Journal of the American Chemical Society 131(43) (2009) 15834-15842.
[140] S.M. Azimi, D. Britz, M. Engstler, M. Fritz, F. Mücklich, Advanced steel microstructural classification by deep learning methods, Scientific reports 8(1) (2018) 2128.
[141] H. Majidifard, Y. Adu-Gyamfi, W.G. Buttlar, Deep machine learning approach to develop a new asphalt pavement condition index, Construction and Building Materials 247 (2020) 118513.
[142] H. Majidifard, B. Jahangiri, W.G. Buttlar, A.H. Alavi, New machine learning-based prediction models for fracture energy of asphalt mixtures, Measurement 135 (2019) 438-451.
[143] H. Majidifard, P. Jin, Y. Adu-Gyamfi, W.G. Buttlar, Pavement Image Datasets: A New Benchmark Dataset to Classify and Densify Pavement Distresses, Transportation Research Record (2020) 0361198120907283.
[144] A. LENJANI, S. DYKE, I. BILIONIS, C.M. YEUM, J. CHOI, A. LUND, A. MAGHAREH, Hierarchical Convolutional Neural Networks Information Fusion for Activity Source Detection in Smart Buildings, Structural Health Monitoring 2019 (2019).
[145] A. Lenjani, I. Bilionis, S. Dyke, C.M. Yeum, R. Monteiro, A Resilience-based Method for Prioritizing Post-event Building Inspections, arXiv preprint arXiv:1906.12319 (2019).
[146] A. Lenjani, S.J. Dyke, I. Bilionis, C.M. Yeum, K. Kamiya, J. Choi, X. Liu, A.G. Chowdhury, Towards fully automated post-event data collection and analysis: pre-event and post-event information fusion, arXiv preprint arXiv:1907.05285 (2019).
[147] Y. Dong, C. Wu, C. Zhang, Y. Liu, J. Cheng, J. Lin, Bandgap prediction by deep learning in configurationally hybridized graphene and boron nitride, npj Computational Materials 5(1) (2019) 26.
[148] D.P. Tabor, L.M. Roch, S.K. Saikin, C. Kreisbeck, D. Sheberla, J.H. Montoya, S. Dwaraknath, M. Aykol, C. Ortiz, H. Tribukait, Accelerating the discovery of materials for clean energy in the era of smart automation, Nature Reviews Materials 3(5) (2018) 5-20.
[149] B.P. MacLeod, F.G. Parlane, T.D. Morrissey, F. Häse, L.M. Roch, K.E. Dettelbach, R. Moreira, L.P. Yunker, M.B. Rooney, J.R. Deeth, Self-driving laboratory for accelerated discovery of thin-film materials, arXiv preprint arXiv:1906.05398 (2019).
[150] V.S. Prasath, Y.M. Kassim, Z.A. Oraibi, J.-B. Guiriec, A. Hafiane, G. Seetharaman, K. Palaniappan, HEp-2 cell classification and segmentation using motif texture patterns and spatial features with random forests, 2016 23rd International Conference on Pattern Recognition (ICPR), IEEE, 2016, pp. 90-95.
[151] Z.A. Oraibi, H. Yousif, A. Hafiane, G. Seetharaman, K. Palaniappan, Learning local and deep features for efficient cell image classification using random forests, 2018 25th IEEE International Conference on Image Processing (ICIP), IEEE, 2018, pp. 2446-2450.
[152] Z.A. Oraibi, M. Irio, A. Hafiane, K. Palaniappan, Texture classification using multiple local descriptors, 2017 IEEE Applied Imagery Pattern Recognition Workshop (AIPR), IEEE, 2017, pp. 1-7.
[153] T. Ojala, M. Pietikainen, T. Maenpaa, Multiresolution gray-scale and rotation invariant texture classification with local binary patterns, IEEE Transactions on pattern analysis and machine intelligence 24(7) (2002) 971-987.
[154] A. Hafiane, S. Chaudhuri, G. Seetharaman, B. Zavidovique, Region-based CBIR in GIS with local space filling curves to spatial representation, Pattern Recognition Letters 27(4) (2006) 259-267.
[155] R. Nosaka, K. Fukui, HEp-2 cell classification using rotation invariant co-occurrence among local binary patterns, Pattern Recognition 47(7) (2014) 2428-2436.
[156] A. Hafiane, K. Palaniappan, G. Seetharaman, Joint adaptive median binary patterns for texture classification, Pattern Recognition 48(8) (2015) 2609-2620.
[157] A. Hafiane, K. Palaniappan, G. Seetharaman, Adaptive median binary patterns for texture classification, 2014 22nd International Conference on Pattern Recognition, IEEE, 2014, pp. 1138-1143.
[158] T. Hajilounezhad, Z.A. Oraibi, R. Surya, F. Bunyak, M.R. Maschmann, P. Calyam, K. Palaniappan, Exploration of Carbon Nanotube Forest Synthesis-Structure Relationships Using Physics-Based Simulation and Machine Learning, (2020).
[159] T.K. Ho, Random decision forests, Proceedings of 3rd international conference on document analysis and recognition, IEEE, 1995, pp. 278-282.
[160] L. Breiman, Bagging predictors, Machine learning 24(2) (1996) 123-140.

[161] D.N. Futaba, K. Hata, T. Yamada, K. Mizuno, M. Yumura, S. Iijima, Kinetics of water-assisted single-walled carbon nanotube synthesis revealed by a time-evolution analysis, Physical review letters 95(5) (2005) 056104.
[162] J. Deng, W. Dong, R. Socher, L.-J. Li, K. Li, L. Fei-Fei, Imagenet: A large-scale hierarchical image database, 2009 IEEE conference on computer vision and pattern recognition, Ieee, 2009, pp. 248-255.
[163] G. Cheng, J. Han, X. Lu, Remote sensing image scene classification: Benchmark and state of the art, Proceedings of the IEEE 105(10) (2017) 1865-1883.
[164] S. Ren, K. He, R. Girshick, J. Sun, Faster r-cnn: Towards real-time object detection with region proposal networks, Advances in neural information processing systems, 2015, pp. 91-99.
[165] K. Simonyan, A. Zisserman, Very deep convolutional networks for large-scale image recognition, arXiv preprint arXiv:1409.1556 (2014).
[166] L. Breiman, Random forests, Machine learning 45(1) (2001) 5-32.
[167] P. Geurts, D. Ernst, L. Wehenkel, Extremely randomized trees, Machine learning 63(1) (2006) 3-42.
[168] P. Python, Scikit-learn: Machine Learning, JMLR 12 (2011) 2825-2830.
[169] L.v.d. Maaten, G. Hinton, Visualizing data using t-SNE, Journal of machine learning research 9(Nov) (2008) 2579-2605.
[170] S. Wold, K. Esbensen, P. Geladi, Principal component analysis, Chemometrics and intelligent laboratory systems 2(1-3) (1987) 37-52.

VITA

Taher Hajilounezhad was born in Urmia, Iran. He completed a Bachelor's of Science in Mechanical Engineering at Urmia University, graduated in Feb. 2006. In September 2010 Taher received a Master's of Science in Mechanical Engineering from the University of Tabriz with the emphasis on energy conversion systems for his thesis work, "Thermodynamic Analysis of Combined Refrigeration Cycles". Finally, he received a Doctoral Degree also in Mechanical Engineering from the University of Missouri for his work," Evaluation of Process-Structure-Property Relationships of Carbon Nanotube Forests Using Simulation and Deep Learning". Taher started working with Professor Matthew Maschmann in the Fall Semester of 2016 as the first PhD student of the "Advanced Nanostructures Group (ANG)". His work has included studying the fundamental mechanics and assembly of carbon nanotube forests. He developed a physics-based and time-resolved finite-element simulation model as well as conducting in-situ CNT growth inside Scanning Electron Microscope (SEM). His main objective of developing such novel techniques is to make an active learning data-driven predictive model that employs simulation, in situ experimentation and deep neural networks to predict CNT forest processing conditions based on desired properties. This is a key step towards synthesis of materials by design to accelerate adoption of their exceptional properties into various industrial applications. Taher will start his career in industry in May 2020 working for Martin Energy Group in Tipton, Missouri as a Senior R&D Engineer.